1-1-1998

A zero-bias spark source for direct solid sample introduction for inductively coupled plasma atomic emission spectrometry

Billie A. Shepherd

A "ZERO-BIAS" SPARK SOURCE FOR DIRECT SOLID SAMPLE INTRODUCTION FOR INDUCTIVELY COUPLED PLASMA ATOMIC EMISSION SPECTROMETRY

by

BILLIE A. SHEPHERD

DISSERTATION

Submitted to the Graduate School

of Wayne State University,

Detroit, Michigan

in partial fulfillment of the requirements

for the degree of

DOCTOR OF PHILOSOPHY

1998

MAJOR: CHEMISTRY (Analytical)

Approved by:

1/28/98

Advisor Date

Ratna Naik

DEDICATION

To my family: my parents, Becky, Barry, Robin, Jeremy, Ryan and Nuna for their love and patience.

To David Burger whose love, encouragement, and understanding have helped me through the good and bad times.

ACKNOWLEDGMENTS

My deepest gratitude and appreciation to Dr. David M. Coleman for his guidance, encouragement, and moral support throughout my graduate career.

To my graduate committee, Drs. David Rorabacher, Gang-yu Liu, and Ratna Naik for their time, advice, and assistance.

I deeply appreciate the support of Susan McIntosh and the Perkin-Elmer Corporation for their continuous collaboration with this research project.

I am grateful to Dr. Paul Beckwith for the loan of the sample holder and the steel and brass standards, to the Alcoa Corporation for the loan of the aluminum alloys, and to the Royal Canadian Mint for the loan of the gold standards.

To Dr. Oleg V. Borisov for his contributions and generosity on a number of experiments. Special thanks are expressed to Fr. Ed Gorman, Amy Robinson, and B.J. Ximba, for their assistance.

To my family and friends for their continuous support.

TABLE OF CONTENTS

LIST OF TABLES

LIST OF FIGURES

Chapter 1

History and Development

ICP-AES

Investigation of the inductively coupled plasma (ICP) dates back to 1946 when Babat[1] published a paper on electrodeless discharges in high-frequency magnetic fields. Analytical studies of the ICP were first pursued individually by two different research groups, Greenfield *et al.*[2] and Wendt and Fassel[3] in the early 1960's. Both groups followed Reed's work[4] in the field of high-frequency plasma generation. Greenfield[2] and Fassel[3] were concerned with investigations of plasma parameters, both experimental and theoretical, and they also studied the use of plasmas as a source for spectrochemical analysis.

Interest in the ICP as spectroscopic emission sources developed from problems associated with flame photometry. Stable compounds can form in the flame and cause interferences with elements of interest. Flame spectroscopy also has limited powers of detection for some elements, limited dynamic range, and can only identify a few elements at a time. Alterations have been made in order to raise the temperature of the flame to decrease the number of compounds formed.[5-8] A few of the modifications, such as using an oxy-cyanogen and a hydrogen-fluorine flame to increase the temperature of the flame, were considered too hazardous for general use.[5,6] D.C.-arc plasmas and the ICP offered partial solutions to this problem.[2]

The ICP, when used as an ion source for atomic emission spectroscopy (AES), has the advantage of rapid and easy sample introduction due to the high temperatures achieved. ICP-AES has the advantage of simultaneous or rapid sequential determination of the elements. The ICP has numerous advantageous over the d.c. arc in that it is simple to operate, involves no electrodes which cause contamination, and possesses low background levels. For these reasons, the ICP has become one of the most common methods for trace inorganic analytical studies.

General Concepts

ICP

A plasma is a gas in which atoms are present in an ionized state. A plasma that is generated by sustaining its power through induction from a high-frequency magnetic field is termed an inductively coupled plasma. The plasma is sustained in a quartz torch consisting of three concentric tubes. A typical inductively coupled plasma is shown in **Figure 1**. Argon is introduced tangentially through the two outer tubes and, once it passes through the top of the torch, it is surrounded by an induction coil. An a.c. current flows through the coil at a frequency of either 27 or 40 MHz and at power levels ranging from 750-1500 W.[9]

The auxiliary gas that enters the coil is initially seeded with free electrons from a Tesla discharge coil. These electrons interact with the magnetic field of the coil and gain sufficient energy to ionize argon atoms by collisional excitation. Cations and electrons generated by the initial Tesla spark are accelerated by the magnetic field in a circular flow perpendicular to the stream that emerges from the tip of the torch. They collide with more argon atoms to produce further ionization and thermal energy. A flame-shaped plasma forms near the top of the torch. Temperatures in the plasma range from 6000-10,000 K.[9]

A second stream of argon, the plasma gas, creates a vorticular flow to maintain the plasma, stabilize its position, and thermally isolate the plasma from the outer confinement tube. A third argon flow, the nebulizer flow, carries the sample into the plasma.[10]

Sample Introduction

Samples for ICP analysis can be aqueous solutions transformed to a gaseous state, or solid particulates. The most common sample introduction is the nebulization of liquids which produces a fine aerosol of droplets. The most common device of sample introduction for the ICP is the pneumatic nebulizer. General types include the cross-

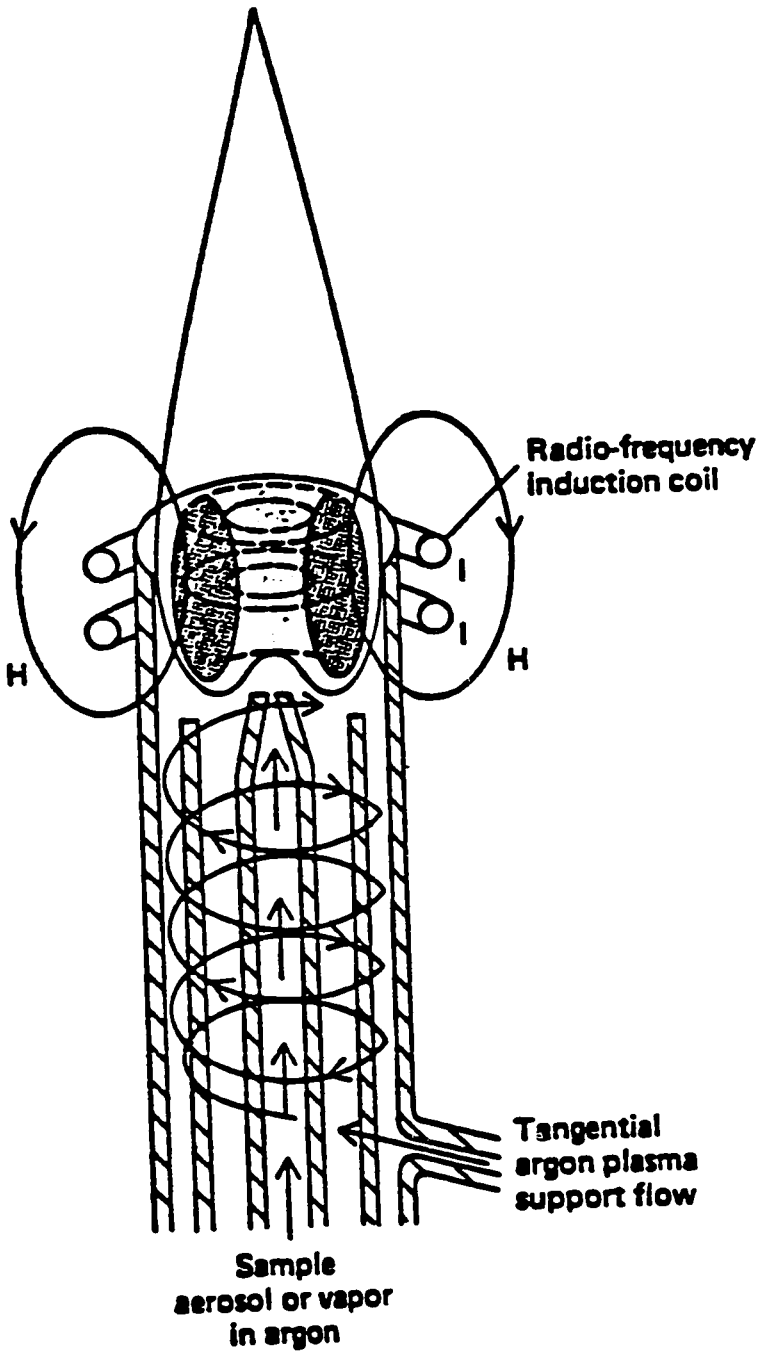

Figure 1. Diagram of an Inductively Coupled Plasma.

flow, conespray, or Meinhard pneumatic nebulizers. A peristaltic pump may be used to control the flow rate of liquids entering the nebulizer. High gas velocities are required to produce an efficient aerosol. Droplets of less than 10 μm diameter are efficiently transported to the plasma. Most droplets are larger and are removed by the spray chamber. The efficiency of sample introduction is therefore usually below 3% and often less than 1%.

Solid sampling for ICP analysis eliminates the sample dissolution steps, which are often time consuming and a major source of errors in an analysis. Solvent contamination, low recovery of the sample, and conflicting requirements for dissolution of various elements and analyte dilution are some problems associated with sample preparation for the nebulization of liquids. Solid sampling significantly decreases the various interferences of matrix and digestion acid-induced interferences.

Detection

ICP-AES is able to detect approximately 70 elements. Concentration linearity is typically 5 orders of magnitude. Detection limits range from 1-100 mg/l or better. The technique is suitable for all concentrations, from ultra-trace levels to major components, because each element has many wavelengths with various sensitivities. Precision and accuracy are both within a few percent. ICP-AES can do simultaneous and rapid determinations of a large number of elements.

The Perkin-Elmer Optima 3000 uses a uniquely modified echelle polychromator with multi-channel solid-state detectors as shown in **Figure 2**. The polychromator system covers the spectral range of 167 to 782 nm. It provides high optical throughput, low stray light, and high stability.[11]

The total spectrum is divided into a UV region and a visible region; each independent detector is appropriately optimized for resolution and throughput. Both regions have their own cross-dispersion, focal length, and multi-channel solid-state detector. A Schmidt aspheric reflector in the UV region corrects for spherical aberration,

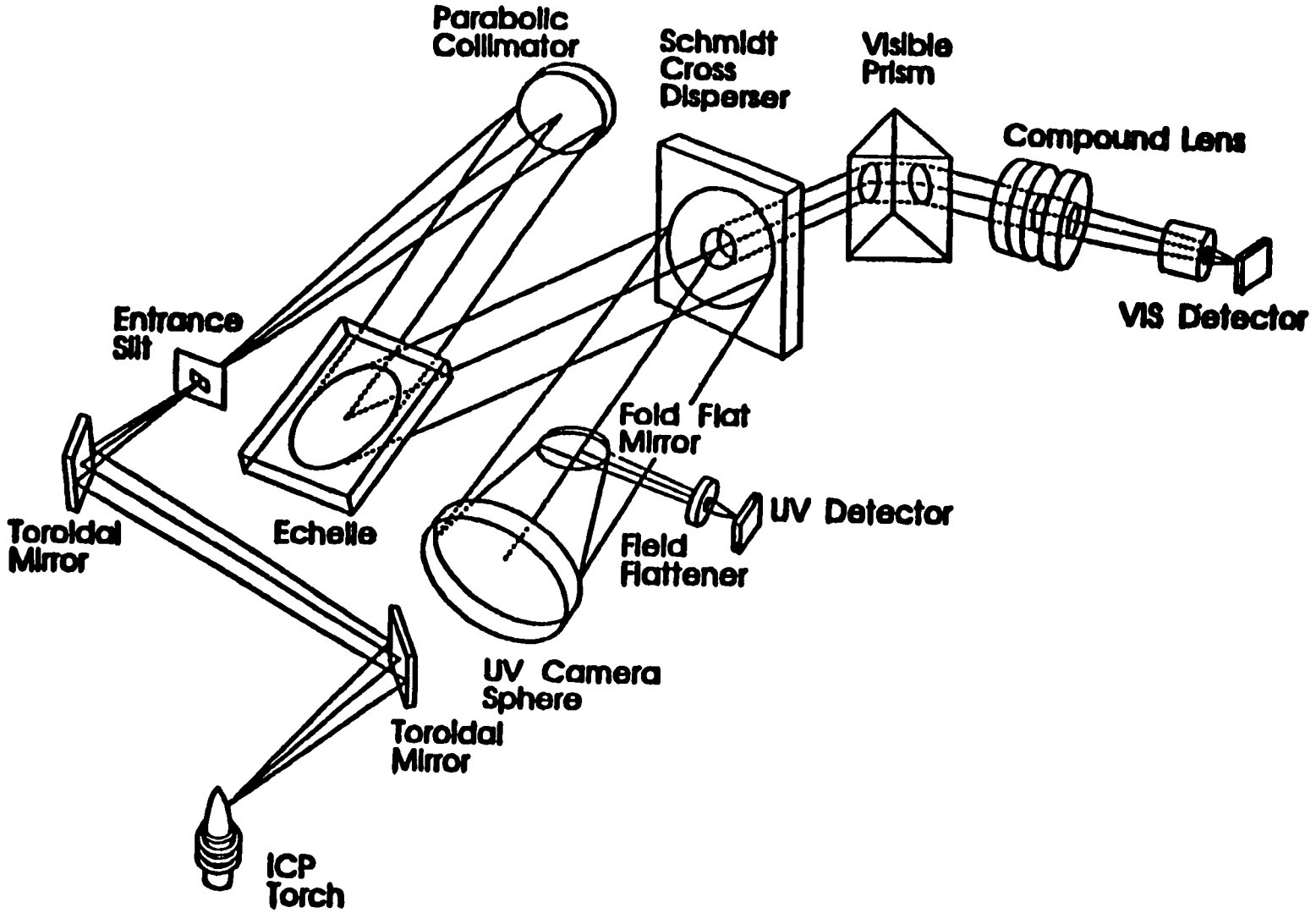

Figure 2. Diagram of the Perkin-Elmer Optima 3000 modified echelle polychromator.

improving resolution while providing high optical throughput.[11]

The optical system consists of the plasma image transfer section, entrance slit, input collimator, echelle grating, and two output sections. The two output sections disperse multiple diffraction orders orthogonally to the echelle dispersion and focus the resulting spectra on detectors.[11] Each detector is physically small, *ca.* 13 mm x 19 mm.

The detectors are segmented-array charge-coupled devices (SCD) which include high quantum efficiency in the UV, low noise, rapid readout, broad spectral coverage, and high spectral resolution. A top view of an SCD is shown in **Figure 3**. The detector is a silicon chip with a series of linear sub-arrays comprised of pixels on its surface. The sub-arrays are positioned on the detector at x-y locations which correspond to the exact location of the desired emission lines generated by the echelle spectrometer.[12] **Figure 4** shows the high resolution capability of the SCD to differentiate between Cd at a wavelength of 228.802 and As at a wavelength of 228.812.

Spark

Historically, most major improvements in the analytical utility of spark sources originated from Walters research group at the University of Wisconsin. Progress in this field continues with a few of Walter's former students and others. The spark source is generally used as an emission source for multi-element chemical analysis. Review articles on spark sources have been published by Walters[13] and Scheeline.[14,15]

In spark sources, sample excitation occurs in the gap, within a closed spark stand, between a pair of electrodes. A large amount of energy is transmitted between the electrodes in a short period of time. Material is removed by the resulting discharge and these particles may be excited and/or ionized. The sparking phenomenon consists of several critical phases: initial breakdown, channel formation, electrode sampling, and vapor propagation. Walters[13] thoroughly reviewed the literature regarding various interpretations of these processes.

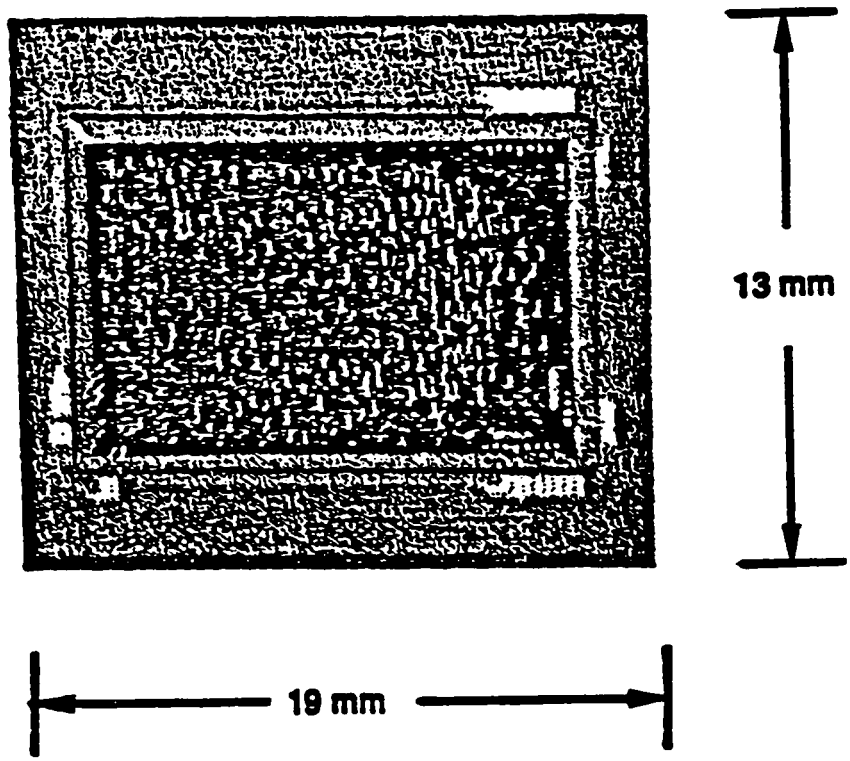

Figure 3. Top view of a segmented-array charge coupled device.

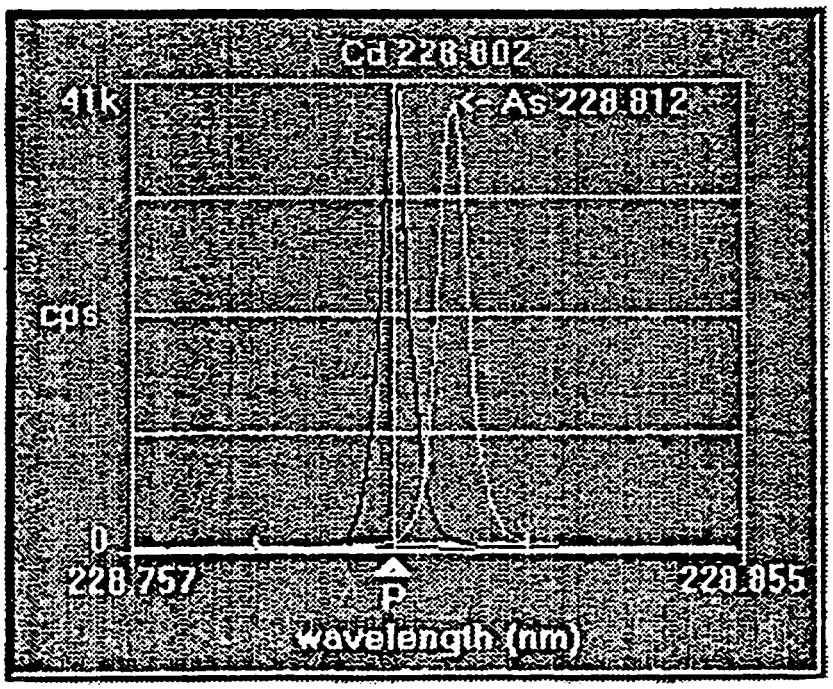

Figure 4. High resolution capabilities of SCD.

If a potential is applied between two electrodes, where the intensity is dependent on their geometry and the gas properties, the gas can become a conductor. The transition from a poor conductor to a relatively good conductor is known as the electrical breakdown of the spark. The interelectrode potential difference at which this transition occurs is critical and is known as the sparking potential. This potential is dependent on the nature and number density of the gas, electrode composition, state of electrodes, and the gap length.[16,17]

Initial breakdown is important because it produces the gas phase charge carriers that conduct the discharge current. A process of even more importance is one that brings about the physical aggregation of these charge carriers into a shaped-pathway, or channel, for gas phase conduction of the discharge current.[13]

Spark discharge is a complex process in which a large number of parameters must be carefully controlled for repeatability. These parameters can be divided into electrical and non-electrical quantities. The main electrical parameters which must be controlled include direction, magnitude, density, and the dI/dt rate of change of the current waveform. Gap length, electrode shape, discharge gas composition, discharge repetition rate, and electrode composition are among the non-electrical parameters of importance.[14]

Thackeray[18] first used argon jets to stabilize a spark discharge. A stream of argon was made to flow in laminar fashion from one electrode to the other. It was then possible to establish a discharge in argon, of shape, size, and position that was somewhat repeatable from spark to spark.

The resulting discharge removes material from the cathode. The amount of charge delivered, the discharge current, and the nature of the electrode determine the amount of erosion. The exact nature of the sampling process with a spark source is still not well understood. It is believed that the spark samples by some combination of melting, bulk heating, vaporization, and sputtering.

Sputtering is the erosion of a solid by bombardment of a surface with ions. An

ion with enough energy can break the bond of surface atoms sufficiently to dislodge atoms from the solid. The atoms are ejected into the gas or vacuum above the solid, accomplishing sampling.[15]

Brewer and Walters[19] examined the erosion craters on brass, aluminum, and steel samples. Multiple sampling points were evident. Pb and Bi in aluminum and Pb in brass samples appeared to migrate to the eroded area.

Scheeline *et al.*[20] examined the formation and physical size distribution of spark-produced aerosol. They found two distinct types of particles: spheres between 0.5 and 2 mm in diameter and aggregates of small spherules. The two types of particles were believed to have different histories, with the large spheres representing solidified liquid droplets and the small particles arising from condensed free atoms.

Prell and Koirtyohann[21] reported transport efficiencies and physical properties of spark-generated aerosols. They observed three types of particles: large, irregularly shaped particles, which are believed to be ablated materials; round, dense particles, which are believed to be material that melted off the surface and later solidified; and irregularly shaped, spongy looking material, which represents aggregates of spherical properties.

Raeymaekers *et al.*[22] examined the composition of spark-produced particles. They found that most of the particles were similar in composition to the electrode material, probably consisting of vapor formed by evaporation of molten spots. Large particles may originate from sputtering and bulk heating.

Watters *et al.*[23] studied the physical properties and chemical composition of spark-produced aerosol. More volatile elements were found concentrated in the aerosol and depleted in the erosion pit relative to the original concentrations of the sample.

The vapor, consisting of particles of the cathode from a spark discharge, travels in the form of high velocity jets. These jets are physically distinct from the discharge channel. Velocities of these jets were found to depend on the electrode material, the electrode shape, and the spark current.[24]

The electrode jet mechanism is complex and only relatively simple models exist.[17] The vapor jet has been attributed to a gas dynamic process involving the expansion of evaporated high temperature electrode material, explosive erosion, or an axial pressure gradient in the channel produced by plasma pinching.

The present research includes investigations of a "zero-bias" spark source[25] as a sample introduction for ICP spectrometry. Conventional spark sources are primarily high voltage, physically large, and quite uncontrollable. The new source, which is being developed in conjunction with the Perkin-Elmer Corporation, represents an entirely different approach to spark ablation sampling for atomic spectroscopy. It operates on relatively low voltage, is physically small, operates using entirely solid state components, is both electronically and acoustically quiet, and eliminates background bias current. Coleman has discovered that these previously undiscovered bias currents seriously affect analytical performance. [25]

Spark-Sampling ICP-AES

Inductively Coupled Plasma Atomic Emission Spectrometry (ICP-AES) and Inductively Coupled Plasma Mass Spectrometry (ICP-MS) are widely employed analytical techniques. As noted earlier, the most common method of sample introduction for ICP spectrometry involves the nebulization of liquids into the radio frequency torch. For many analytical problems this mandates that the sample be subjected to time-consuming and error-prone dissolution techniques. Direct solid analysis has an inherent advantage for ICP applications as it allows a dry plasma to be maintained. This helps minimize the background species present as many arise from the water and acids present in solution.

Several methods of direct solid sampling have been used with ICP spectrometry including direct insertion of samples into the plasma,[26-28] electrothermal vaporization,[29-32] radio frequency arc,[33] and laser ablation.[34-42] Spark ablation[43-58] has previously been shown to be a useful technique in solid sampling. Spark sampling

has been evaluated for use in conjunction with ICP-AES[46-54] and ICP-MS.[55-58] Human[46] was the first to describe the use of spark ablation combined with ICP-AES for the analysis of compact metallic samples.

Each method of solid sample introduction presents certain advantages and disadvantages. Direct insertion differs from the other methods in that it does not employ separate sampling and excitation process. It is also not amenable to all sample types. Laser ablation is the focus of many research efforts and commercial instruments are available. However, this technique is expensive and difficult to operate. In addition, it is usually characterized by poor accuracy and precision. Spark ablation has been shown to have advantages over arc ablation due to its higher instantaneous current and reduced discharge wander. For these reasons the spark source as a solid sampling device has been a major focus of this research group.

The new "zero-bias" spark source which directly ablates material from a variety of conductive metal standards and samples for ICP excitation and detection is employed in the present work. The use of a spark source as a sample introduction method for ICP employs separate sampling and excitation processes. In separating these two events, both may be optimized to give enhanced performance. Preliminary research was also carried out using the "zero-bias" spark source coupled to an ICP-MS.[59]

Chapter 2

Instrument Development

ICP-AES

A commercially available ICP-AES (Perkin-Elmer Optima 3000, Norwalk, CT) instrument has been used in these experiments. The Optima 3000 uses a 40-MHz free-running generator. The actual frequency output changes slightly as the electrical characteristics of the plasma change enabling the most efficient coupling of the RF power to the plasma in free-running generators.[60] The RF generator provides a power output of 750 to 1500 watts. An in-house water supply was used as cooling water for the RF coil and detectors. Liquid Nitrogen (LINDE) was used to purge the optical system during operation to remove oxygen and moisture and to keep the environment dry. Argon gas in the form of liquid argon (AGA Gases) was used for ICP plasma operation. Operating Parameters are given in **Table 1.**

Table 1. Parameters of the ICP-AES.

RF Power	**1100-1250 Watts**
Argon Flow	
Nebulizer Flow	
Auxiliary Flow	**1.0 L/min**
Plasma Flow	**15 L/min**
Viewing Height	**15 mm**
Manual Integration Time	
Sampling Time	**500-10,000 ms**
Integration Time	**50-2000 ms**
Auto Background Correction	
Resolution	**< 6 pm at 220 nm**
Recipricol Linear Dispersion	**168.7 nm/m**
Diffraction Angle	**63^0**
Limit of Detection	**0.1 - 100 ng/mL**
Sensitivity	**10^4**
Accuracy	**within a few percent**
Precision	**0.5 - 2 %**
Dynamic Range	**4 - 6 orders of magnitude**
Spectral Range	**167 - 782 nm**
Elemental Range	**72 elements, > 5000 ICP emission lines**

Spark

Prior research in interfacing a spark ablation device with ICP detection was mostly carried out utilizing a medium- or high voltage uni-directional spark source. Some of the characteristics associated with these spark sources are the large size (the size of a desk), continuous high voltage, and a significant degree of spark discharge wander around the surface of an electrode. Discharge positional instability results in undesirable and poor analytical results. **Figure 5a** shows the simplified circuit used to generate the uni-directional waveform. Because of the high voltages (on the order of 10 to 15 kV) present in the circuit continuously, the active component's impedance allows conduction of electrical current during charging cycles. In **Figure 5b** this phenomena is shown as reactances associated with the circuit components. The leakage current is negligibly small (only a few mA) compared to the "spark" current (10 to 150 A) ejected in the course of the discharge. None-the-less it still plays a significant role when the amount of charge delivered to the surface by these two currents in their intervals are considered (**Figure 6**). It is thought that the amount of material removed from the surface is proportional to the number of coulombs delivered to that surface. **Figure 6** shows simple calculations (for a hypothetical but typical example) indicating that the charge delivered to the surface by the short-term spark discharge current is approximately equal to the continuous low bias current. Hence, the bias current acts as a "real" addition to the actual discharge current (primary discharge) and may be responsible for secondary processes (*e.g.*, secondary discharges) of sample removal. This phenomena is shown in **Figure 7**.

Figure 8 shows actual burn patterns from the two spark sources. During each pulse there is typically a 100 amp discharge through the counter-electrode to the grounded sample. However, once initiated it takes only a few milliamps to sustain a spark discharge. If the spark is sustained between discharges, it wanders. It will wander out of the pit area that is being formed, so that the next discharge, instead of sampling the same pit area, it may be off to the side. This area looks like it has been chemically

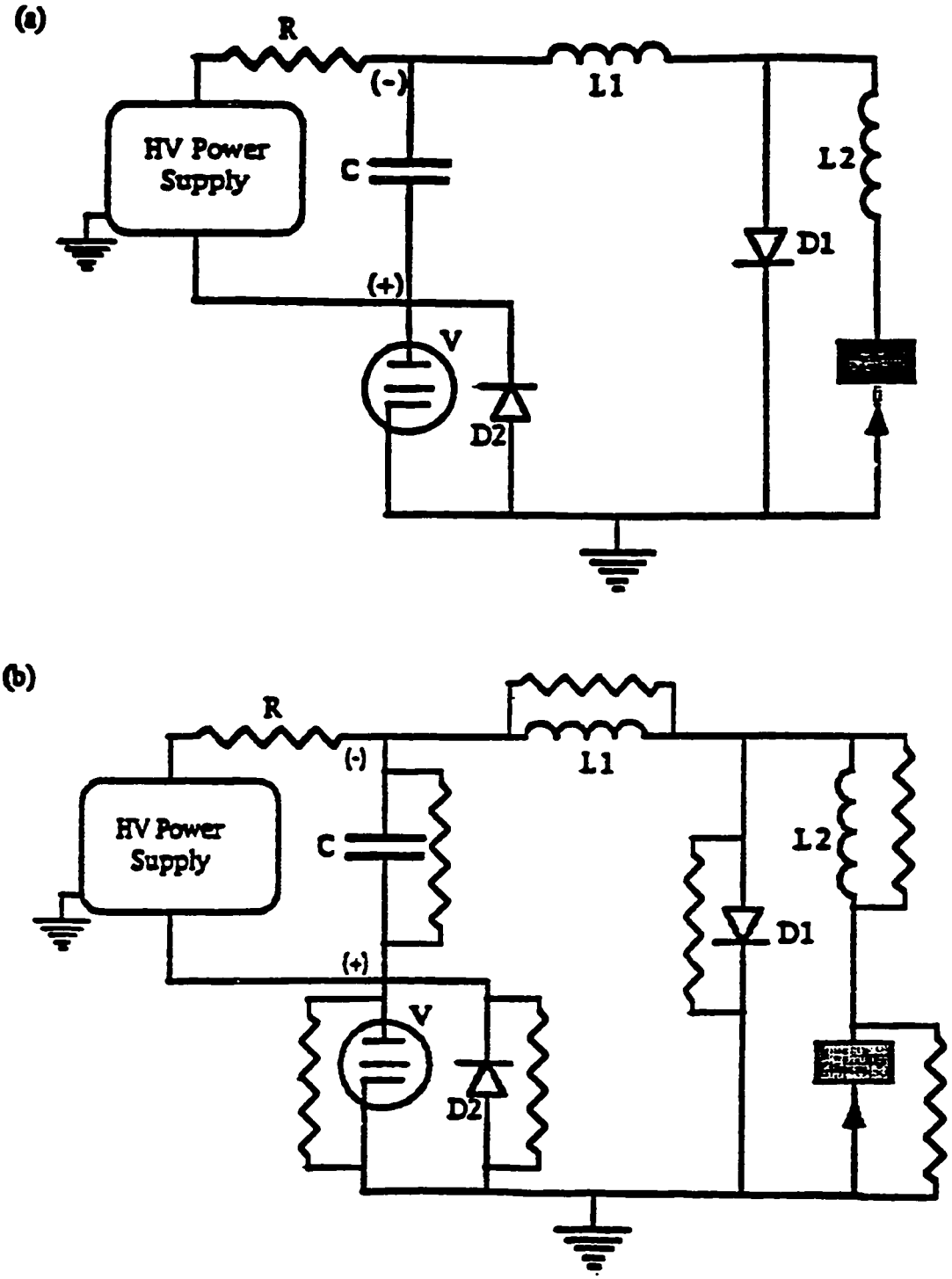

Figure 5. (a) A simplified circuit diagram of a high voltage uni-directional spark source, (b) reactances associated with circuit components due to the high voltage used.

1 KHz, 100 A Spark with a 250 mA Continuous Secondary Discharge

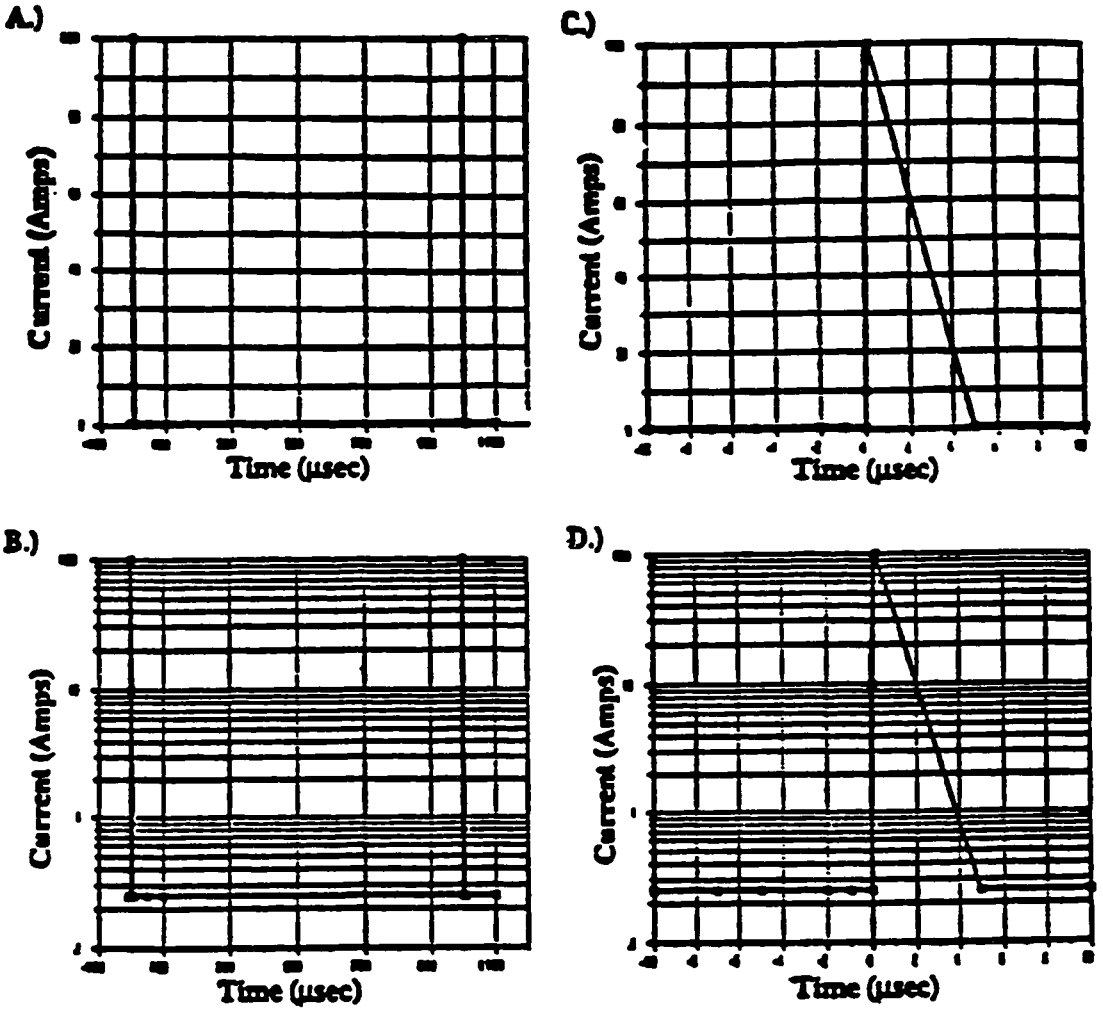

Charge delivered to the electrode due to the primary spark discharge (interval of 1 spark - 5 µs):

$$Q = \int idt = (10^2) \times (1/2) \times (5 \times 10^{-6}) = 2.5 \times 10^{-4} \quad \textit{Coulombs}$$

Charge delivered to the electrode due to the secondary discharge (interval of 1 spark - 1 ms):

$$Q = \int idt = (0.25) \times (10^3) \times (10^{-6}) = 2.5 \times 10^{-4} \quad \textit{Coulombs}$$

Figure 6. Current peak waveform for the conventional high voltage spark source (a,c) linear scale and (b,d) logarithmic scale.

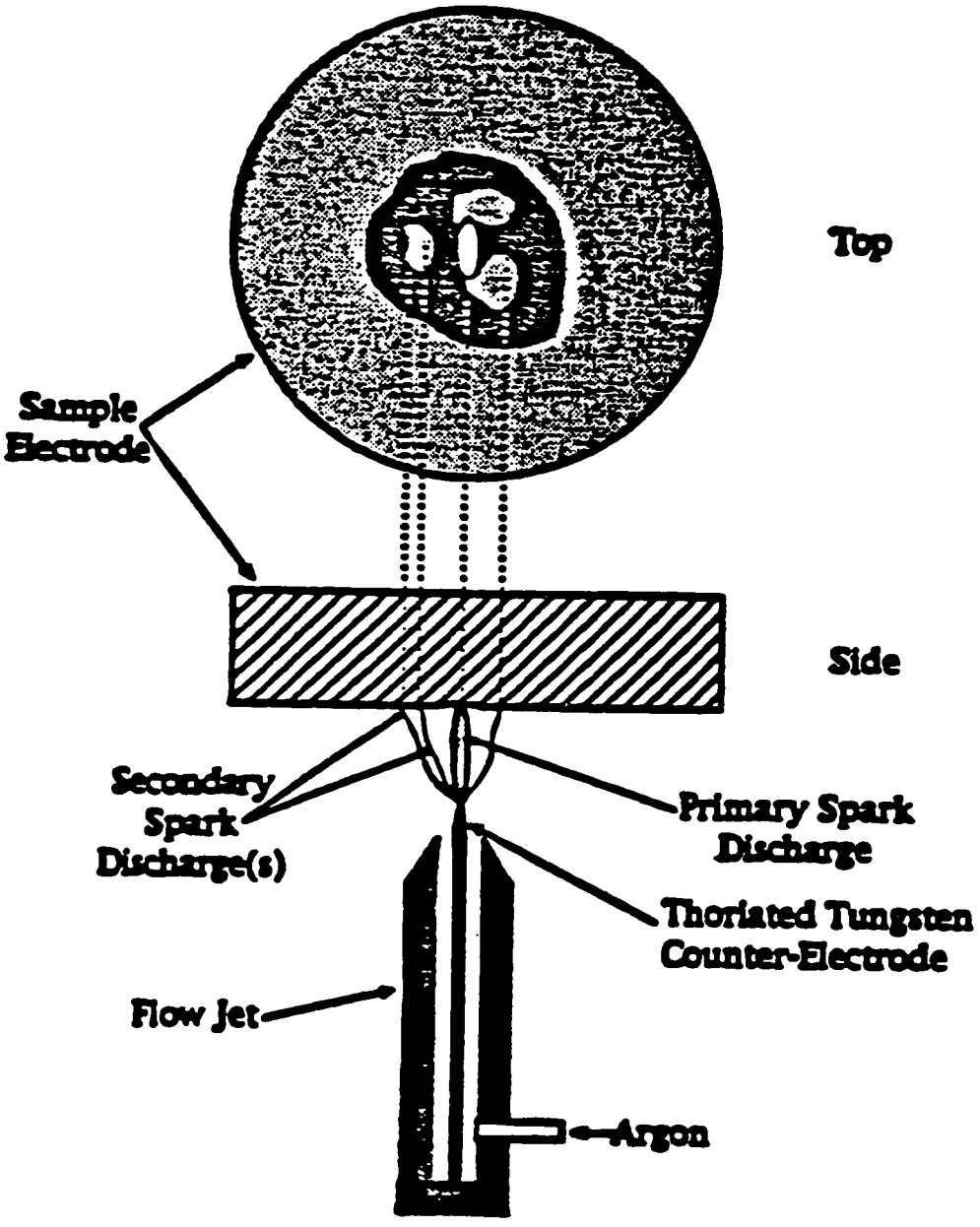

Figure 7. A typical sampling configuration of conventional spark sources.

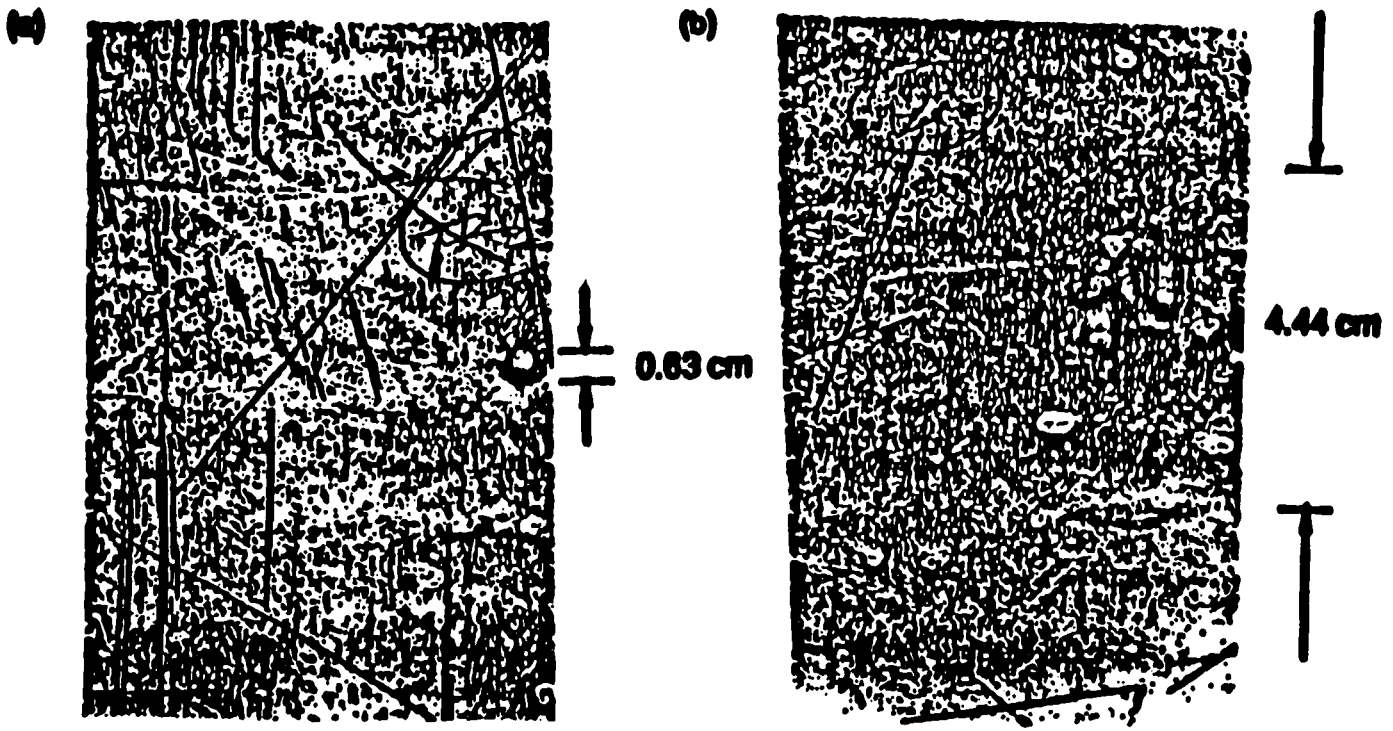

Figure 8. Actual burn patterns of the (a) "zero-bias" spark source and (b) conventional spark sources.

oxidized as shown in **Figure 8b**. In addition, the bias current sustained secondary discharge provides different sampling than the primary discharge. This is highly undesirable and provides poor test results. **Figure 8a** shows the results of the new "zero-bias" spark source (this is described in detail below). In this case the ablation occurs through the current waveform storage and "shaping" network allowing all of the energy of the spark to be concentrated on a small spot on the cathode.

A prototype-grade "zero-bias" spark source was developed by Coleman[25] in collaboration with the Perkin-Elmer Corporation. Looking at spark sources from 20, 30, and 50 years ago, Coleman determined that an "ideal" spark source is one where the circuit is divided into two separate sections: II) the spark "ignitor" circuit and IV) the current waveform storage and "shaping" network where each circuit is timed independently. The purpose is to accurately store the energy needed or desired to be dissipated in the spark discharge in Section IV and separately ionize or breakdown the gap with Section II. The concept of the "ideal" spark ablation device is shown in **Figure 9.** This approach can eliminate bias current and, as a result, a positionally stable discharge can be achieved. The current waveform storage and "shaping" network is first charged by an ablation current power supply (Section III) using constant current charging. The charge is stored by the storage and "shaping" network, and then the ablation current power supply is electronically removed from the circuit by means of a high impedance switching device. This stored charge, measured in joules or watt seconds, reflects the total energy dissipated during each spark cycle. Prior to breakdown, the spark gap between the counter-electrode and the sample electrode presents a very high impedance to the network. An ignition power supply (Section I) is connected through a switching device to the spark "ignitor" circuit. This produces a periodic, very short duration, high voltage pulse to ionize the spark gap, thereby lowering the impedance close to one ohm. This pulse is on the order of 50 kV, with a very low current flow of short duration (a few ns). Once the gap is broken down, the charge in the storage network will discharge it's

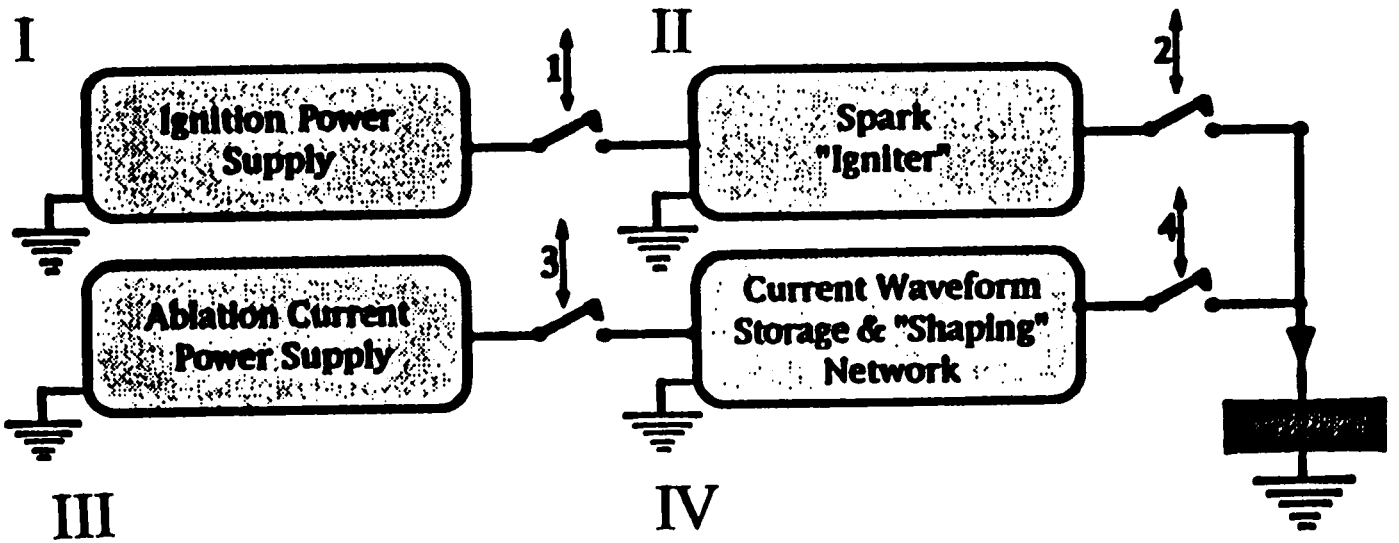

Figure 9. An "ideal" spark ablation concept device.

energy through the counter-electrode as a spark to ablate the sample.

Figure 10 shows the timing diagram of the "zero-bias" spark source. At time A, a master clock turns on for 10 μs. The master clock is off during the remainder of the cycle. At point A the ignition coil power supply turns off for approximately 40 μs, while the remainder of the cycle this power supply is on. Also, at this point in time, an ignition clock circuit opens the switch for the spark ignitor. There is a 30 μs delay as indicated.

The high voltage, low current, and a short duration energy pulse from the spark ignitor circuit is then used to ionize the spark gap. At this point a small controlled spark is generated. At point A the ablation current power supply is turned on for approximately 100 μs opening the "switch" to the current waveform storage and "shaping" network circuit. During the remainder of the cycle of operation the charge clock circuit closes the switch to maintain a flow of current from the power supply to the current waveform storage and "shaping" network. At point A the circuit is completely charged. After a delay of 30 μs this circuit is discharged. It provides a pulse between 10 and 200 amps (at 125-400 volts) for a duration of 5 μs. This is the duration of the spark during each cycle. The duration, voltage and current of each spark discharge can be carefully adjusted to control sample ablation. The circuit remains discharged for approximately 70 μs and is gradually charged again for a period of about 100 μs. The entire cycle is then ready to be repeated. The duration or frequency of the pulse for each spark discharge is adjusted to control the ablation. It directly determines the ablation process on the sample. This changes as the sample matrix is changed (e.g., aluminum *vs.* steel, etc.).

A simplified circuit of the "zero-bias" spark source is shown in **Figure 11**. The output pin of the master clock triggers the ignition clock and the charge clock. The charge clock is connected to the switching circuit for the current waveform storage and "shaping" network by means of an optical coupler and the ignitor clock is connected to the

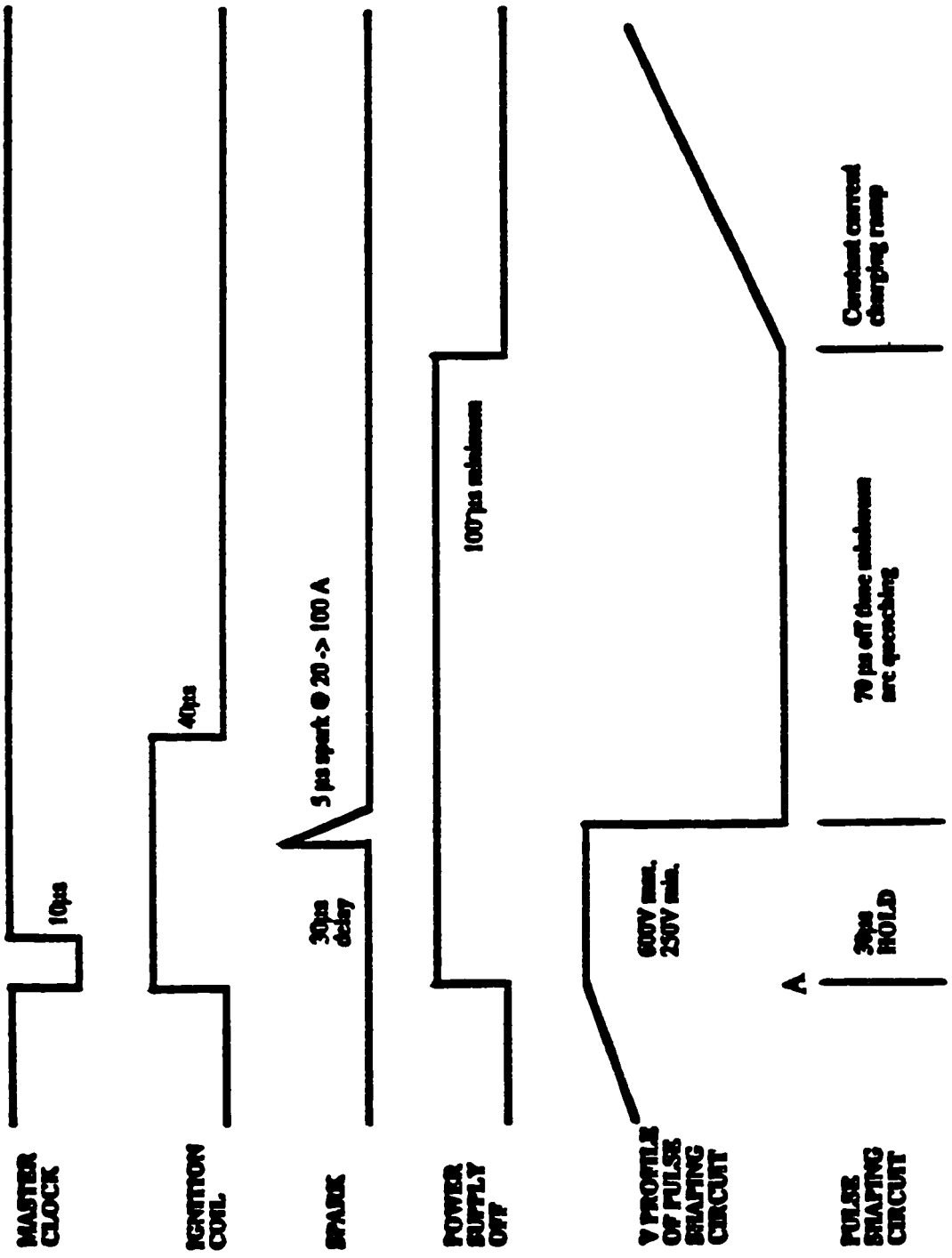

Figure 10. Timing diagram for the "zero-bias" spark source.

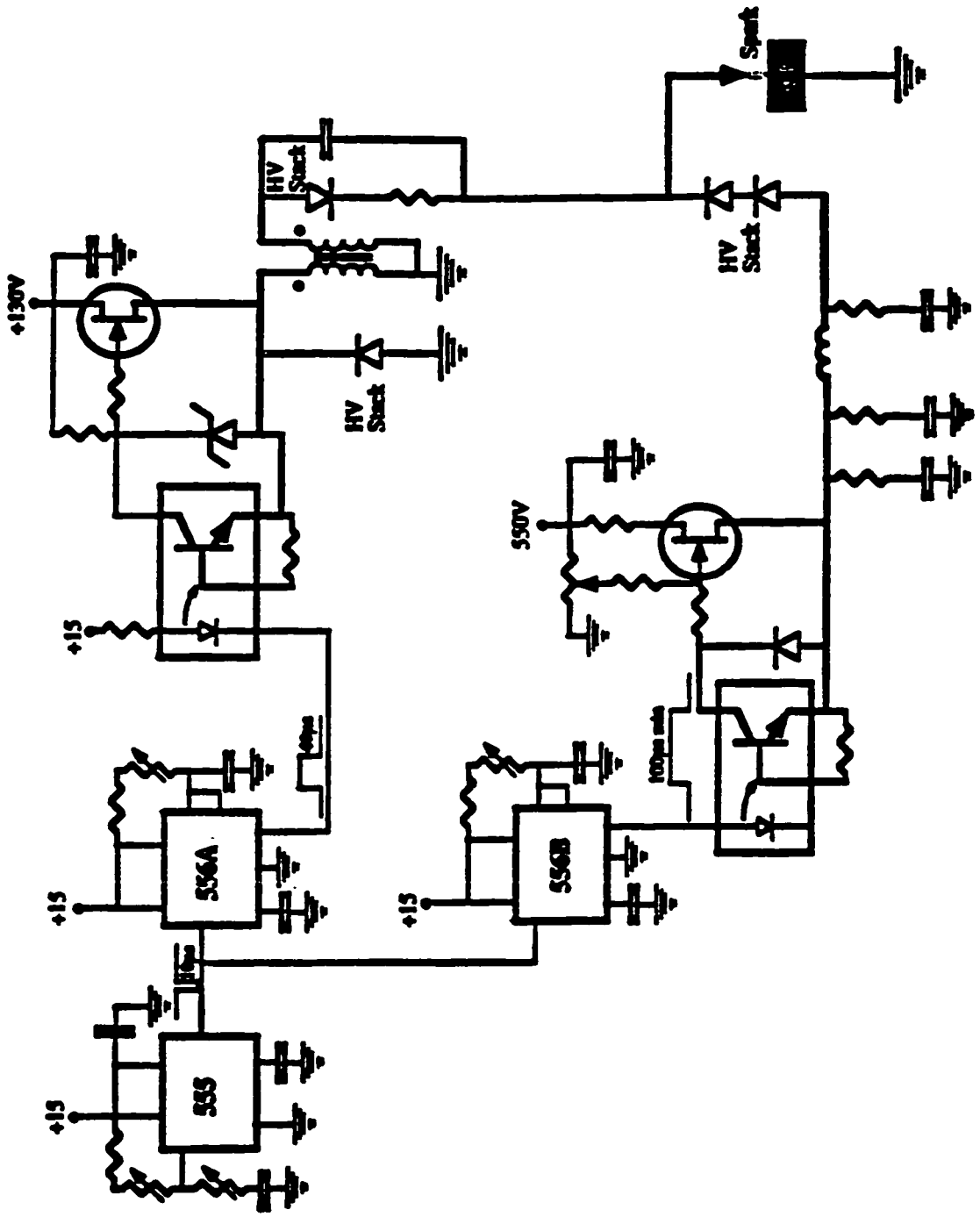

Figure 11. A simplified schematic diagram of the "zero-bias" spark source.

switching circuit for the spark "ignitor" circuit. These optical couplers isolate the power supply electrically so that there is no electrical noise between the two supplies. Solid-state field-effect n-channel HEXFET transistors (IRF50, International Rectifier) are used as the switching elements. The power is evenly distributed over the pulse by the arrangement of three capacitors in the current waveform and "storage" network. The two diodes in this section assure that the current is unidirectional and the electrode remains cathodic.

A 20K resistor within the spark 'ignitor" section limits the current to assure that the high voltage does not allow the sample to be ablated. This resistor, together with the capacitor and diode, prevents ablation of the counter-electrode instead of the sample electrode.

The counter-electrode is a thoriated tungsten pin which has been silver-soldered to a hollow brass body with a circular array of holes on the top surface. These pins are generally used in heli-arc welding apparatuses. The counter electrode is shown in **Figure 12**. Argon gas flows through the brass body and the array of holes supporting the electrical discharge while helping to positionally stabilize it. The samples generally used are 1 1/4 inch diameter disks or 1 1/4 inch square NIST (or other) standards. Sample preparation consists of using fine grit sand paper to provide a clean surface followed by rinsing with acetone.

The spark stand provides physical separation of the electrodes, allows precise adjustments to the interelectrode gap, and also provides an air-tight environment for the ablation process. An old spark stand (Thermo-Jarrell Ash, USA), shown in **Figure 13**, was used in these experiments. The counter-electrode was inserted through the bottom of the stand and was sealed with an o-ring. The tip of the electrode was contained within a convex ceramic body of the ablation chamber. An o-ring was placed into a groove located on top of the ceramic chamber to provide a seal between the chamber and sample. The sample was firmly held in place with an air piston.

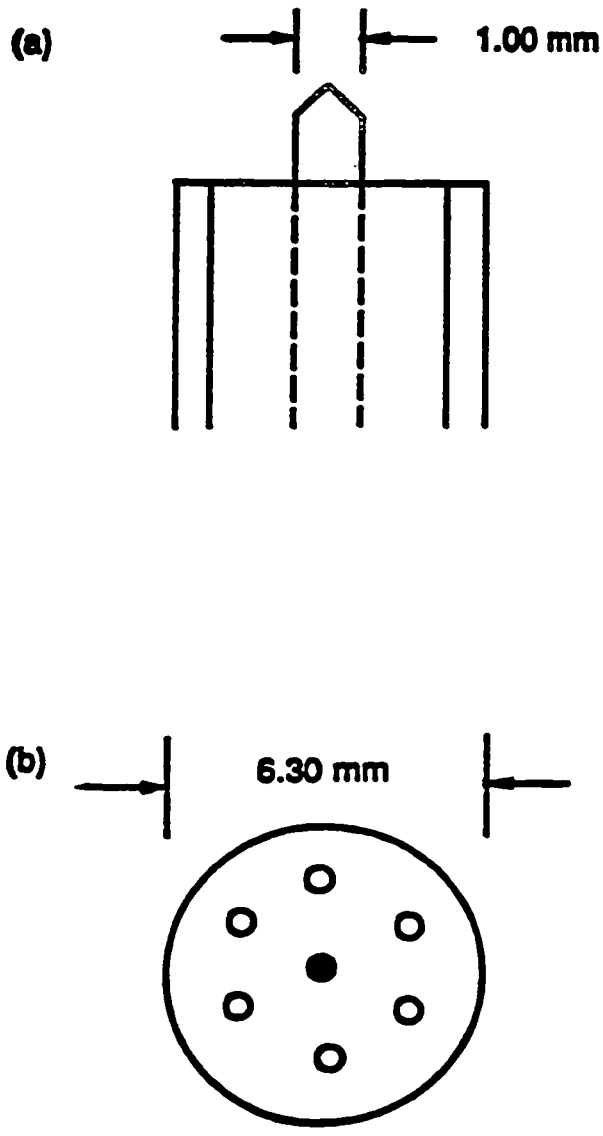

Figure 12. Counter-electrode for the "zero-bias" spark source, (a) side view and (b) top view.

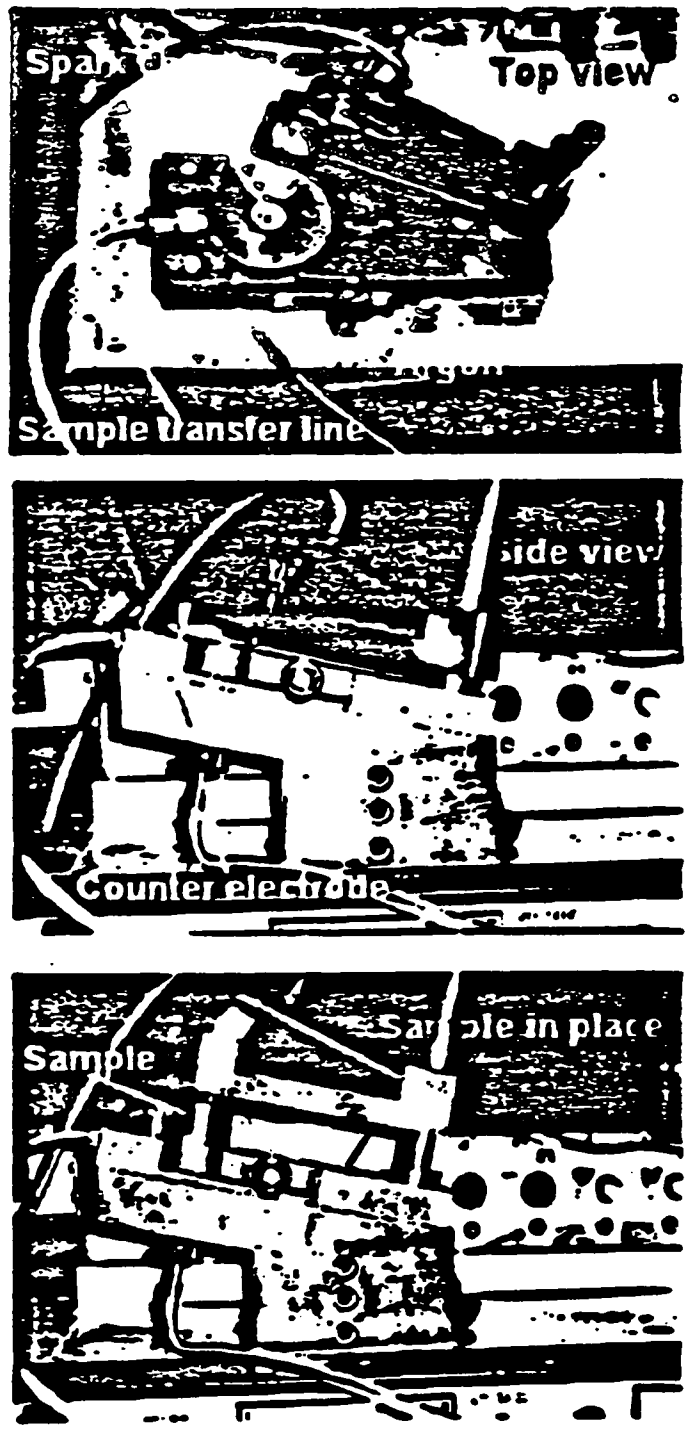

Figure 13. Spark stand used with the "zero-bias" spark source.

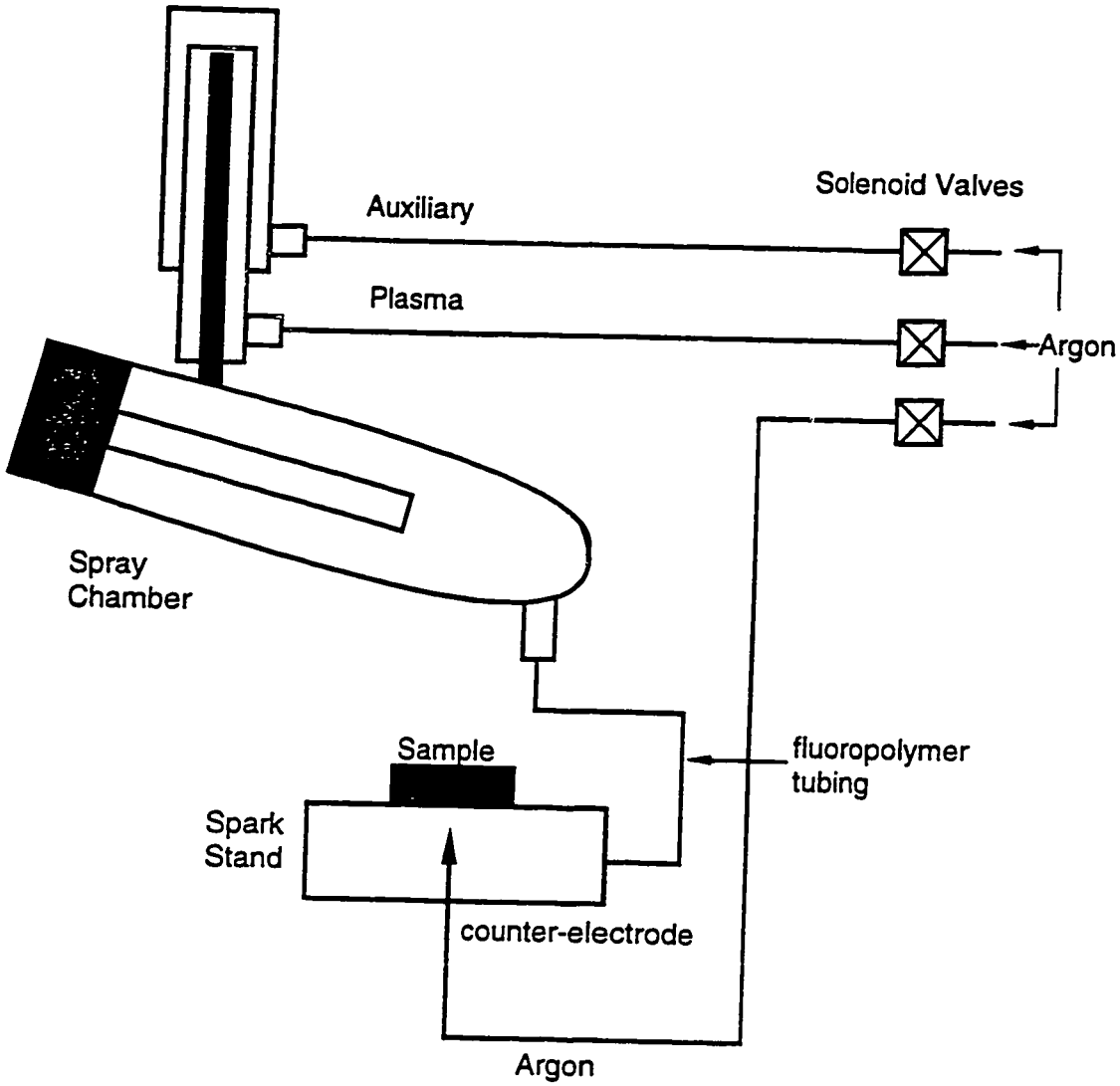

Figure 14. Interface of the spark source to the ICP-AES.

The interface of the spark source with the ICP-AES is shown in **Figure 14.** Argon is introduced into the spark chamber controlled and adjusted by the mass flow controller of the ICP-AES instrument. The ablated material is transported through approximately 2 meters of fluoropolymer tubing (1/4 inch i.d.). It has been shown[50] that analytical performance is relatively independent of the length of tubing, indicating that the fine aerosol generated is efficiently transported from the spark source to the ICP spray chamber and torch. The spray chamber is used to help stabilize the plasma and to provide a better flow of the ablated material. It also acts as a pneumatic buffer to help stabilize pressure differences. Particles too large to reach the plasma generally fall to the bottom of the spray chamber. Carry over effects are found to be minimal.

Chapter 3

General Concepts of Solid Spark Ablation

Introduction

Direct spark emission spectra are characterized as complex, line-broadened, and having high background levels. Analytical consequences include poor detection limits, short dynamic ranges, spectral interferences, and the need for complicated algorithms for quantitation.[43] They are also subject to self-absorption and/or self-reversal leading to apparent matrix effects.[14,43] It has been shown that significant improvements in detection limits and working curve linearity are evident in transporting ablated material from a spark source to an ICP for excitation.[47,61] Using the "zero-bias" spark source as a solid sampling device for ICP-AES enables separation of the processes of sampling and spectral excitation and to optimize each individually. Ideally the spark source should remove a sufficient amount of the sample to achieve adequate detection limits and should remove material in a uniform manner so that the aerosol reflects the sample composition. The intent of this research is to evaluate the new "zero-bias" spark source as a solid sampling device for ICP-AES.

Results and Discussion

Several preliminary experiments were done to evaluate spark source performance on a variety of samples including steel standards, brass standards, aluminum alloys, and gold standards. The experiments were designed to examine the new spark source coupled to an ICP-AES in terms of stability, accuracy, precision, and linearity. The operating parameters of the ICP are shown in **Table 1**. Manual integration time was used to insure that sampling was carried out at the same time for each run. This is described in more detail below. Operating parameters of the spark source are dependent on the sample matrices and are shown in **Table 2**. Optimization, carried out for each sample, will be described in more detail in subsequent chapters.

Analytical performance can be partially evaluated by time profiles, a plot of

Table 2. Operating Parameters for the "Zero-Bias" Spark Source.

Repetition Rate	**500-2,000 Hz**
Peak Current	**20-120 Amps**
Spark Duration	**5 μs (typical)**
Pseudo-Triangular Waveform	
Spark Bias Current	**≈ 0 Amps**
Argon Flow	**0.5-1.0 L/min**
Preburn	**30 seconds**

emission intensity *vs.* time. A few representative examples for the different sample matrices are shown in **Figures 15, 16, 17** and **18. Figure 15** shows a time profile of NIST SRM 1162 (low alloy steel). The composition in weight percent for Ti, V, and Sn is 0.037, 0.058, and 0.066, respectively. The spark source was discharging for approximately 20 minutes. A time profile for Alcoa Al Alloy 384 is shown in **Figure 16**. The composition in weight percent for Si, Mg, and Ti is 11.50, 0.10, and 0.05, respectively. The spark source was discharging for approximately 10 minutes for the aluminum. **Figure 17** shows a time profile of NIST SRM 1108 (brass alloy). The composition in weight percent for Zn, Mn, and Sn is 34.42, 0.025, and 0.39, respectively. The spark source was discharging for approximately 7 minutes. **Figure 18** shows a time profile for FAU 10 (high purity gold). The composition in μg/g for Ag, Mn, and Ti is 49.7, 64.3, and 2.6, respectively. The spark source was discharging for approximately 17 minutes for the gold.

The data indicate that spark sampling and concurrent spectral emission are stable over time. As shown, ignition of the "zero-bias" spark source results in a rapid increase in signal intensity from background levels. After a certain time, the signal intensity reaches a pseudo-steady state level, is constant for a few minutes, and then starts to decline. For this reason, the ICP is operated in the manual operational mode to insure that sampling occurs at the same time for each analysis. It also appears that minor constituents, *i.e.* tin, titanium, and vanadium, follow the major constituent (iron) in the

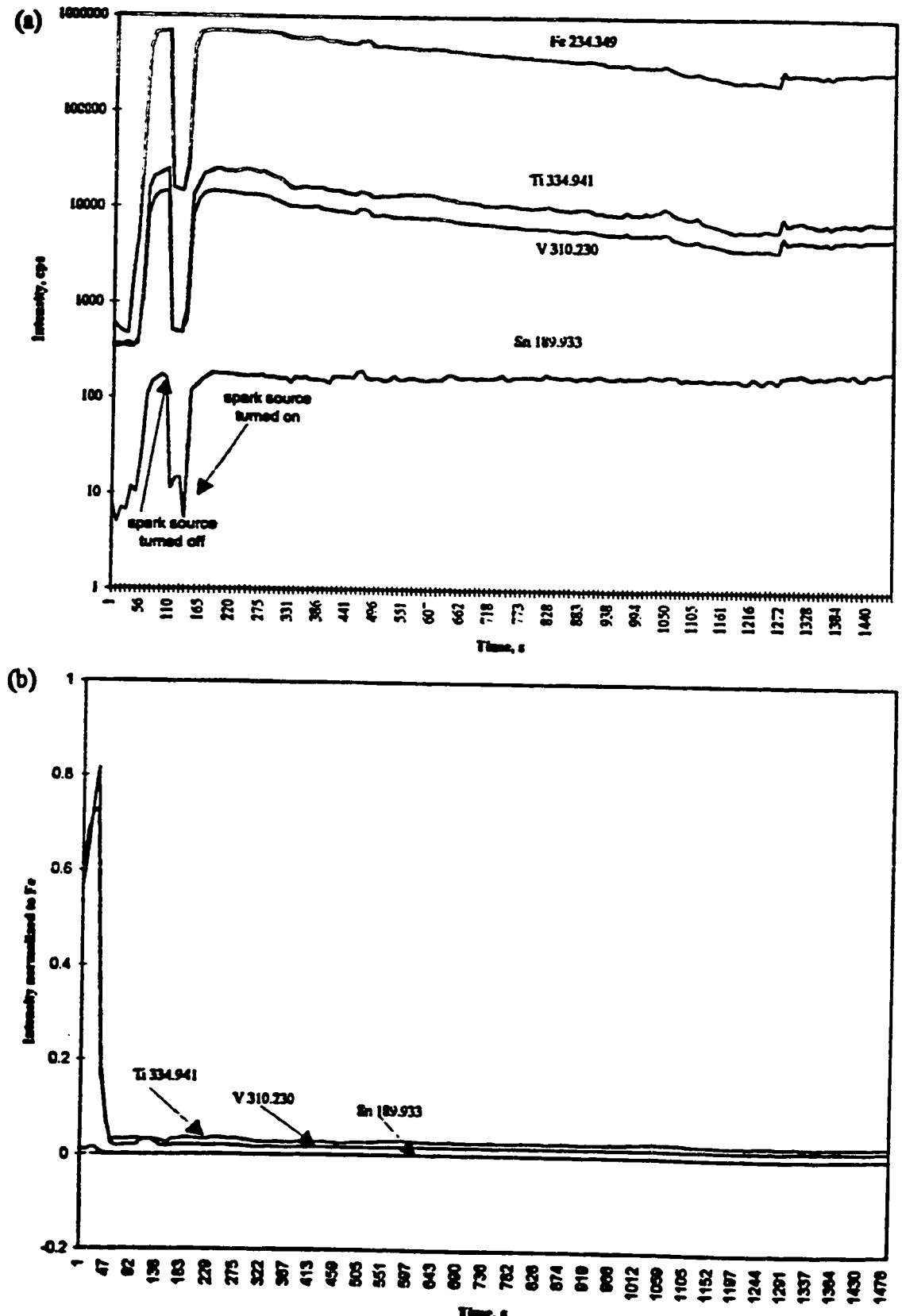

Figure 15. Time profile for specified elements during spark ablation of NIST SRM 1162.

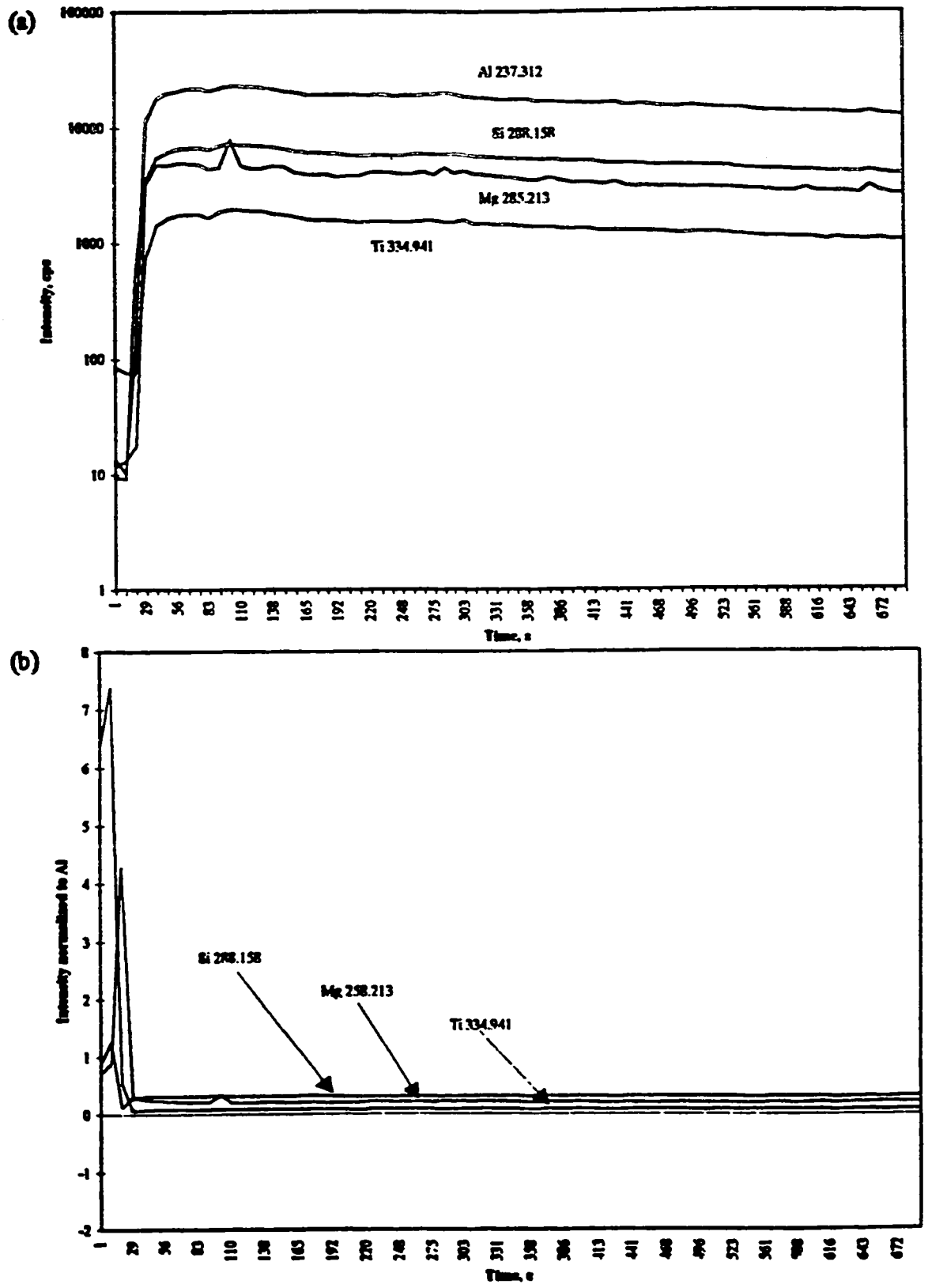

Figure 16. Time Profile for specified elements during spark ablation of Alcoa Aluminum Alloy 384.

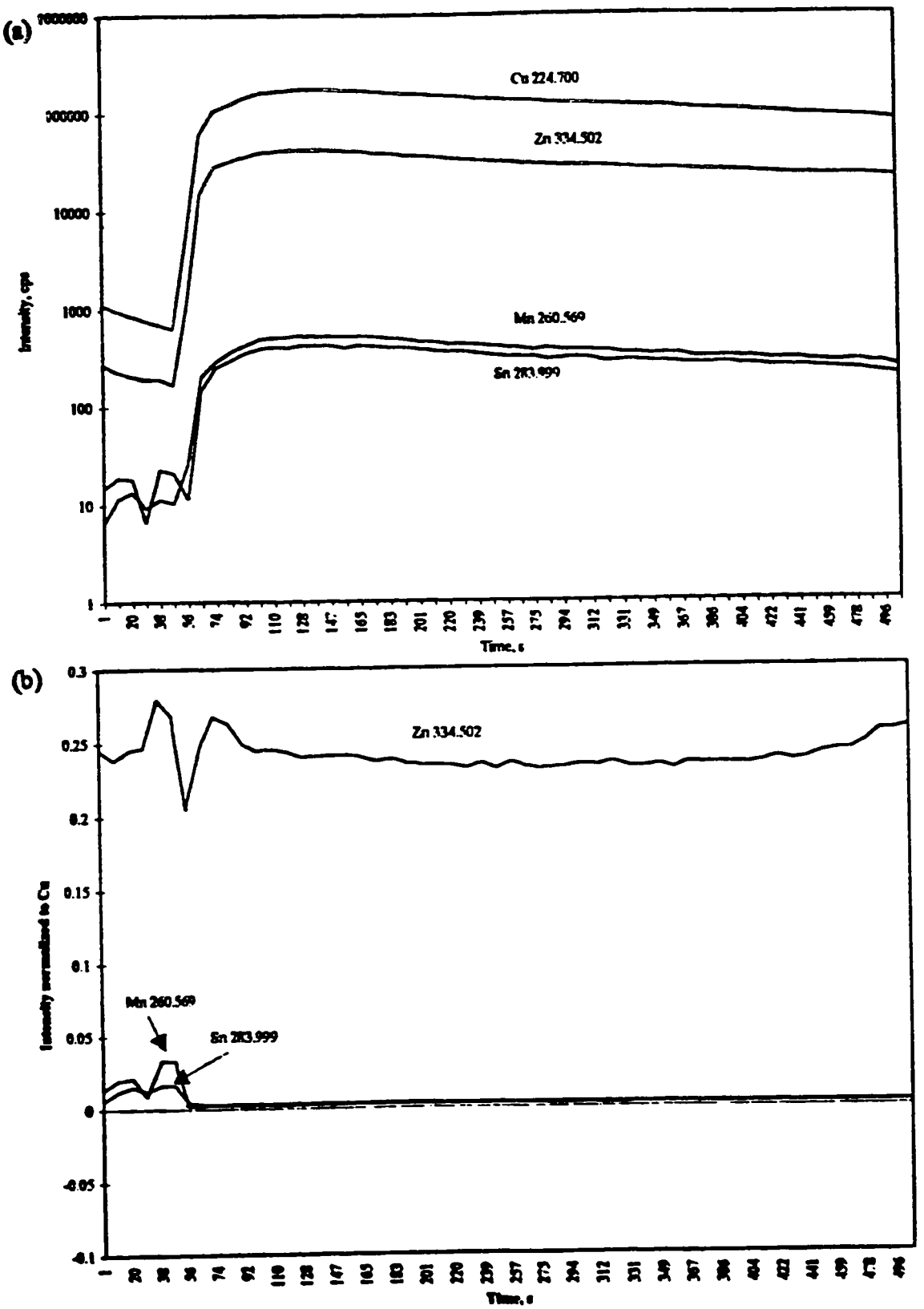

Figure 17. Time profile for specified elements during spark ablation of NIST SRM 1108.

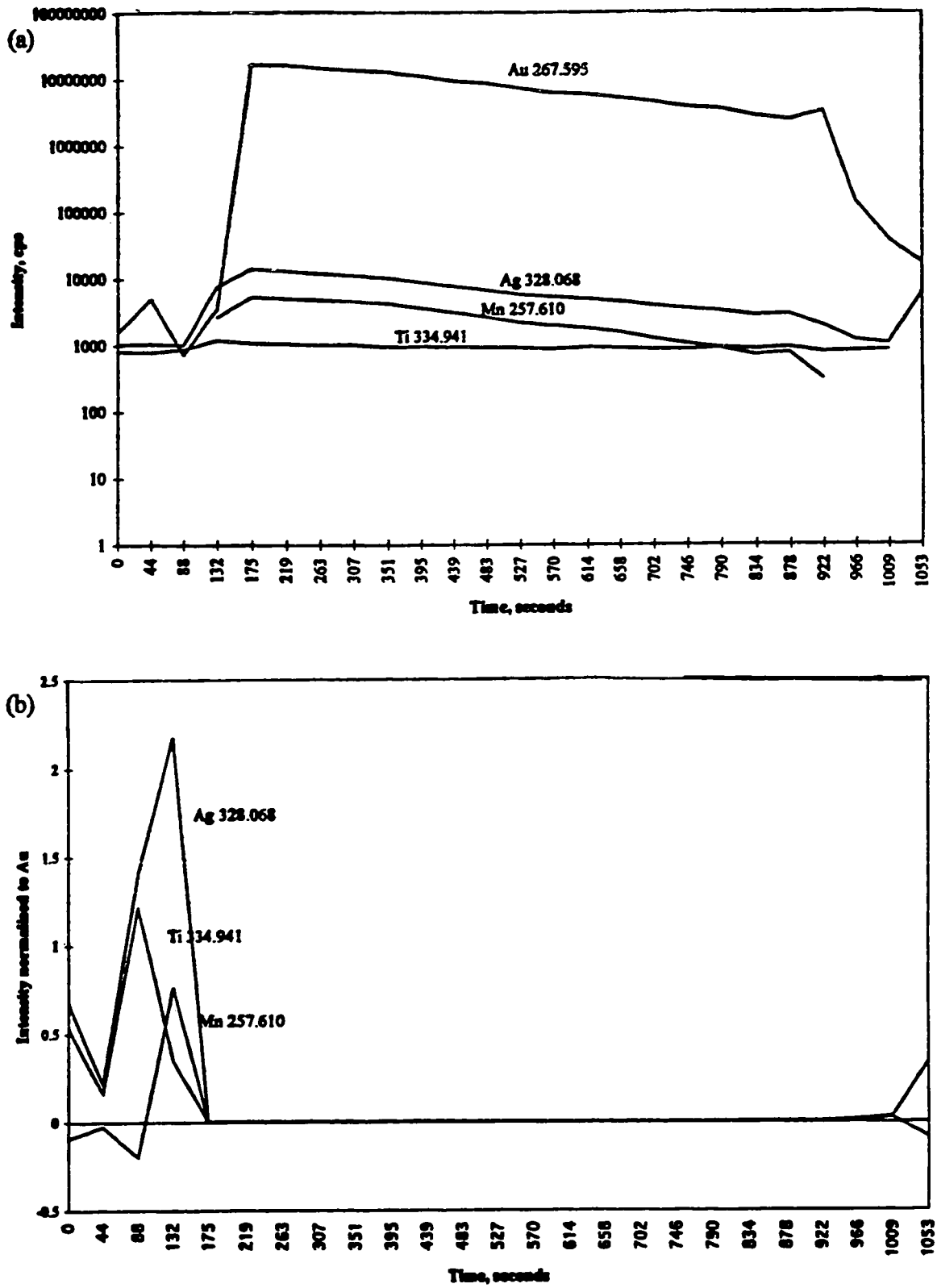

Figure 18. Time profile for specified elements during spark ablation of gold standard FAU 10.

case of NIST SRM 1162, low alloy steel. This is shown in **Figure 15**. Similar effects are seen for other sample matrices. These are readily seen when plotting the signal intensity for minor constituents normalized to the major constituent of the sample *vs.* time. As shown in **Figures 15B, 16B, 17B** and **18B**, essentially straight lines are obtained, indicating that the elements generally tend to track each other.

Two different experiments were carried out to measure spark reproducibility. In the first case, "readbacks" were performed where the ICP was "calibrated" using a one-point calibration based on the standard. Following standardization, this "standard" is read as a "sample" for ten separate burns, each burn being located at a different location on the standard. Reported values are given in terms of concentration. Representative data are shown in **Tables 3, 4, 5** and **6**. In the second case, ten different burns were carried out at ten different locations on the sample. Hence, the reported values are detector generated counts per second. **Tables 7, 8, 9** and **10** show representative data. Accuracy and precision are generally acceptable with most RSDs in the 0.5 to 5% range. In cases where the RSDs are larger, generally only small amounts of alloying constituents are present. The poor precision and accuracy of some of the constituents of gold standards will be explained in more detail later. In both sets of experiments, a "preburn" of 30 s was carried out for each sample to allow the spark source to achieve a pseudo-steady state and for the ablated material to reach the ICP-AES. A less sensitive spectral line of the major constituent of each sample was used as an internal standard to help accommodate for the amount of aerosol reaching the plasma.

The analytical utility of the "zero-bias" spark sampling/ICP-AES combination was evaluated with calibration curves, of emission intensity *vs.* concentration. Representative curves for each sample matrix are shown in **Figures 19, 20, 21** and **22**. Each determination for the steel and brass standards represents an average of three runs, while ten runs were carried out for the aluminum alloys. Error bars are based on the standard deviation of these runs. Linearity is seen with major constituents, (**Figures**

Table 3. "Readback" of BAS SS 407, Low Alloy Steel.

Element	Wavelength	elemental composition (ppm)	mean (ppm)	% RSD
C	193.018	4700	4734.1	0.51
Si	288.158	5900	5733.9	2.02
Mn	260.569	470	464.7	0.80
P	214.914	300	302.0	0.19
S	180.669	100	117.2	11.20
Cr	205.552	29500	29581.6	0.19
Mo	281.615	7800	7493.1	2.84
Ni	231.604	5900	5728.3	2.09
Cu	324.754	5700	5651.6	0.60
V	310.238	1800	1752.6	1.89

Table 4. "Readback" of Alcoa Aluminum Alloy 2024.

Element	Wavelength	elemental composition (ppm)	mean (ppm)	% RSD
Si	288.158	2000	2083.6	2.89
Fe	259.940	3500	3625.2	2.48
Cu	327.396	46000	45906.1	0.14
Mn	257.610	6500	6536.1	0.39
Mg	285.213	16000	15920.0	0.35
Cr	357.869	600	596.5	0.41
Ni	221.647	400	441.0	6.89
Zn	334.502	1000	1033.2	2.31
Ti	334.941	300	311.3	0.41

Table 5. "Readback" of NIST SRM 1103, Free Cutting Brass.

Element	Wavelength	elemental composition (ppm)	mean (ppm)	% RSD
Cu	221.458	592700	591382.2	0.16
Zn	334.502	357000	366443.2	1.85
Pb	220.353	37300	34614.6	5.28
Sn	283.999	8800	8414.0	3.17
Fe	238.204	2600	2604.8	0.13
Ni	231.604	1600	1627.0	1.18
P	177.428	30	28.9	2.64

Table 6. "Readback" of FAU 10, Fine Gold Reference Material.

Element	Wavelength	elemental composition (ppm)	mean (ppm)	% RSD
Ag	328.068	49.7	50.6	4.14
As	228.812	29.4	36.6	15.36
Bi	223.061	53.9	47.9	8.29
Cr	205.552	4.9	3.9	15.83
Cu	324.754	9.8	15.2	30.55
Fe	238.204	90.4	98.1	5.80
Mg	279.079	3.2	3.4	5.04
Mn	257.610	64.3	63.2	1.18
Ni	231.604	14.6	15.3	3.31
Pb	220.353	49.7	45.6	6.08
Pd	340.458	119.0	123.0	2.34
Si	251.611	9.0	9.4	3.30
Sn	235.484	49.7	41.1	13.45
Ti	334.941	2.6	2.5	2.21
Zn	334.502	20.9	21.3	1.23

Table 7. Relative Intensities Obtained During Spark Ablation of BAS SS 70, Ferritic Stainless Steel.

Element	Wavelength	elemental composition (wt. %)	mean (cps)	% RSD
C	193.018	0.18	785.66	5.97
Si	288.158	0.35	1827.24	3.59
P	214.914	0.024	25.56	4.68
Mn	260.569	0.038	18476.55	1.26
Cr	205.552	16.35	43235.85	1.43
Ni	231.604	0.40	1062.02	1.08

Table 8. Relative Intensities Obtained During Spark Ablation of Alcoa Aluminum Alloy 3003.

Element	Wavelength	elemental composition (wt. %)	mean (cps)	% RSD
Si	288.158	0.20	121.38	2.26
Fe	259.940	0.50	1021.96	2.24
Cu	327.396	0.15	2557.35	1.45
Mn	257.610	1.20	9492.42	0.43
Mg	285.213	0.03	1659.62	1.52
Zn	334.502	0.08	78.20	1.86
Ti	334.941	0.02	647.40	1.22

Table 9. Relative Intensities Obtained During Spark Ablation of NIST SRM 1107, Naval Brass.

Element	Wavelength	elemental composition (wt. %)	mean (cps)	% RSD
Cu	224.700	61.21	204834.12	4.43
Zn	334.502	37.34	75031.09	2.19
Pb	220.353	0.18	122.23	5.72
Fe	238.704	0.037	177.58	4.19
Sn	283.999	1.04	1379.69	1.45
Ni	231.604	0.098	201.73	1.59

Table 10. Relative Intensities Obtained During Spark Ablation of FAU 8, Fine Gold Reference Material.

Element	Wavelength	elemental composition (μg/g)	mean (cps)	% RSD
Ag	328.068	81.7	23489.74	2.2
As	188.979	18.0	22.35	35.0
Bi	223.061	34.0	223.51	13.0
Cr	205.552	13.3	249.87	9.5
Cu	324.754	46.9	10038.15	11.2
Fe	238.204	33.8	364.05	9.6
Mg	279.079	11.8	208.11	10.4
Mn	257.610	22.5	1890.65	1.6
Ni	232.003	50.5	674.35	4.5
Pb	220.353	30.5	13.26	52.7
Pd	340.458	19.8	353.41	1.9
Si	288.158	27.8	221.76	17.1
Sn	235.484	27.2	31.55	45.8
Ti	334.941	25.3	2889.06	3.0
Zn	334.502	6.6	1678.53	1.2

Table 11. Correlation Coefficients for NIST SRM Series 1161-1168, Low-Alloy Steel.

Element	Wavelength	Correlation Coefficient	Concentration Range (wt. %)
C	193.018	0.965	0.037-0.54
Si	288.158	0.997	0.025-0.48
Cu	324.754	0.996	0.019-0.47
Ni	231.604	0.999	0.026-1.73
Cr	205.552	0.999	0.004-0.74
Mo	281.615	0.999	0.005-0.30
Sn	189.933	0.979	0.001-0.10
Ti	334.941	0.998	0.004-0.26
W	207.911	0.970	0.001-0.20
Zr	343.823	0.999	0.002-0.20
Nb	269.706	0.986	0.001-0.29
Ta	226.230	0.958	0.001-0.23
Al	309.271	0.994	0.005-0.19

Table 12. Correlation Coefficients for Alcoa Aluminum Wrought Alloys.

Element	Wavelength	Correlation Coefficient	Concentration Range (wt. %)
Si	288.158	0.957	0.03-1.00
Fe	259.940	0.952	0.05-0.50
Cu	327.396	0.999	0.04-2.60
Mn	257.610	0.983	0.01-1.20
Zn	334.502	0.999	0.01-5.40
Ti	334.941	0.898	0.01-0.06

Table 13. Correlation Coefficients for NIST SRM Series 1100-1102, Optical Emission & X-ray Spectroscopic Analysis Standards .

Element	Wavelength	Correlation Coefficient	Concentration Range (wt. %)
Ag	328.068	0.965	0.001-0.019
Al	309.271	0.999	0.0006-0.008
Be	234.861	0.997	0.00003-0.015
Ni	231.604	0.999	0.005-0.052

Table 14. Correlation Coefficients for Fine Gold Reference Materials.

Element	Wavelength	Correlation Coefficient	Concentration Range (μg/g)
Ag	328.068	0.998	7.1-81.7
Bi	223.061	0.835	3.4-53.9
Cr	205.552	0.987	1.7-32.6
Cu	324.754	0.943	1.6-98.1
Fe	238.204	0.965	6.2-90.4
Mg	279.079	0.987	1.1-34.0
Ni	231.604	0.993	2.7-50.5
Pb	220.353	0.963	1.9-49.7
Pt	213.423	0.920	5.1-87.1
Si	288.158	0.987	2.7-27.8
Sn	189.933	0.962	2.8-49.7
Ti	334.941	0.996	0.7-25.3
Zn	213.856	0.937	2.6-54.6

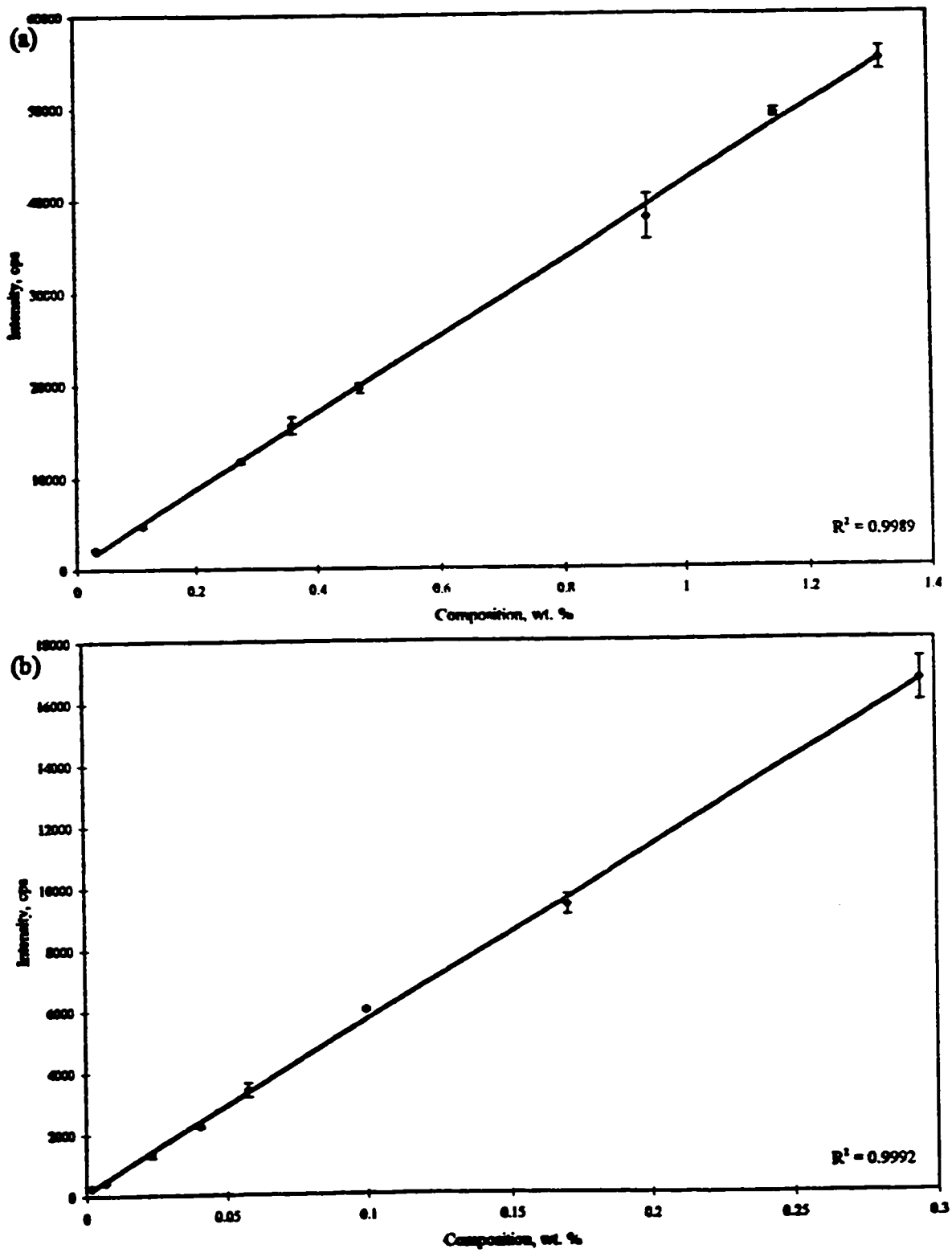

Figure 19. Calibration curves for (a) Mn 260.569 and (b) V 310.230 of NIST SRM series 1161-1168, Low Alloy Steels.

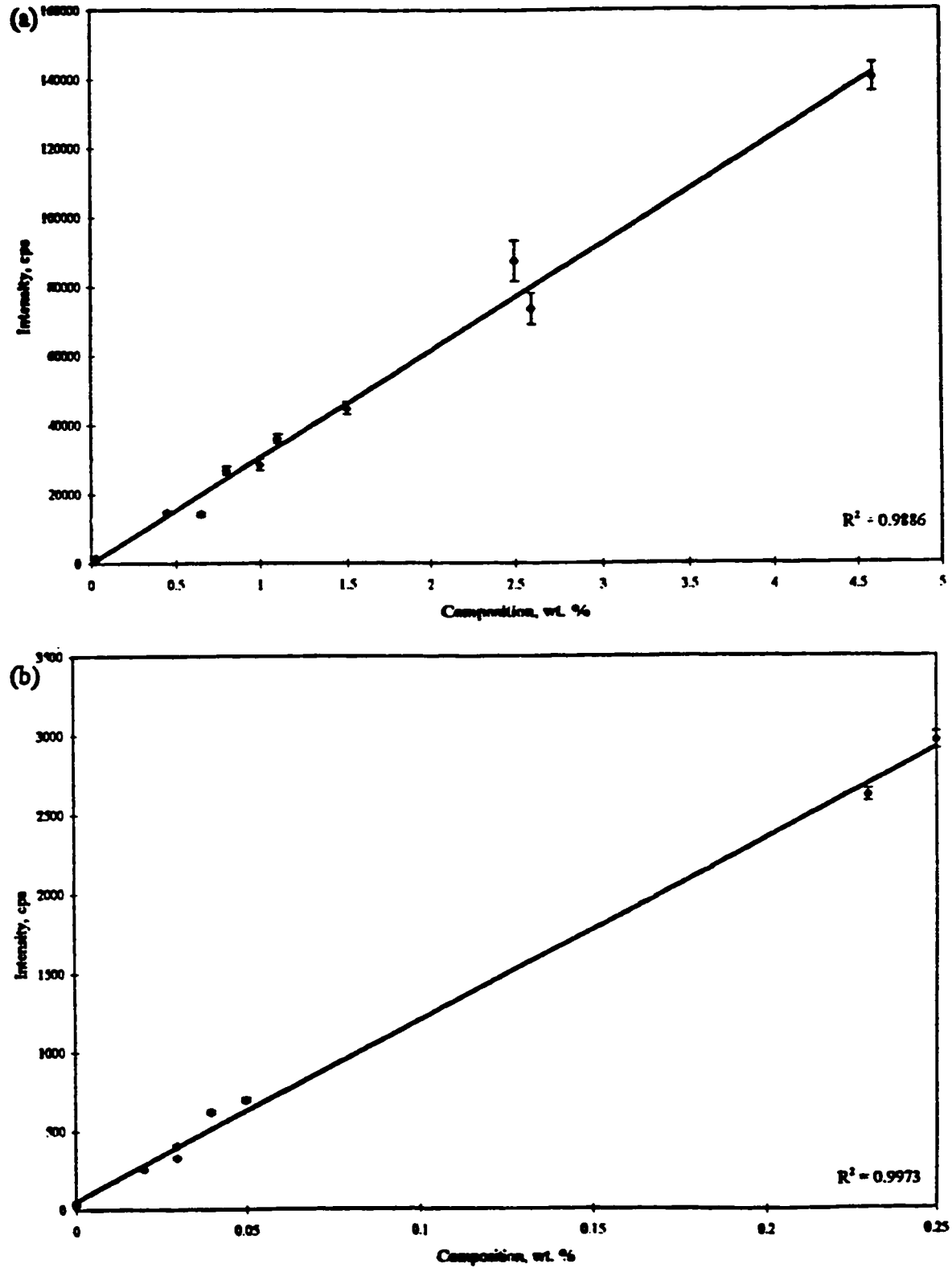

Figure 20. Calibration curves for (a) Mg 285.213 and (b) Cr 357.869 of Alcoa Aluminum Wrought Alloys.

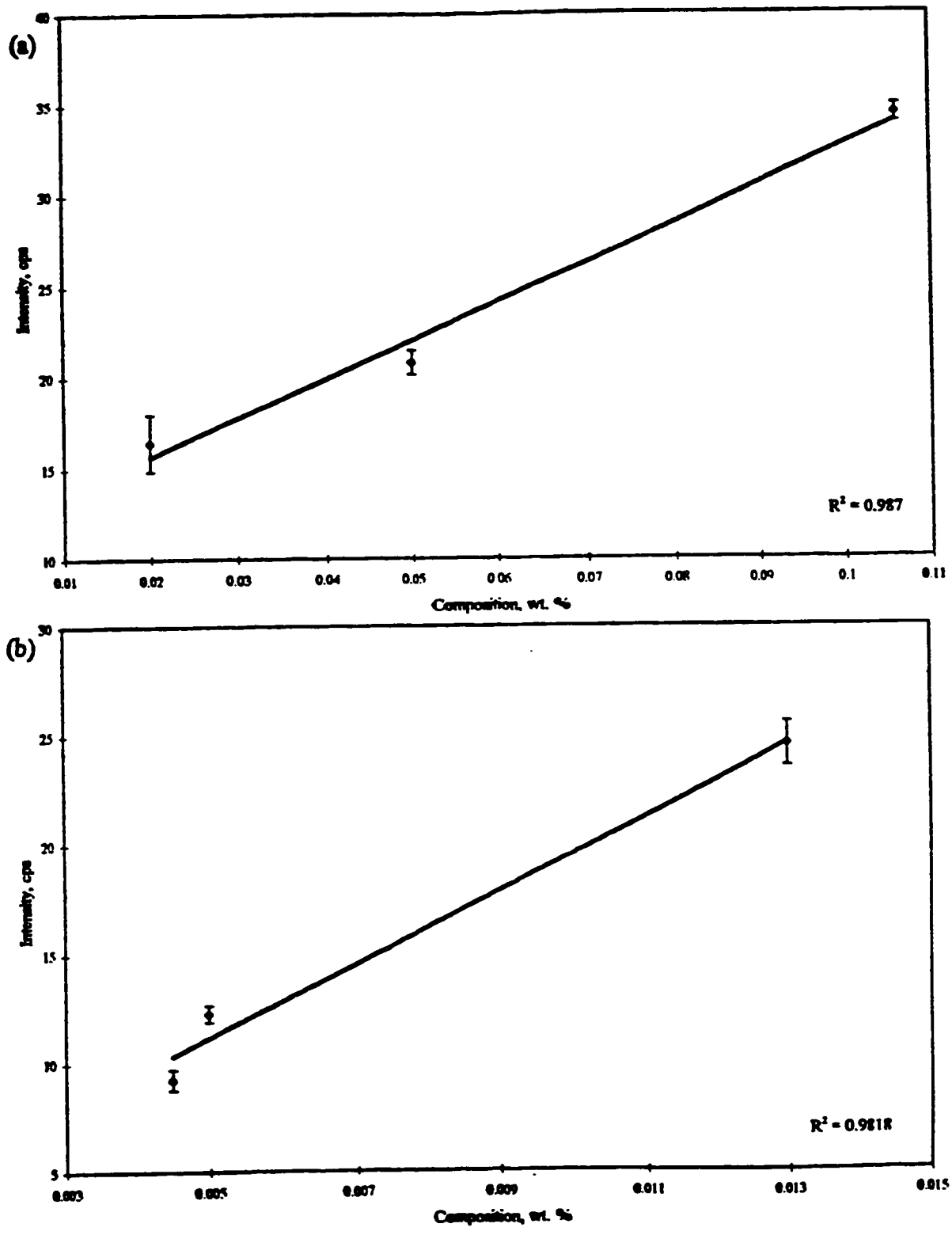

Figure 21. Calibration curves for (a) Pb 220.353 and (b) Cd 228.802 of NIST SRM series 1100-1102, Optical Emission & X-Ray Spectroscopic Analysis Standards.

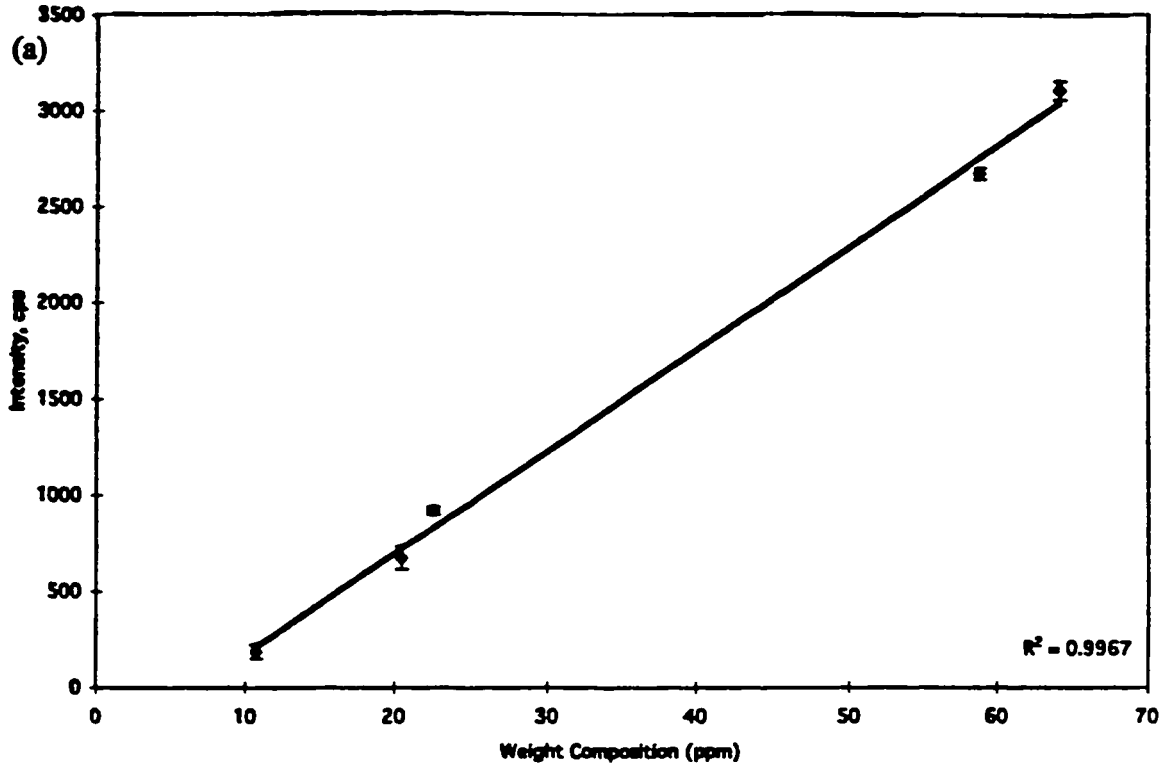

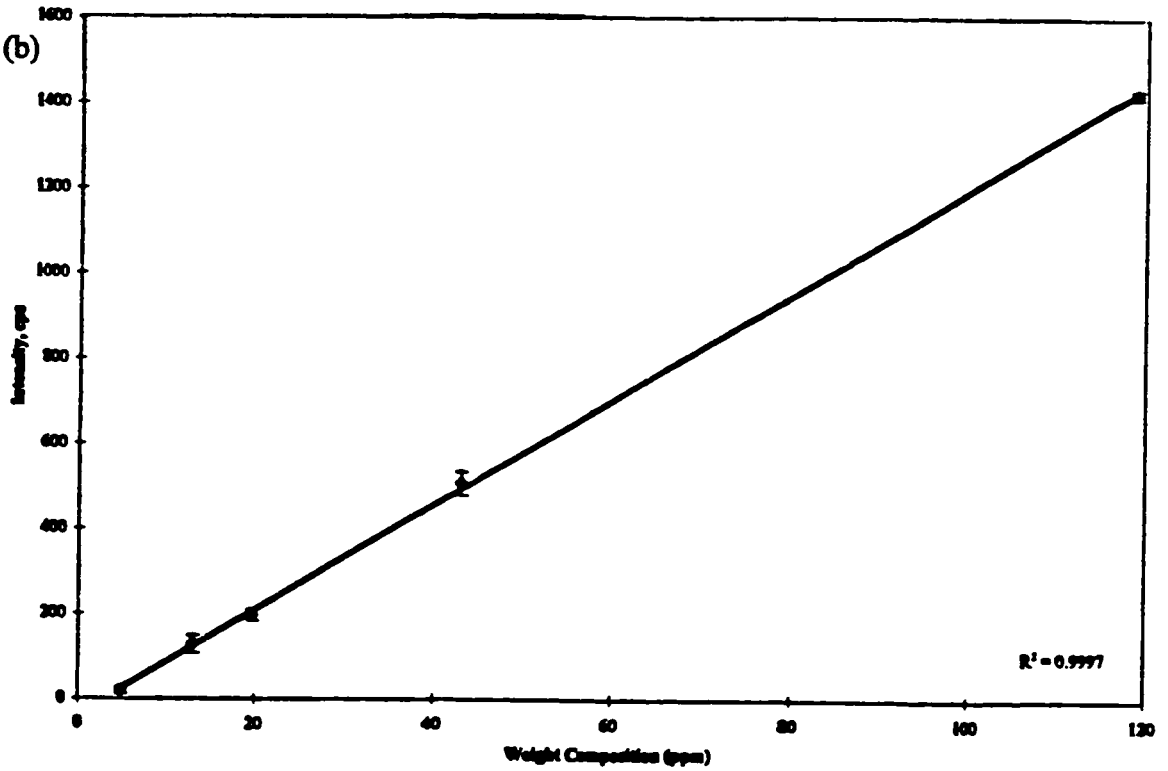

Figure 22. Calibration curves for (a) Mn 257.610 and (b) Pd 340.548 of Fine Gold Reference Materials.

19A, and **20A**) minor constituents, (**Figures 19B**, **20B**, and **21A**) and trace constituents, (**Figures 21A**, **22A** and **22B**). There are only three standards in the brass series. **Tables 11**, **12**, **13** and **14** show results for the remaining elements in the series, including their concentration ranges and correlation coefficients. Correlation coefficients of 0.95 or better are typically observed. These data indicate that full quantization of the individual sample is likely.

From these experiments it is apparent that the "zero-bias" spark source can be used as a solid-sampling device for ICP-AES. A variety of matrices (steel, brasses, aluminum, and gold, etc.) have been sampled for rapid multi-element quantitative analysis. Accuracy and precision of the technique are both within a few percent. Excellent detection limits and analytical linearity are possible.

Chapter 4

The Analysis of Steel Samples

Introduction

As noted earlier, the "zero-bias" spark source was developed by Coleman in collaboration with the Perkin-Elmer Corporation. The purpose of this project was the fundamental and applied research of the "zero-bias" spark source used as a solid sampling device for ICP-AES. Stability, accuracy, precision, and linearity of the new spark source coupled to an ICP-AES were discussed previously. A variety of sample matrices including steel, brass, aluminum, and gold standards were analyzed in order to test the versatility of the spark source. The first phase of developing the spark source is largely complete. Subsequent refinement is expected to result in the introduction of the spark source in a commercially available instrument. The next four chapters will discuss, in detail, studies carried out for each of these sample matrices.

Results and Discussion

As stated previously, application of the spark ablation device to generate an aerosol from a solid sample for introduction in ICP spectrometry allows separation of the sampling and excitation processes. In separating these two events, both are individually optimized to give enhanced performance. Spark source parameters optimized for the sampling process include repetition rate, peak current waveform, and argon flow rate. ICP parameters optimized for the excitation process include the RF power and the integration time. Optimized samples are dependent on the sample matrix and were carried out for each sample matrix.

When optimizing parameters, the most abundant element, a major and a minor constituent were all analyzed in order to choose optimal parameters for most elements. **Figures 23** and **24** show plots of RF power *vs.* intensity for the BAS SS stainless steel series. **Figure 23** shows a minor constituent, Mn 260.569, which has a weight composition of 0.41% and **Figure 24** shows a major constituent, Cr 267.716, which has

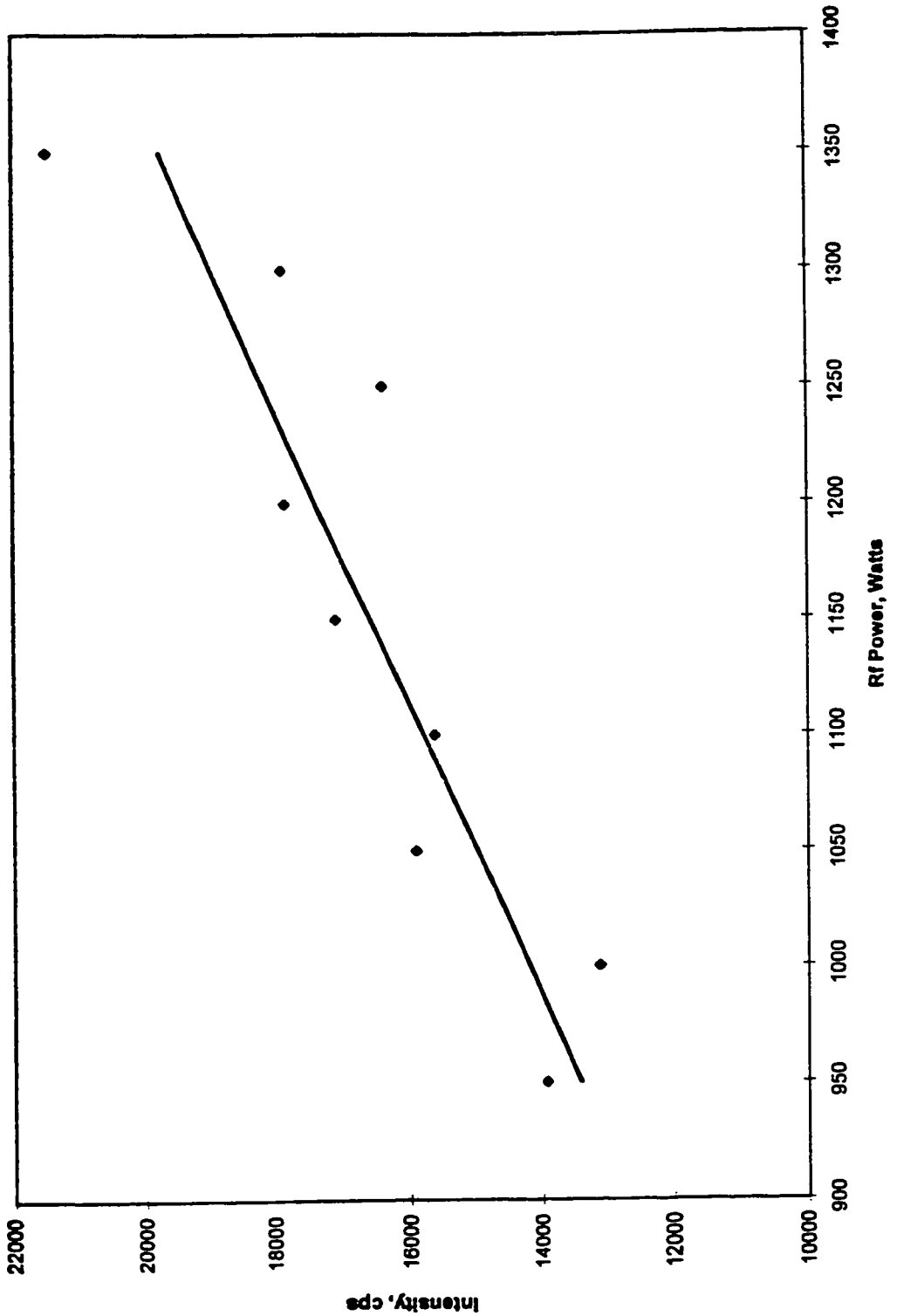

Figure 23. Optimizing RF power for BAS SS stainless steel series, Mn 260.569.

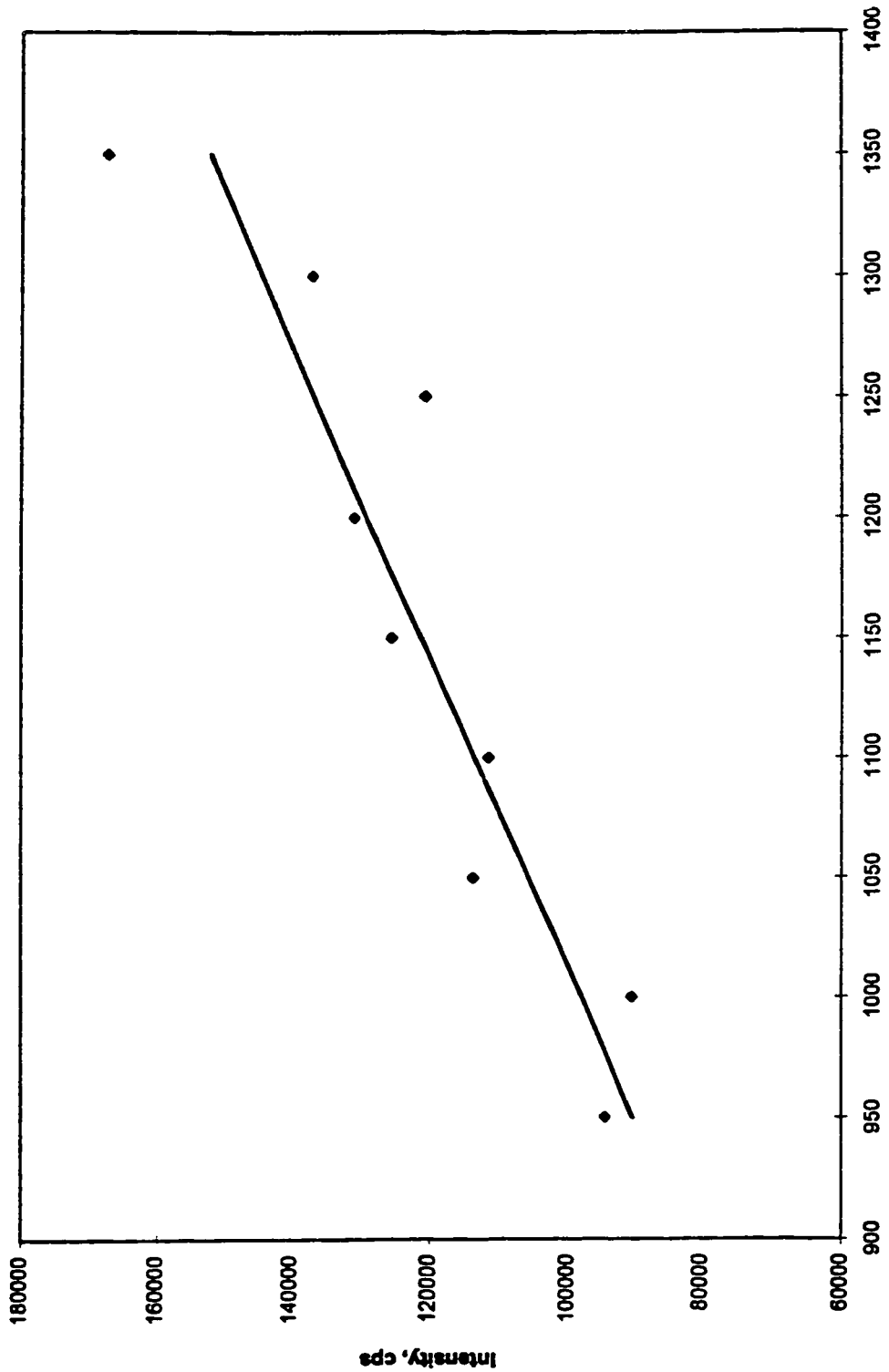

Figure 24. Optimizing RF power for BAS SS stainless steel series, Cr 267.716.

a weight composition of 12.40%. As would be expected the intensity increases for each element as a result of RF power increases. An RF power of 1200 Watts was chosen for safety reasons and to prolong the lifetime of the power amplifier tube of the ICP. The net effect of flow rate on the signal intensity was investigated. A plot of argon flow rate *vs.* intensity for BAS SS stainless steel series is shown in **Figures 25** and **26**. Both of the plots show that the maximum signal was obtained at a flow rate of 0.5 L/min. Therefore, a flow rate of 0.5L/min. was considered optimal and was used for the remaining experiments. At higher flow rates, the residence time (amount of time the sample is in the plasma) is shorter causing decreased intensity. **Figure 27** shows the effect of nebulizer flow rate on residence time. A flow rate that is low causes the sample to remain in the preheating zone or initial radiation zone of the plasma, below the reading area. A flow which is too high causes the sample to be carried to the tail plume of the plasma where oxides form with the sample. **Figure 28** shows the zones of the plasma. PHZ is the preheating zone where the solid particles go through sublimation. IRZ is the initial radiation zone in which atomization occurs. Ionization occurs in the NAZ or normal analytical zone. Viewing of the photons takes place in this zone.

The repetition rate of the spark source was found to have a strong effect on the analyte signal of the ICP-AES. This may be due to a change in the dominant sampling mechanism to melting and evaporation of molten areas.[48] Watters *et al.*[23] found that the aerosol number density increases as the repetition rate increases. Although initial sampling efficiency decreases after a period of time, melting becomes important. **Figure 29** shows the dependence of spark parameters on analytical characteristics of the ablation process for BAS SS stainless steel series for Mn 260.569. Higher peak current settings result in an increase in sample removal from the surface, although precision of the measurement at higher currents is low. The signal increases at higher frequencies, although high frequency settings result in unstable discharges and sample overheating. The % RSD values are from 20 readings on the ICP while the spark source was on

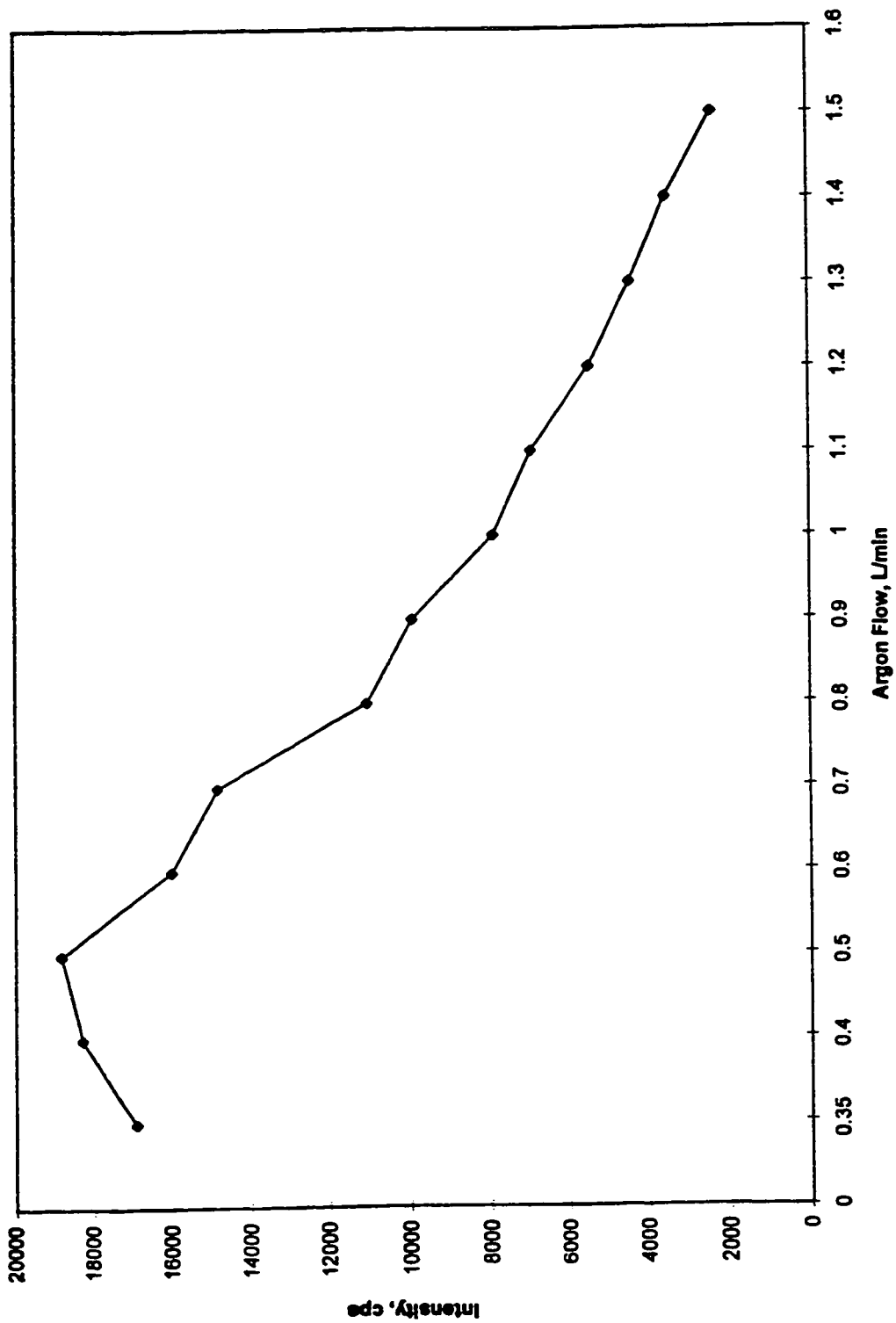

Figure 25. Optimizing argon flow rate for BAS SS stainless steel series, Mn 260.569.

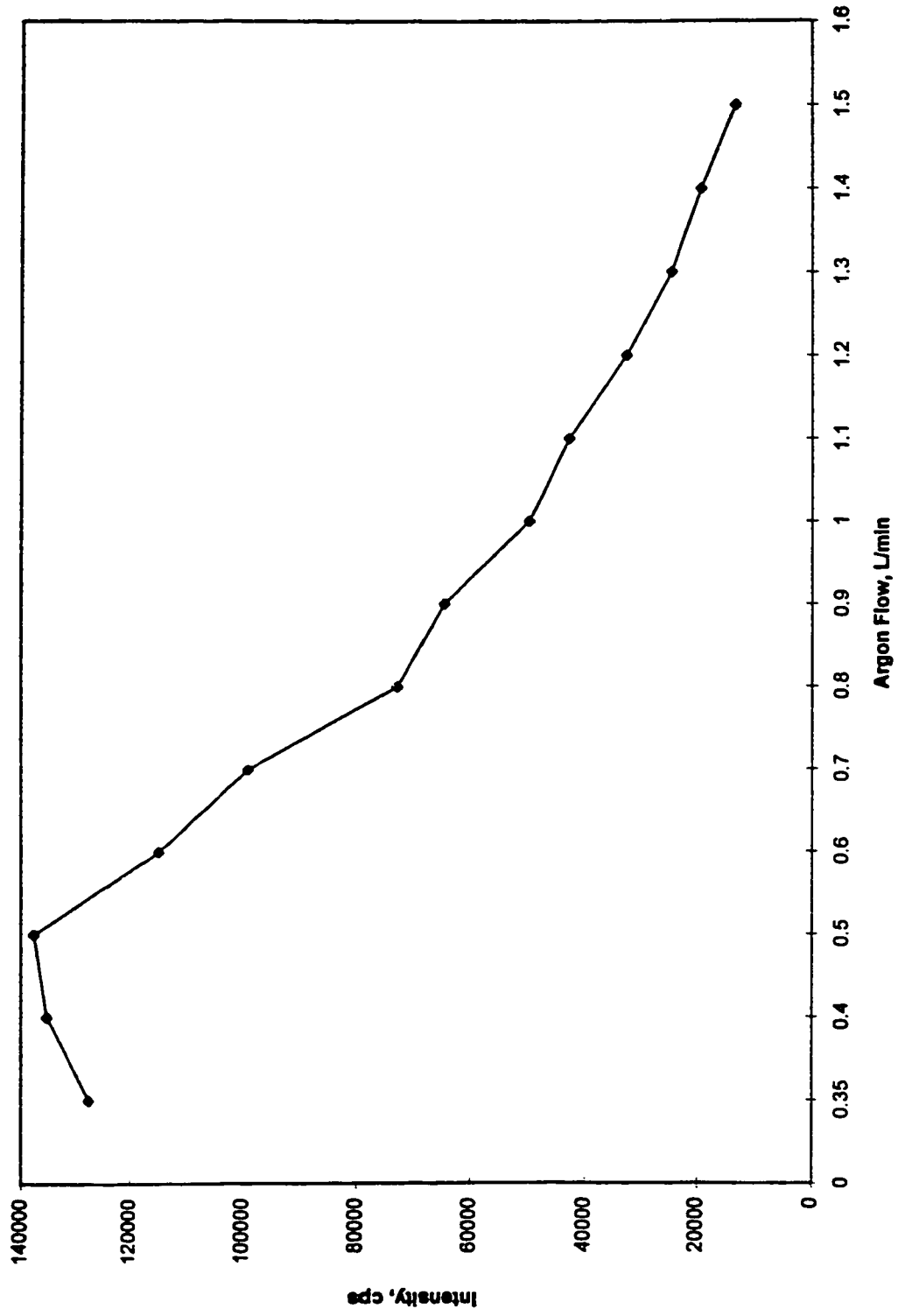

Figure 26. Optimizing argon flow rate for BAS SS stainless steel series, Cr 267.716

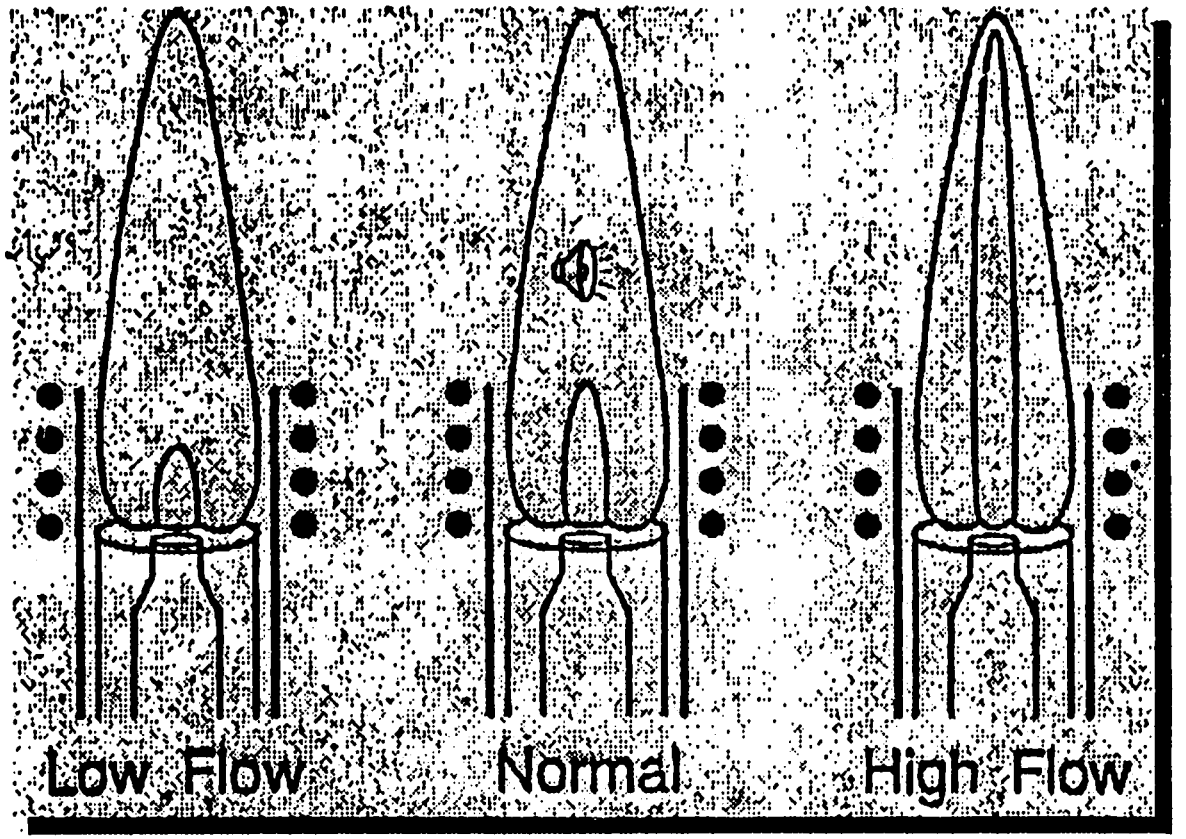

Figure 27. Effect of nebulizer flow on residence time.

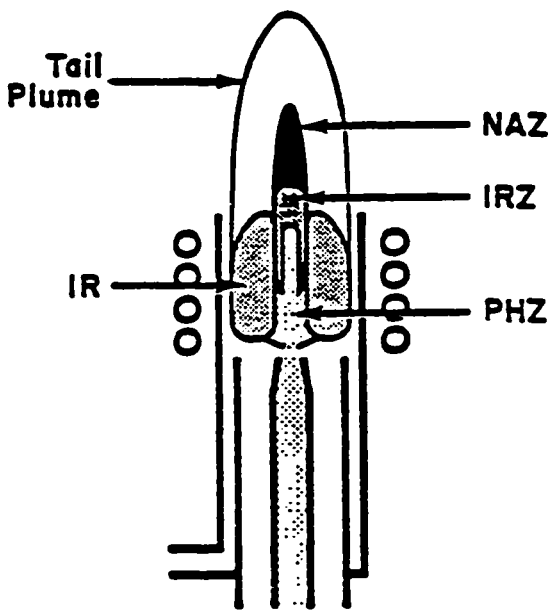

Figure 28. Zones of the ICP.

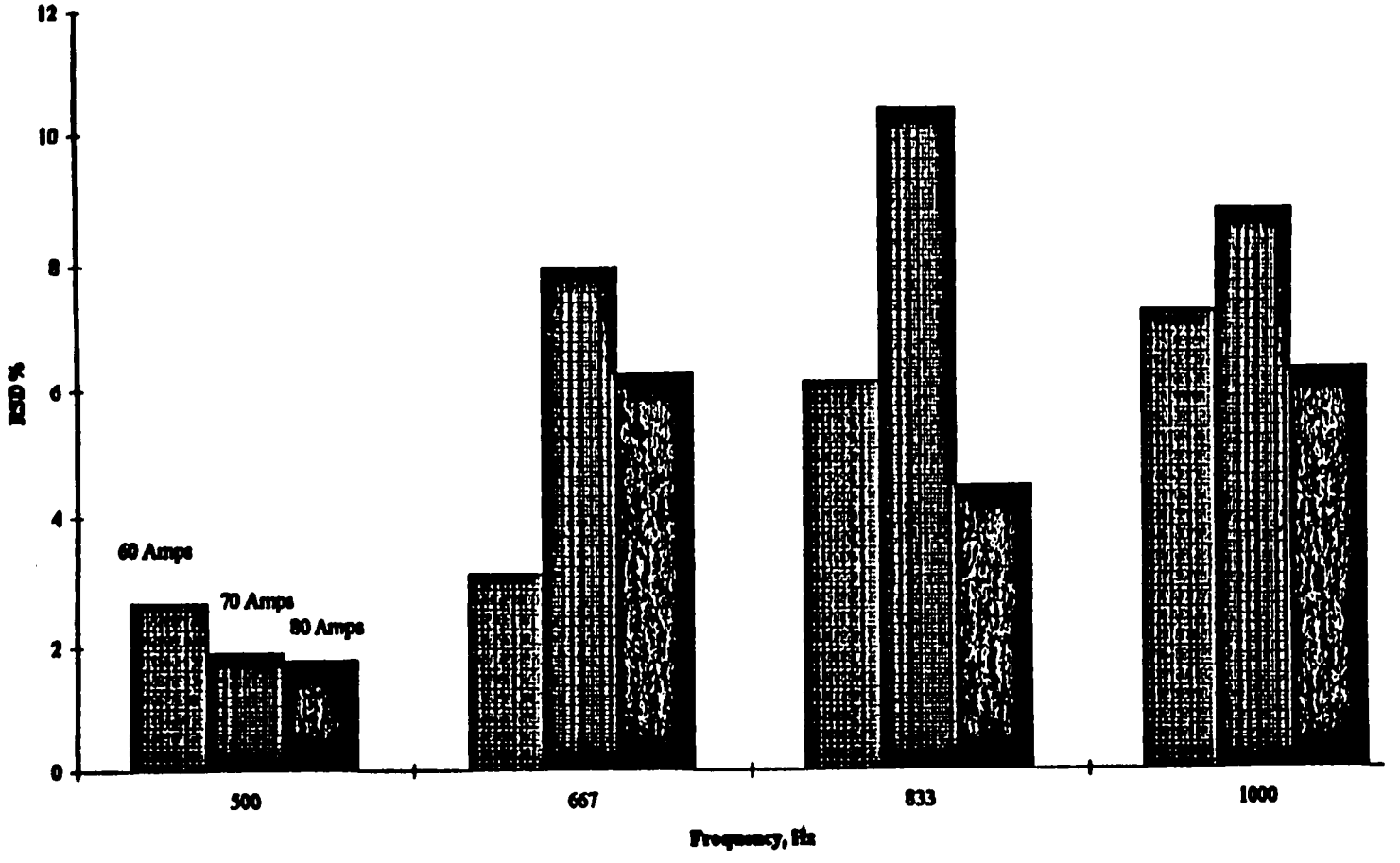

Figure 29. Dependence of spark parameters on analytical characteristics of the ablation process for BAS SS stainless steel series, Mn 260.569

continuously. There appears to be no obvious trend between % RSD values and peak current or frequency.

Figures 30 and **31** show the dependence of spark parameters on analytical characteristics of the ablation process for an NIST low alloy steel series and high alloy steel series, respectively, for Mn 260.569. The percent composition of Mn for the low alloy steel is 0.275 and is 1.63 for the high alloy steel. There are differences in the three matrices but optimized parameters for the three steel matrices appear at a repetition rate of 500 Hz and a current of 70-80 amps.

Another parameter that effects the analytical characteristics of the ablation process is the spark gap between the sample electrode and anode. **Figure 32** shows the analytical characteristics of the spark gap for the NIST low alloy steel series. The elemental composition for Mn 260.569 and V 310.230 is 0.275% and 0.041%, respectively. The % RSD values are for 20 readings on the ICP where the spark source is on continuously while the ICP analyzes the 20 replicates taken. **Figure 33** shows the length of the spark gap *vs.* signal intensity for the two elements. A spark gap of 2.0 mm was most stable and also had the highest signal intensity. For these reasons a spark gap of 2.0 mm was considered optimal. **Table 15** shows the optimal operating conditions for the ICP and "zero-bias" spark source for the steel samples.

Manual integration mode was used to insure that the sampling was executed at the same time for each analysis and also to optimize the read time of the detector for each element. Major constituents must have a short integration time so that the signal does not saturate. Minor constituents have a longer integration time for the detector to read more photons in order to increase signal/noise ratio.

Studies were carried out to show the importance of a seal between the sample electrode and a sample holder. If a proper seal is not formed the spark becomes unstable and oxygen is entrained into the gap. Oxygen reactions can cause many problems, including spectral interferences from oxides formed, and result in irreproducibility.

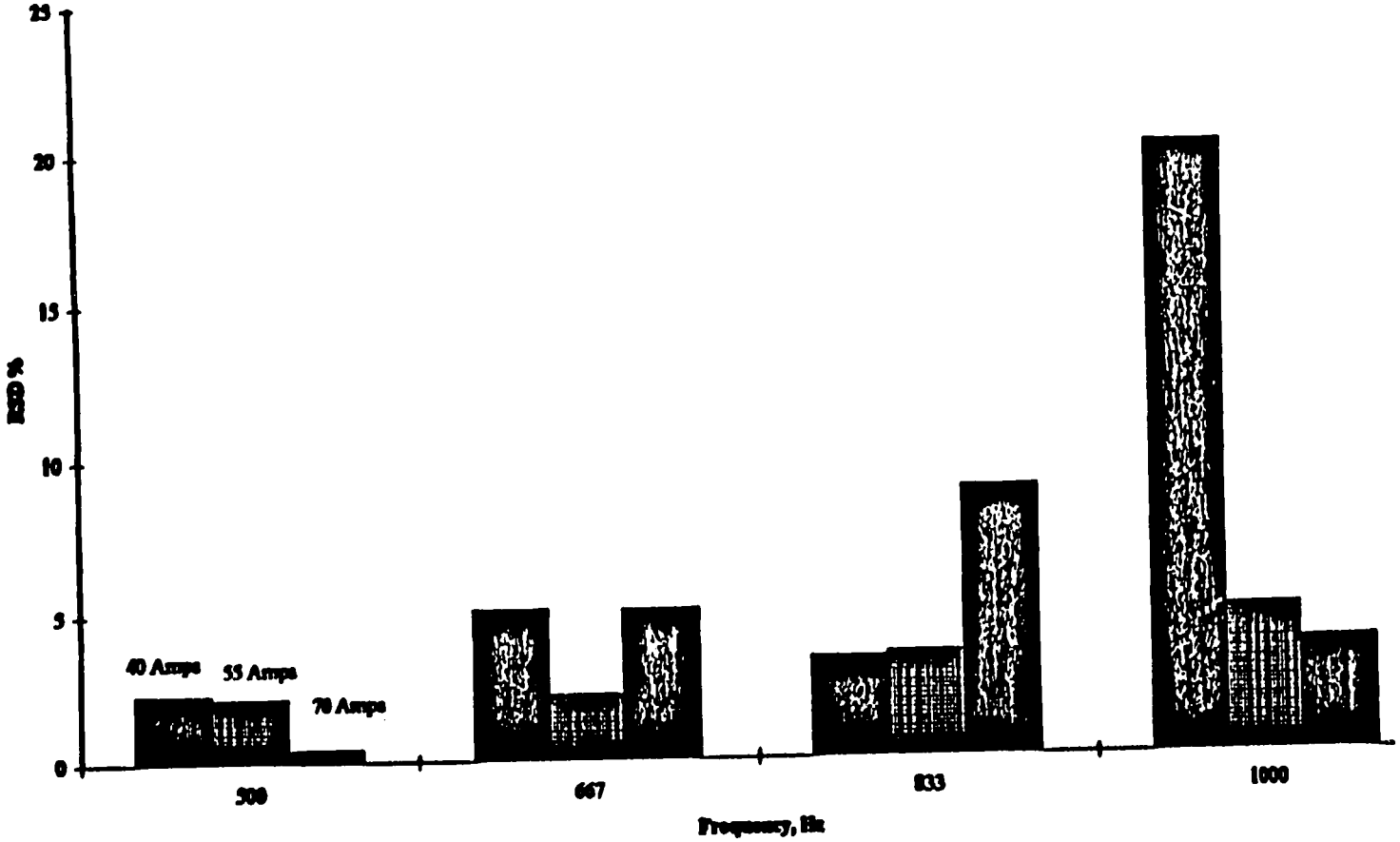

Figure 30. Dependence of spark parameters on analytical characteristics of the ablation process for NIST low alloy steel series, Mn 260.569.

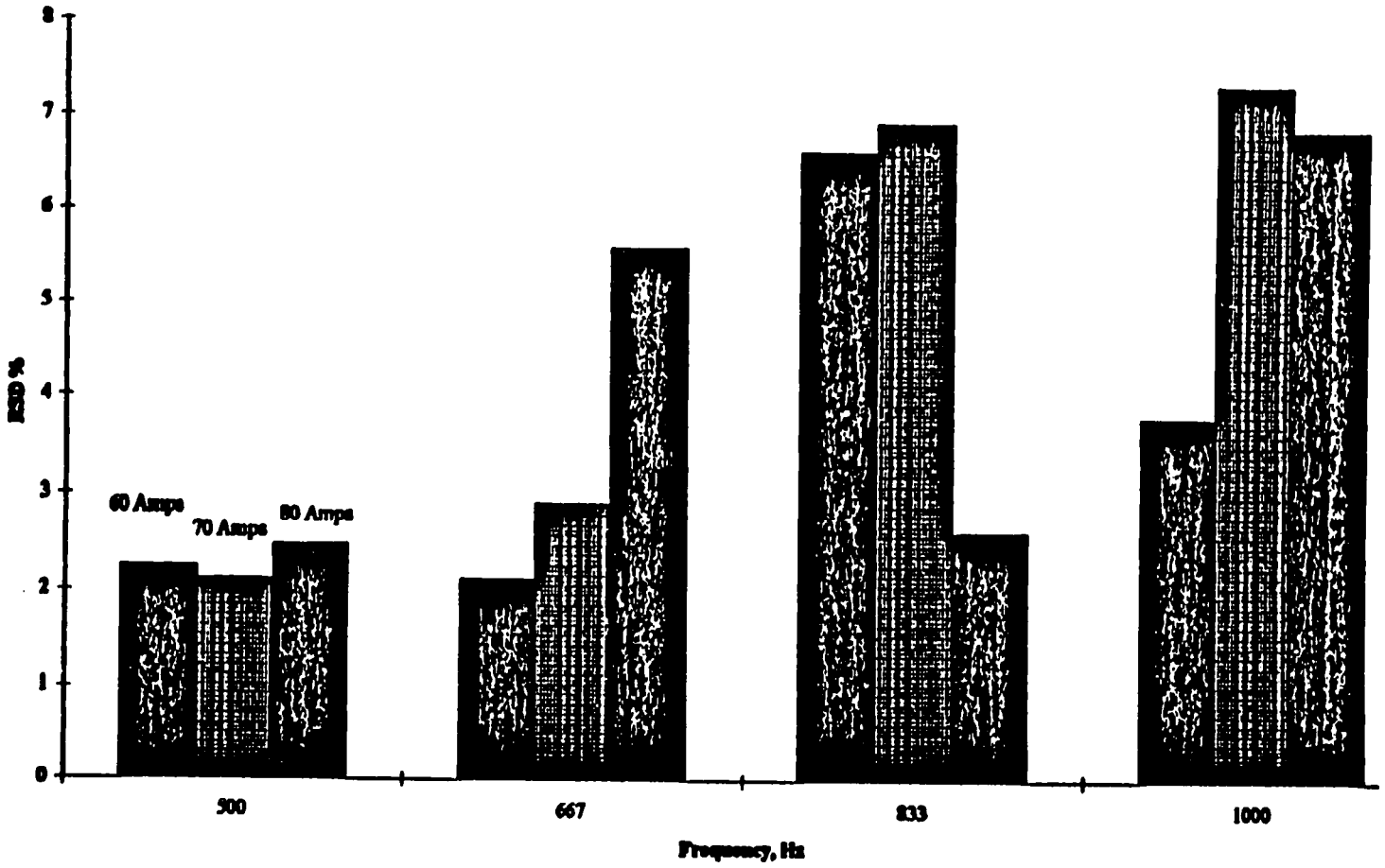

Figure 31. Dependence of spark parameters on analytical characteristics of the ablation process for NIST high alloy steel series, Mn 260.569.

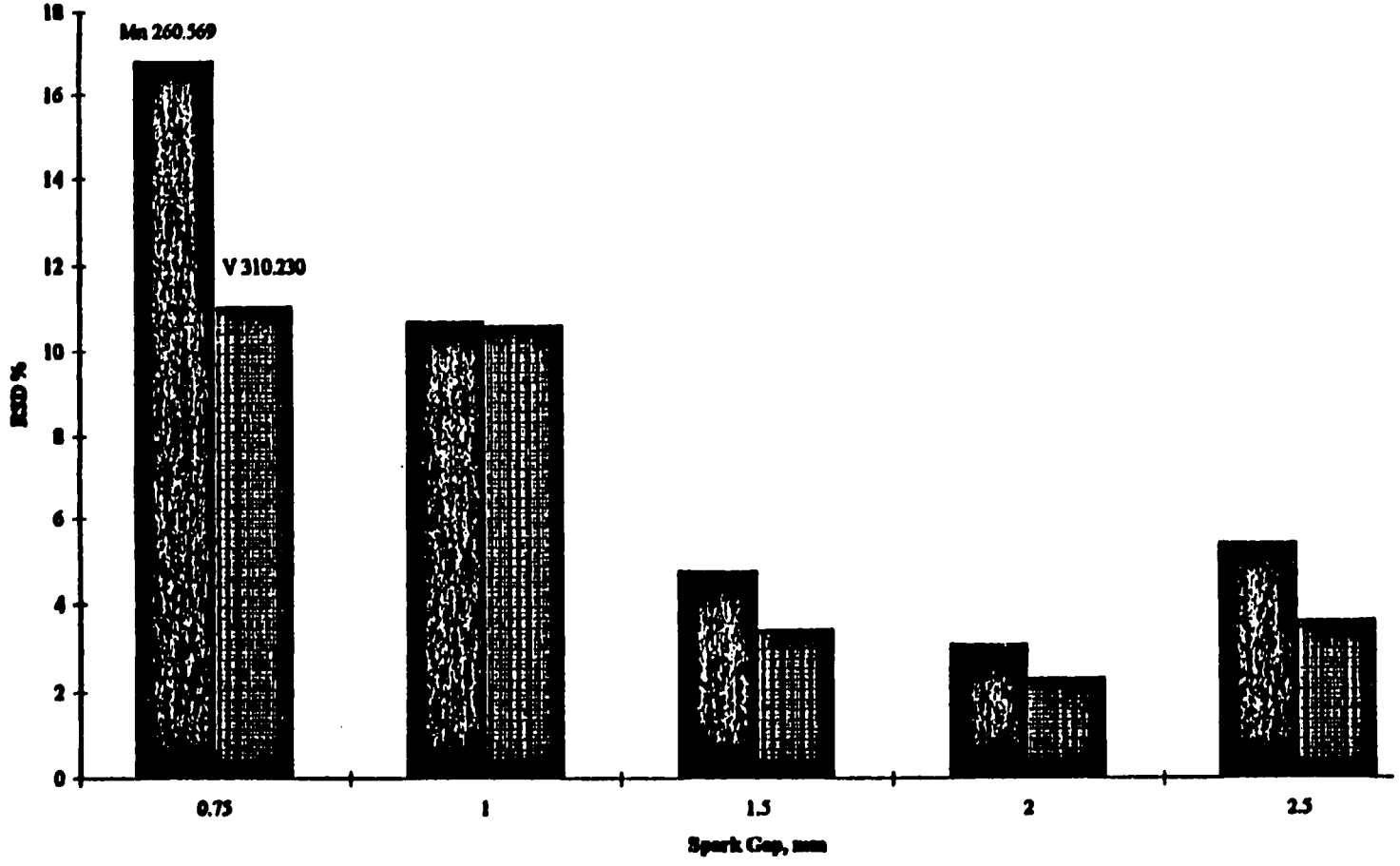

Figure 32. Dependence of spark gap on analytical characteristics of the ablation process for NIST low alloy steel series, Mn 260.569 and V310.230.

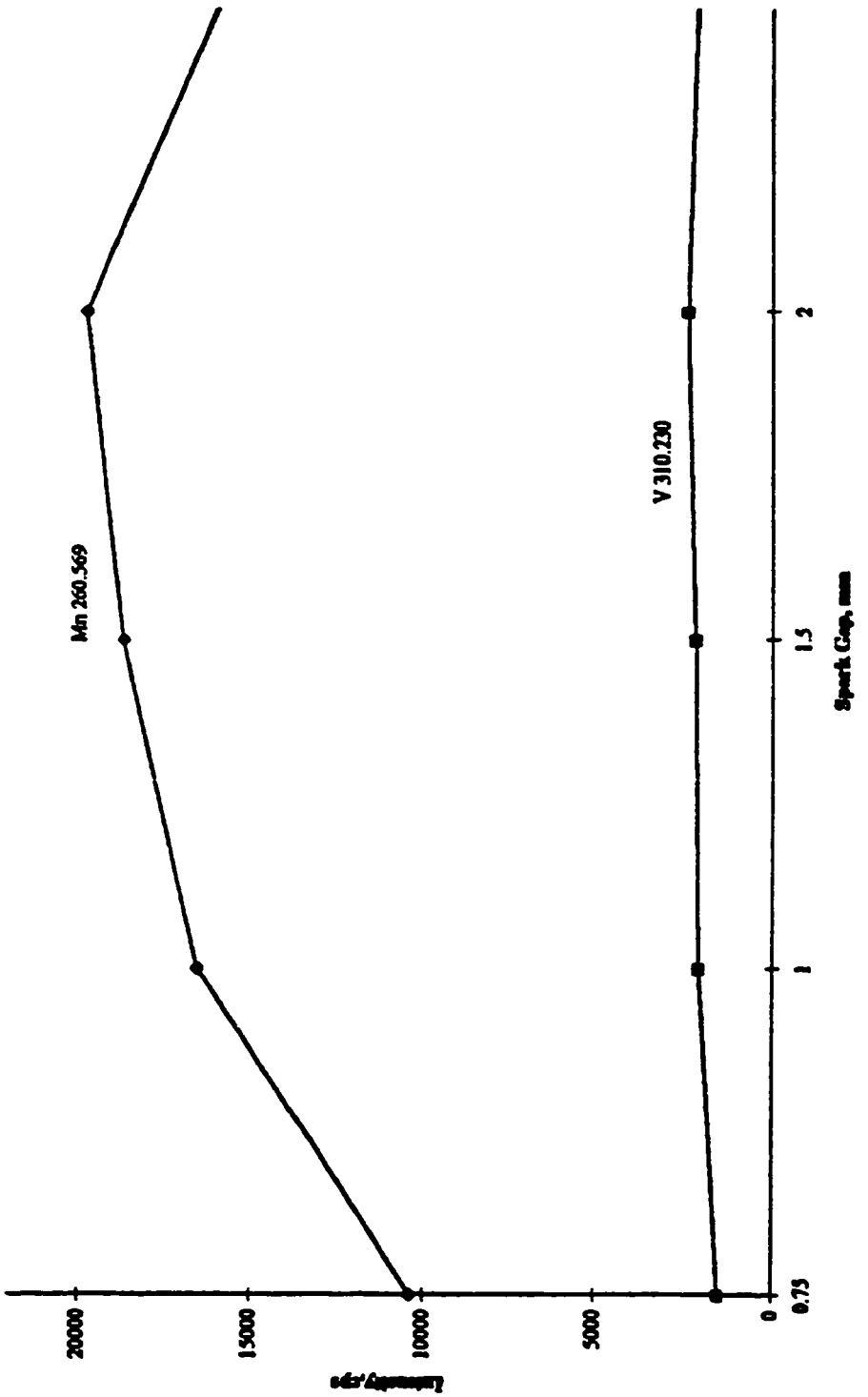

Figure 33. Length of the spark gap *vs.* signal intensity, Mn 260.569 and V 310.230.

Table 15. Optimal Conditions of the ICP-AES and "Zero-Bias" Spark Source for Steel Samples.

ICP-AES	
RF Power	1200 Watts
Argon Flow	
Nebulizer Flow	
Auxiliary Flow	1.0 L/min
Plasma Flow	15 L/min
Viewing Height	15 mm
Manual Integration Time	
Sampling Time	500-10,000 ms
Integration Time	50-2000 ms
Auto Background Correction	
Spark Source	
Repetition Rate	500 Hz
Peak Current	80 Amps
Spark Duration	5 μs
Pseudo-Triangular Waveform	
Spark Bias Current	≈ 0 Amps
Argon Flow	0.5 L/min
Preburn	30 Seconds
Spark Electrode Gap	2.00 mm

Figure 34 shows differences in the analytical characteristics of the ablation process for a sample (NIST SRM 1167) properly and improperly sealed while observing Fe 234.349. **Figure 35** shows the spectrum for Fe when a proper seal is formed and not formed. The difference of intensity levels from a sample with a proper seal and without a proper seal formed is easily seen. The % RSD values are calculated from 20 readings on the ICP where the spark source is on continuously during the 20 readings.

Method performance was evaluated by creating a calibration curve with NIST SRMs 1161, 1162, 1164, 1165, 1166, 1167, and 1168. NIST SRM 1163 was analyzed as a sample. **Table 16** shows these results. Generally, a recovery within 10% is achieved.

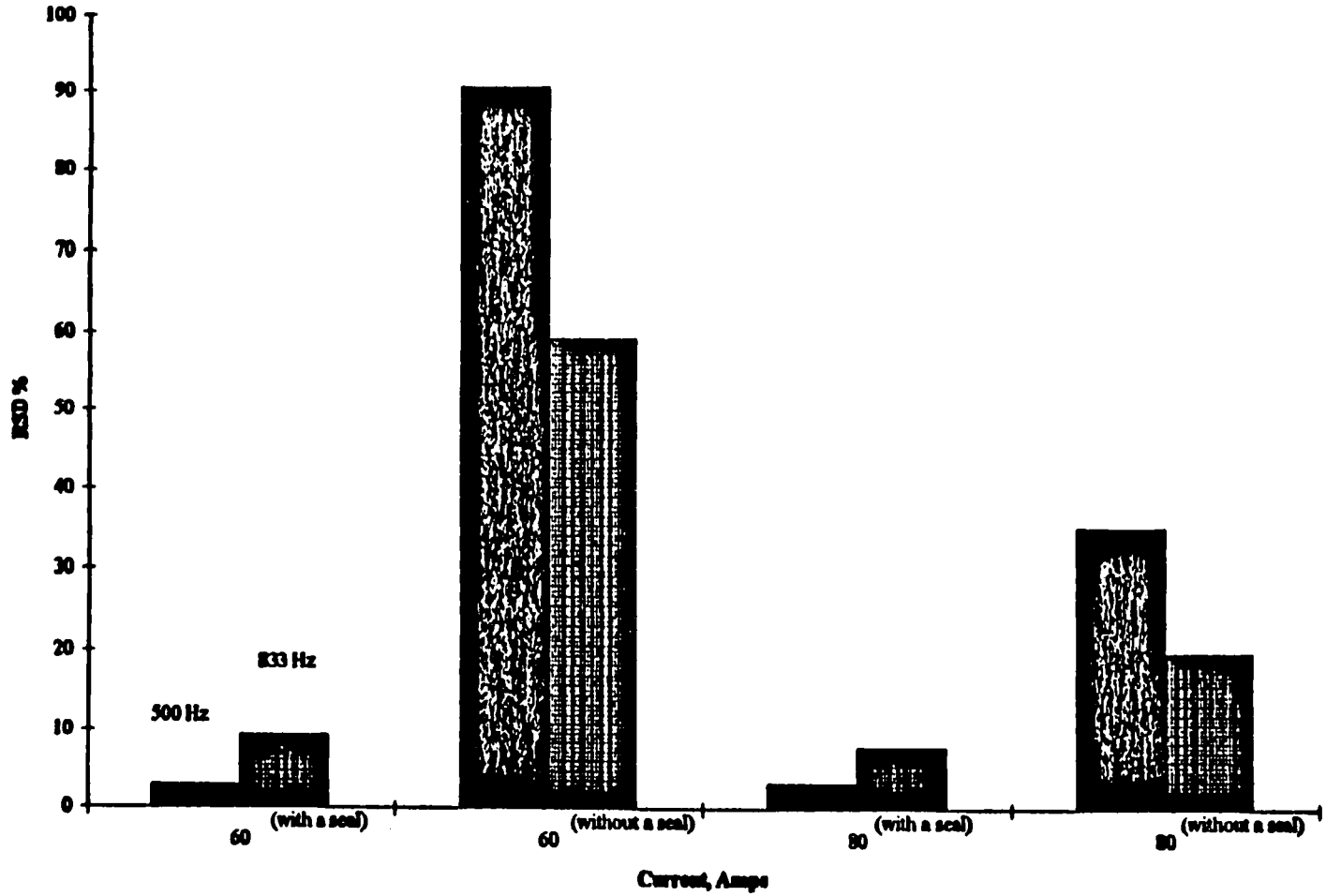

Figure 34. Analytical characteristics of the ablation process for NIST SRM 1167, Fe 234.349 when a proper seal is both formed and not formed between the sample electrode and sample holder.

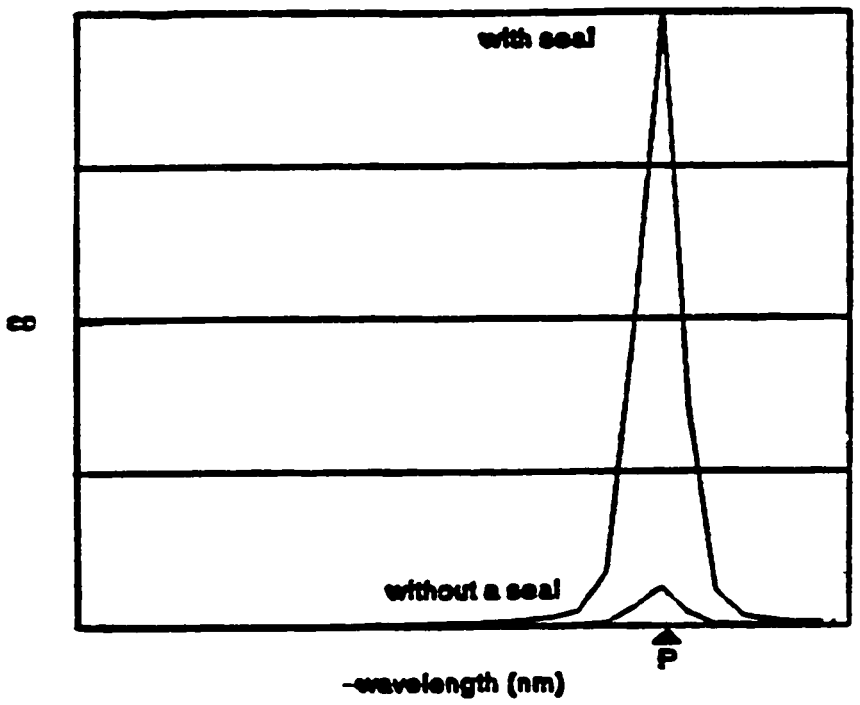

Figure 35. Difference of signal intensity of Fe 234.349 when a proper seal is formed between the sample electrode and sample holder.

Table 16. Method Performance of NIST Low Alloy Steel Series.

Element	Wavelength	Measured Value (μg/g)	Certified Value (μg/g)	% Recovery
C	193.018	236	220	107.3
Si	288.158	4054	4100	98.9
Cu	324.754	4791	4700	101.9
Ni	231.604	3756	3900	96.3
Cr	205.552	2615	2600	100.6
Mo	281.615	1131	1200	94.2
Sn	189.933	140	130	101.1
Ti	334.941	119	100	119.0
W	207.911	930	1050	88.6
Zr	343.823	1978	2000	98.9
Nb	269.706	2105	1950	107.9
Ta	226.230	1666	1500	111.1
Al	309.271	276	270	102.2

Chapter 5

The Analysis of Brass Samples

Introduction

The progress of technology puts increased emphasis on the quality of materials. Chemical compositions are required to meet strict tolerances for alloying metals as well as for traces of impurities in the field of metals and alloys. The day-to-day requirements of industry demand accurate determinations of the elemental composition of a sample. The analytical laboratory must be able to provide accurate and rapid results. This can only be carried out by using appropriate methods rationally established. The conventional spark source has been an established method for a number of years whereas the development of the "zero-bias" spark source is new research. Accurate and precise results of the new spark source have been demonstrated in a previous chapter. It has been discussed earlier the significant reduction in time involved for solid sample introduction to the ICP-AES compared to the normal nebulization of liquids.

Results and Discussion

The parameters for brass standards were optimized in a fashion which is similar to the method described previously. **Figures 36** and **37** show the effect of argon flow rate on signal intensity for the Be 234.911 and Co 238.943 lines in the NIST SRM 1121 brass standard. The maximum intensities for Be and Co were 0.50 L/min and 0.40 L/min, respectively. However, the signal at 0.40 L/min is only slightly lower than at 0.50 L/min for Be. Therefore, a flow rate of 0.40 L/min was considered optimal. **Figures 38** and **39** show RF power *vs.* signal intensity for Be and Co in brass standards. An RF power of 1250 Watts was chosen for the same reasons discussed earlier. **Figure 40** shows the dependence of spark parameters on the analytical characteristics of the ablation process for NIST brass series for Be. A repetition rate of 500 Hz and current peak waveform of 60 amps were chosen as optimal parameters. **Table 17** shows optimal conditions for the brass samples.

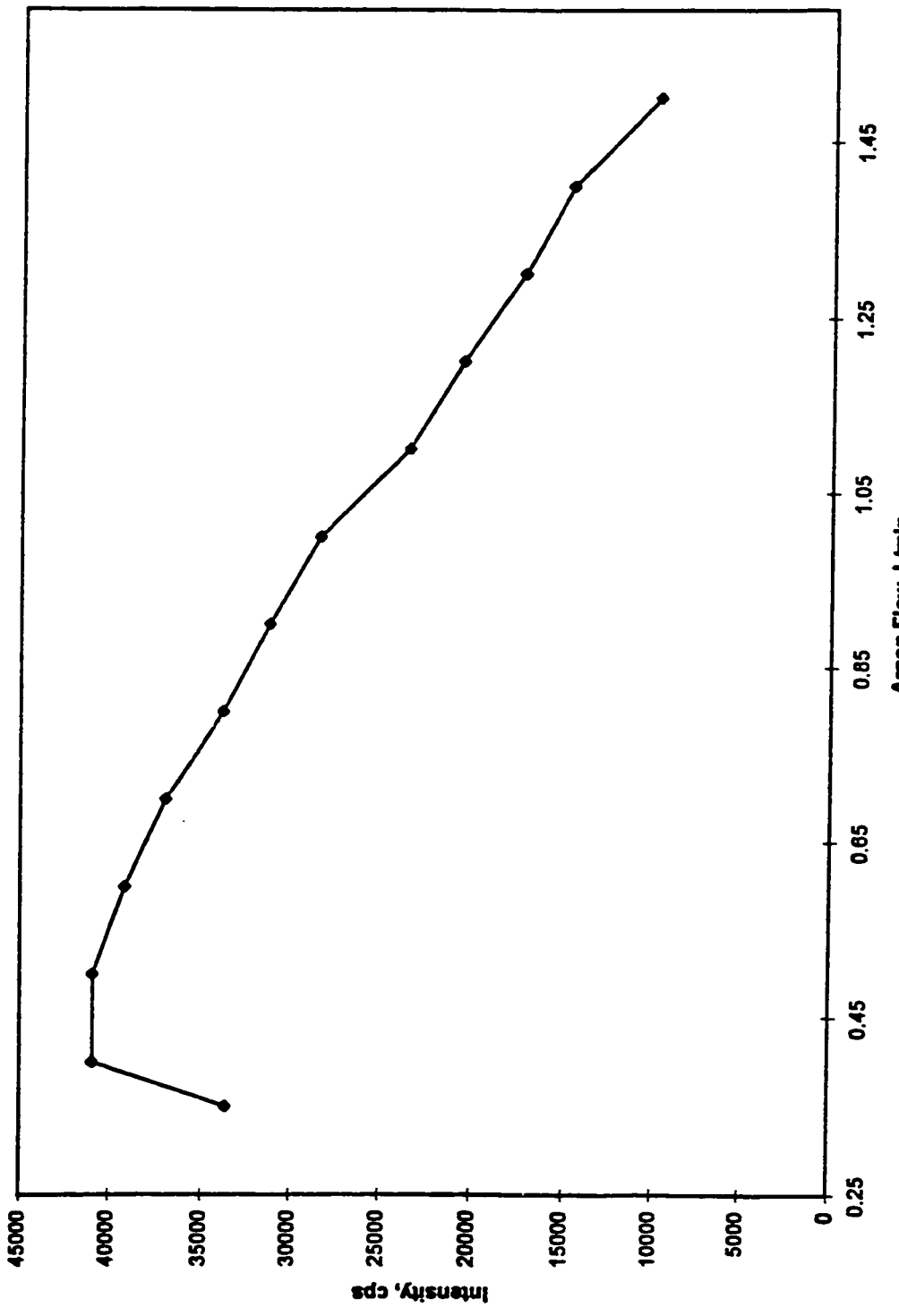

Figure 36. Optimizing argon flow rate for NIST brass standards, Be 234.911.

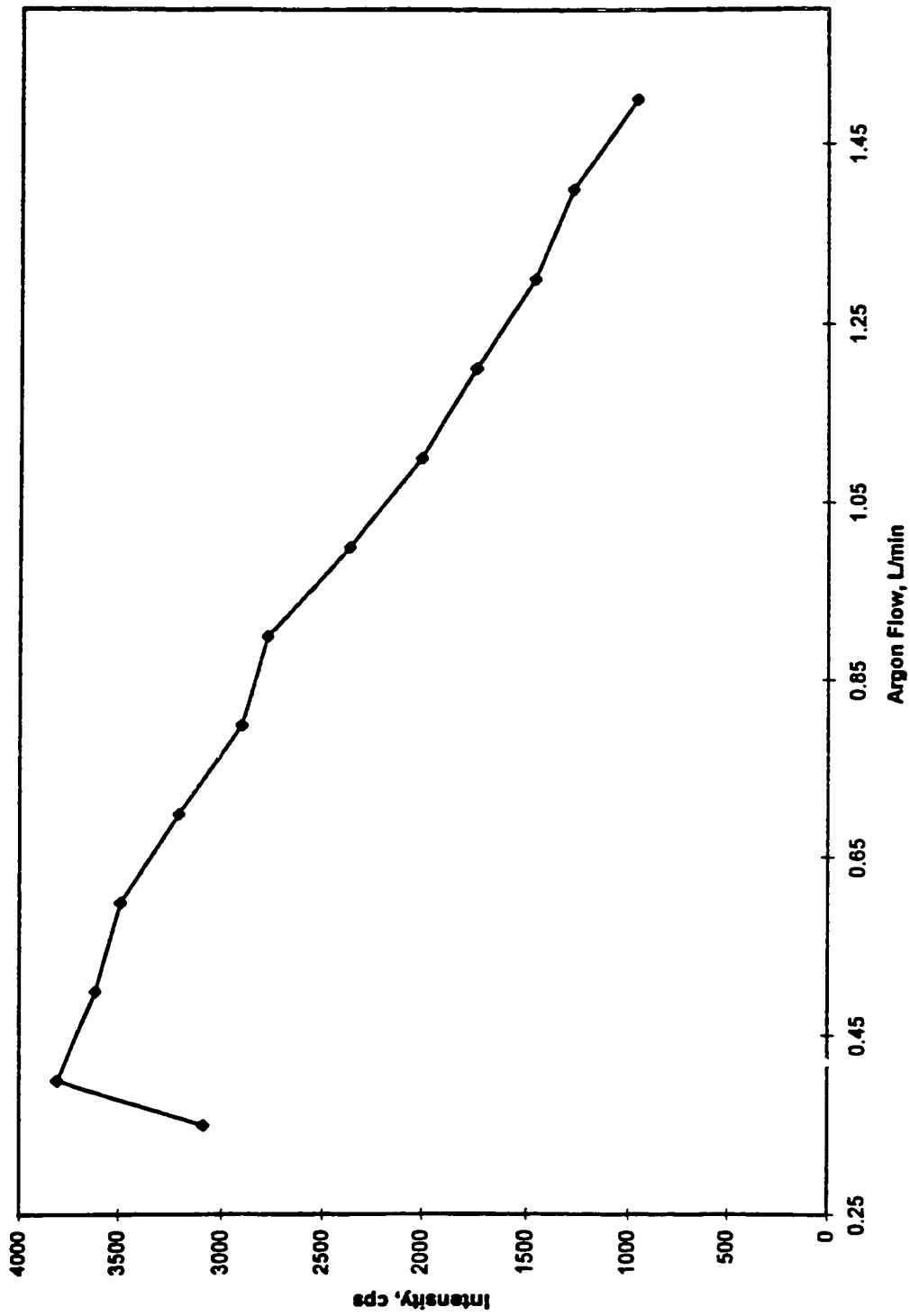

Figure 37. Optimizing argon flow rate for NIST brass standards, Co 238.943.

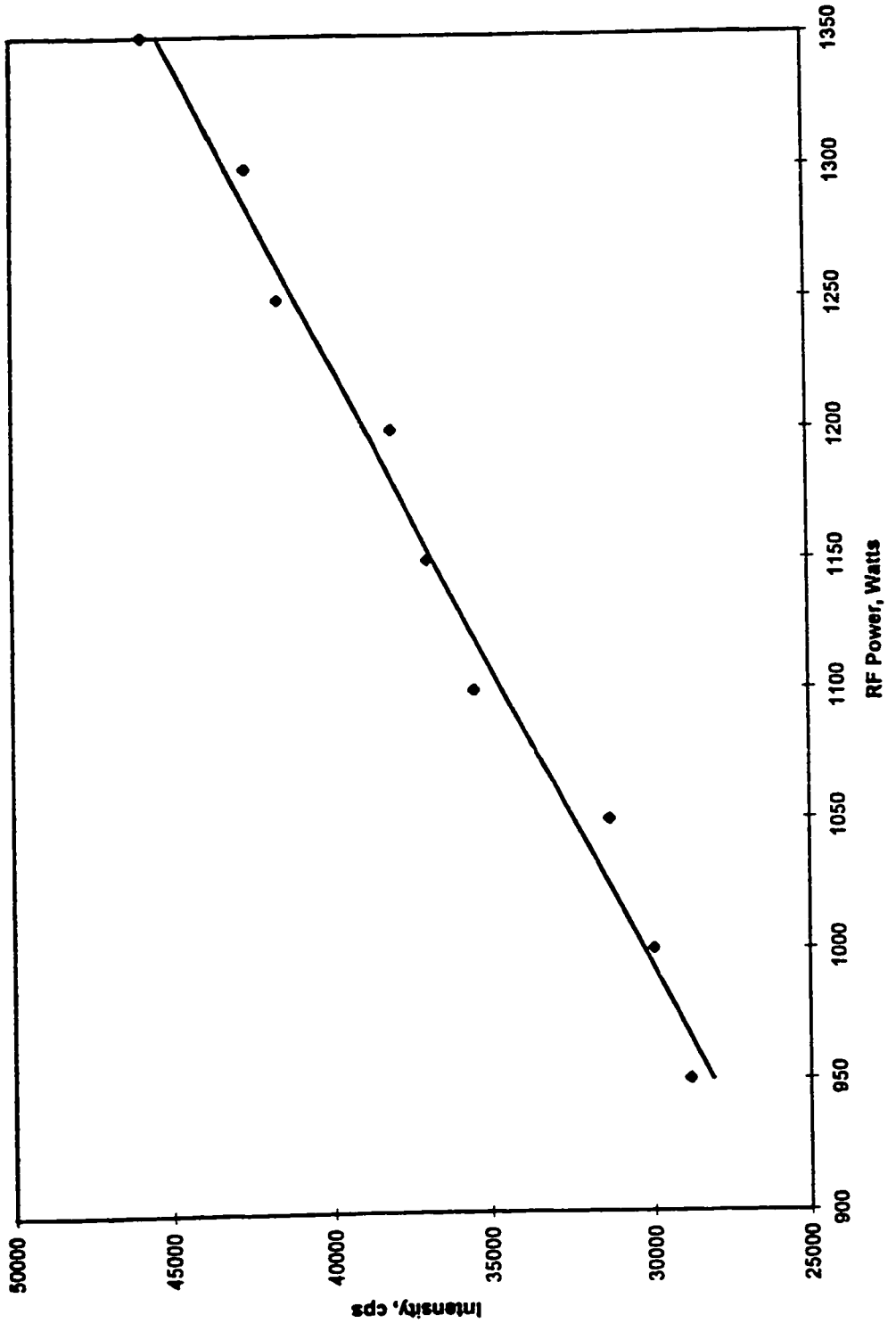

Figure 38. Optimizing RF power for NIST brass standards, Be 234.911.

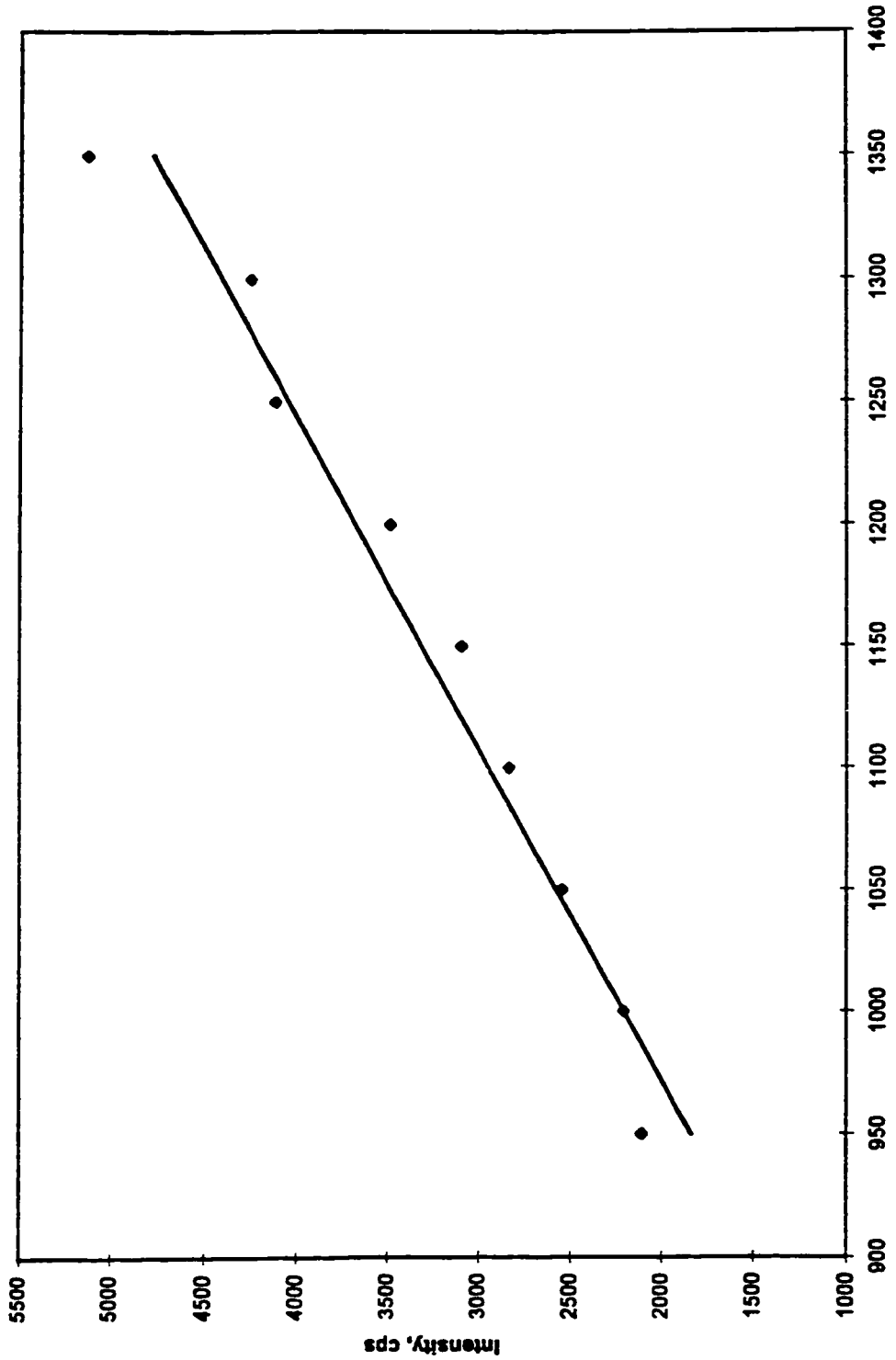

Figure 39. Optimizing RF power for NIST brass standards, Co 238.943.

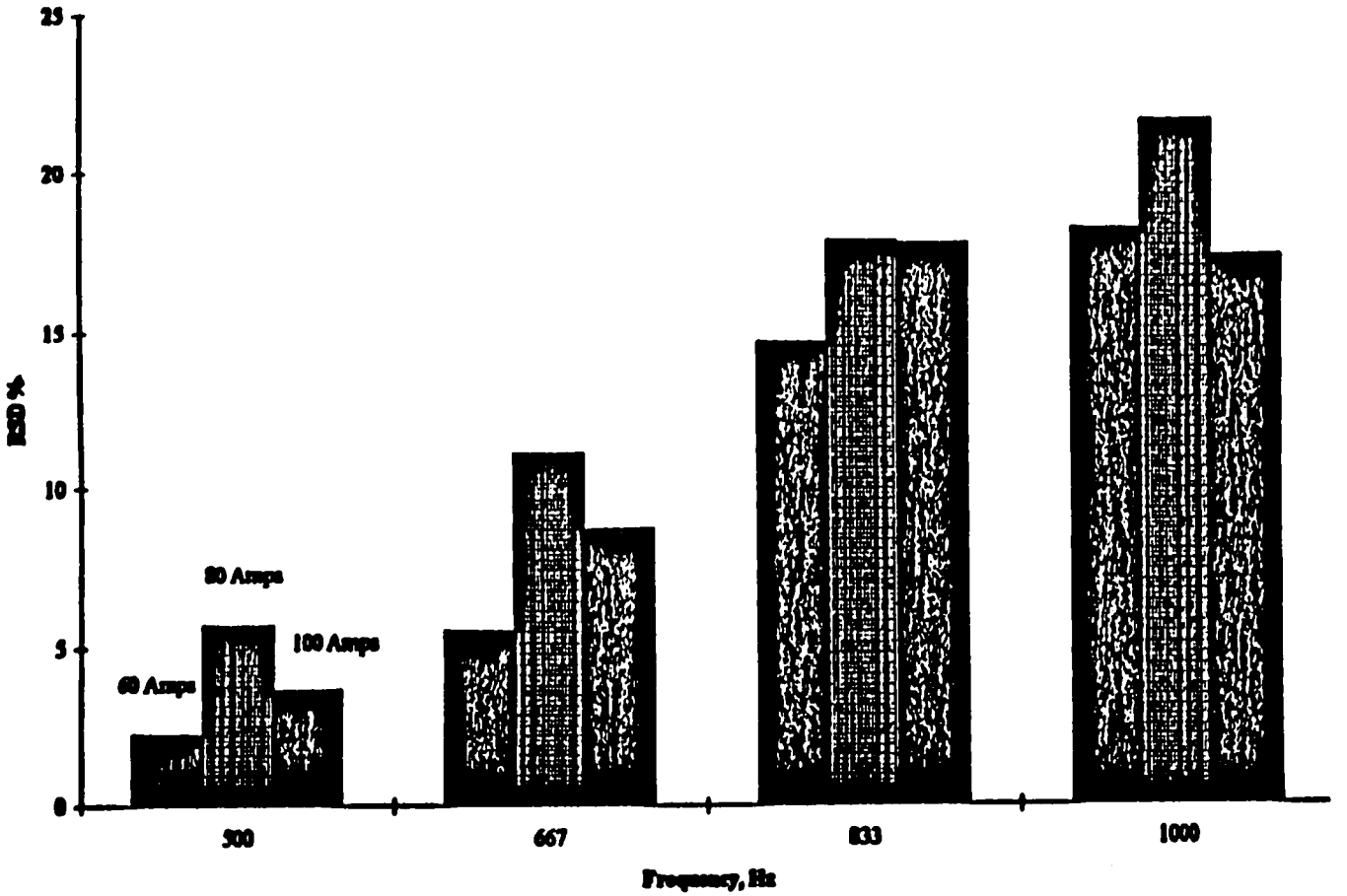

Figure 40. Dependence of spark parameters on analytical characteristics of the ablation process for NIST brass standards, Be 234.911.

Table 17. Optimal Conditions of the ICP-AES and "Zero-Bias" Spark Source for Brass Samples.

ICP-AES	
RF Power	1250 Watts
Argon Flow	
Nebulizer Flow	
Auxiliary Flow	1.0 L/min
Plasma Flow	15 L/min
Viewing Height	15 mm
Manual Integration Time	
Sampling Time	500-10,000 ms
Integration Time	50-2000 ms
Auto Background Correction	
Spark Source	
Repetition Rate	500 Hz
Peak Current	60 Amps
Spark Duration	5 μs
Pseudo-Triangular Waveform	
Spark Bias Current	≈ 0 Amps
Argon Flow	0.4 L/min
Preburn	30 Seconds
Spark Electrode Gap	2.00 mm

Aziz *et al.*[48] suggest that improvements in the power of detection can result from increasing the amount of material delivered to the plasma. An increase in the repetition rate of the spark source increases the amount of material removed from the sample electrode per unit time. But, as stated previously, excessive frequency settings often result in unstable discharges and overheating of the sample (and the spark source). Optimizing the integration time of the ICP-AES also helps improve detection limits. Integration time is defined as the time period over which the detectors will be collecting photons from the plasma during analysis. For intense emission lines or major constituents of a sample matrix, too many photons will saturate the detector. In such cases, a short integration time would be optimal. For weak emission lines or trace elements, longer integration times will be needed in order to provide acceptable

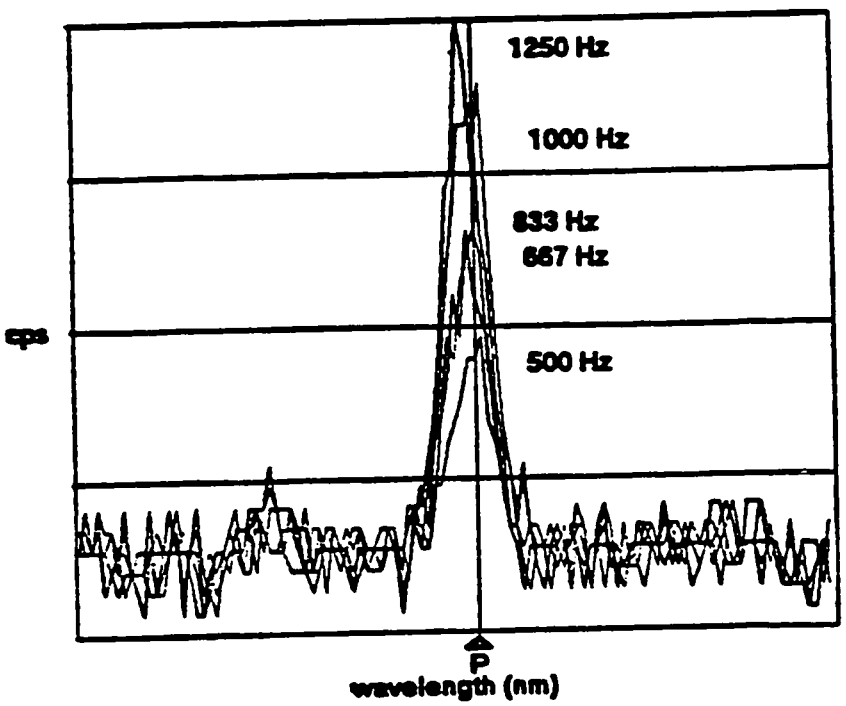

Figure 41. Spectra for Fe 238.204 for NIST SRM 1121 Beryllium-Cobalt Standards, varying repetition rate of the "zero-bias" spark source.

signal/noise ratios.[60] **Figure 41** shows the spectra of Fe 238.204 for NIST 1121 Beryllium-Copper Standards at spark repetition rates of 500, 667, 833, 1000, and 1250 Hz. Fe is present at a weight composition of 0.085%. The manual integration time is 0.05 s and the sampling time is 0.05 s. The sampling time is the total amount of time the detector reads information for the sample. It is equal to the integration time multiplied by the number of readings. Typically, the longer sampling times result in better detection limits and improved analyte precision. The spectrum is noisy for repetition rates of 500, 667, 833 and 1000 Hz. At 1250 Hz the spectrum has "smoothed" out. Since higher repetition rates result in unstable discharge and sample overheating, the effect of manual integration time was studied. **Figure 42(b)** shows the improvement of signal/noise ratio with a longer integration time, 1.0 s when compared to **Figure 42(a)** with an integration time of 0.05 s. A repetition rate of 500 Hz and current of 60 amps was ultimately selected.

Higher peak currents of the spark source waveform increase the ablation rate of the sample electrode. The current magnitude was adjusted by changing the capacitor charging voltage on the "zero-bias" spark source. As the charging voltage increases, the peak current increases. The peak current was measured oscilloscopically using a conventional Rogowski coil. Aziz *et al.*[48] state that increases in the voltage of the spark increase ablation rates. Ekimoff *et al.*[62] also found that increasing the voltage increases emission intensity. One would expect emission intensity to increase linearly. **Figure 43** shows that the signal does not increase linearly as a function of the spark current peak waveform. **Figure 44** shows that the current peak waveform vs. signal intensity is linear to approximately 70 amps with a correlation coefficient of 0.9978. At higher currents it is linear with a correlation coefficient of 0.9880 at a smaller slope. Aziz *et al.*[48] demonstrated that an increase in the voltage of the spark increases the ablation rate but results in increased particle size. Larger particles often do not reach the plasma; instead they settle in the spray chamber.

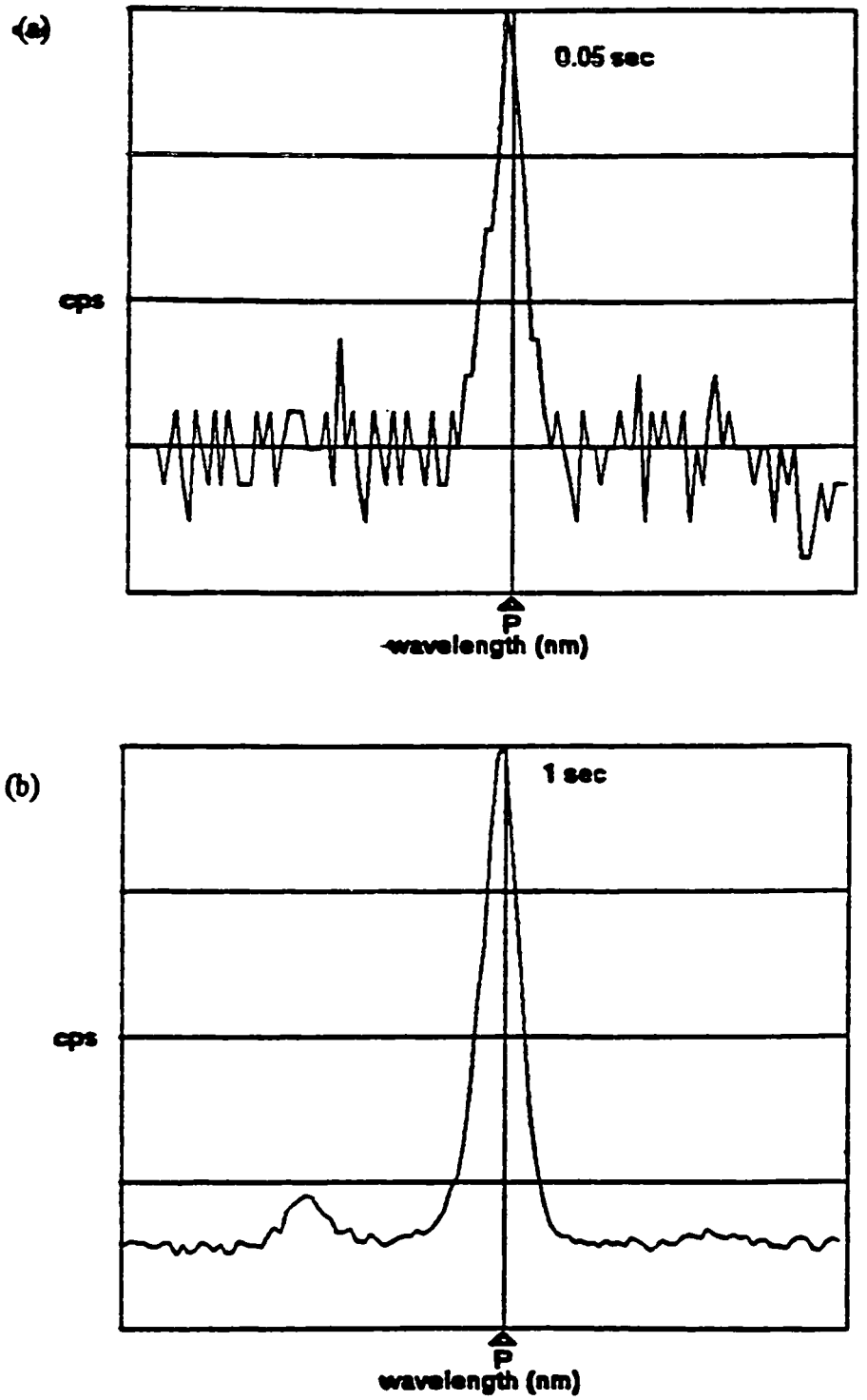

Figure 42. Spectra for Fe 238.204 at manual integration times of (a) 0.05 seconds and (b) 1.0 second.

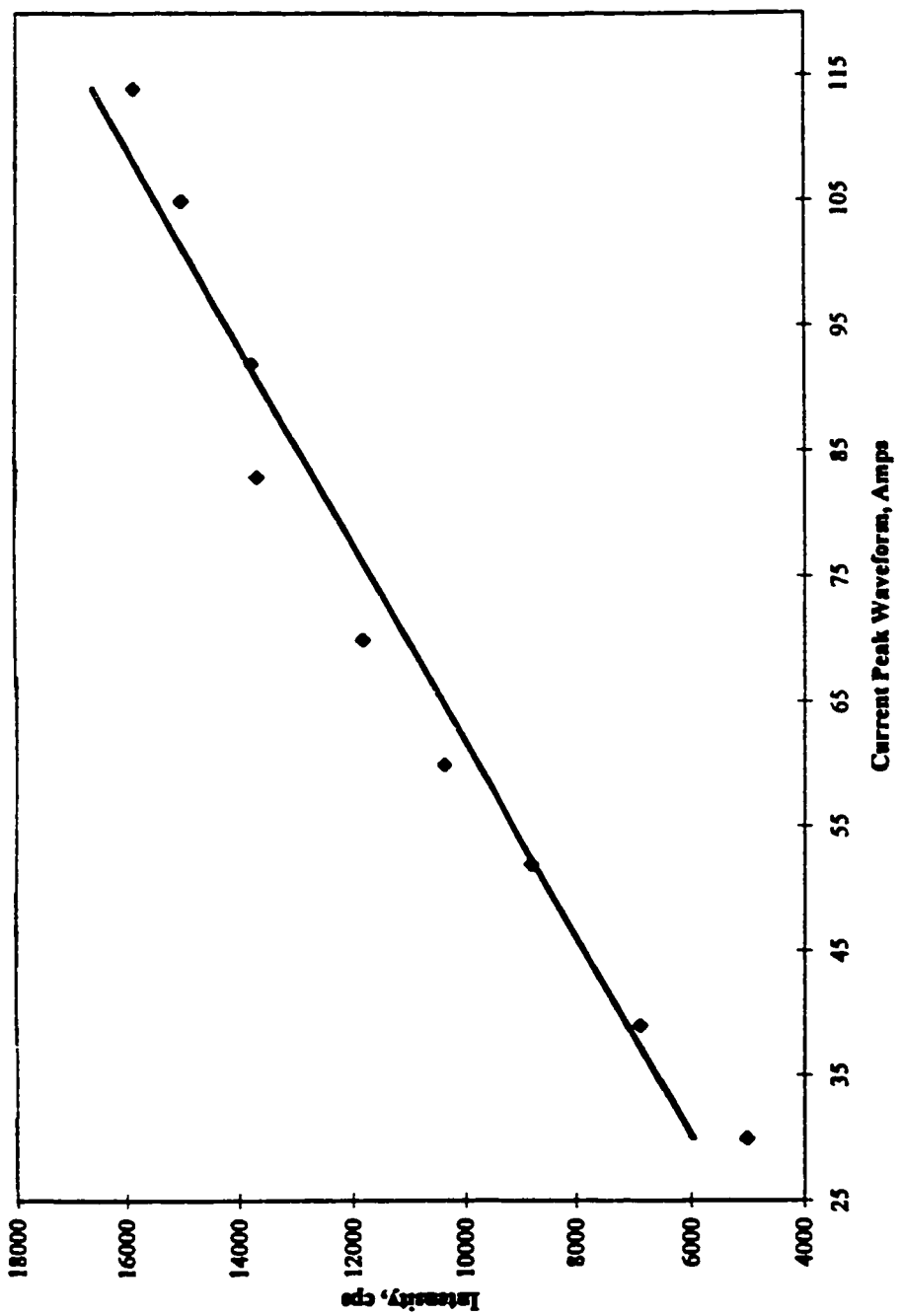

Figure 43. Current peak waveform of the spark source *vs.* signal intensity.

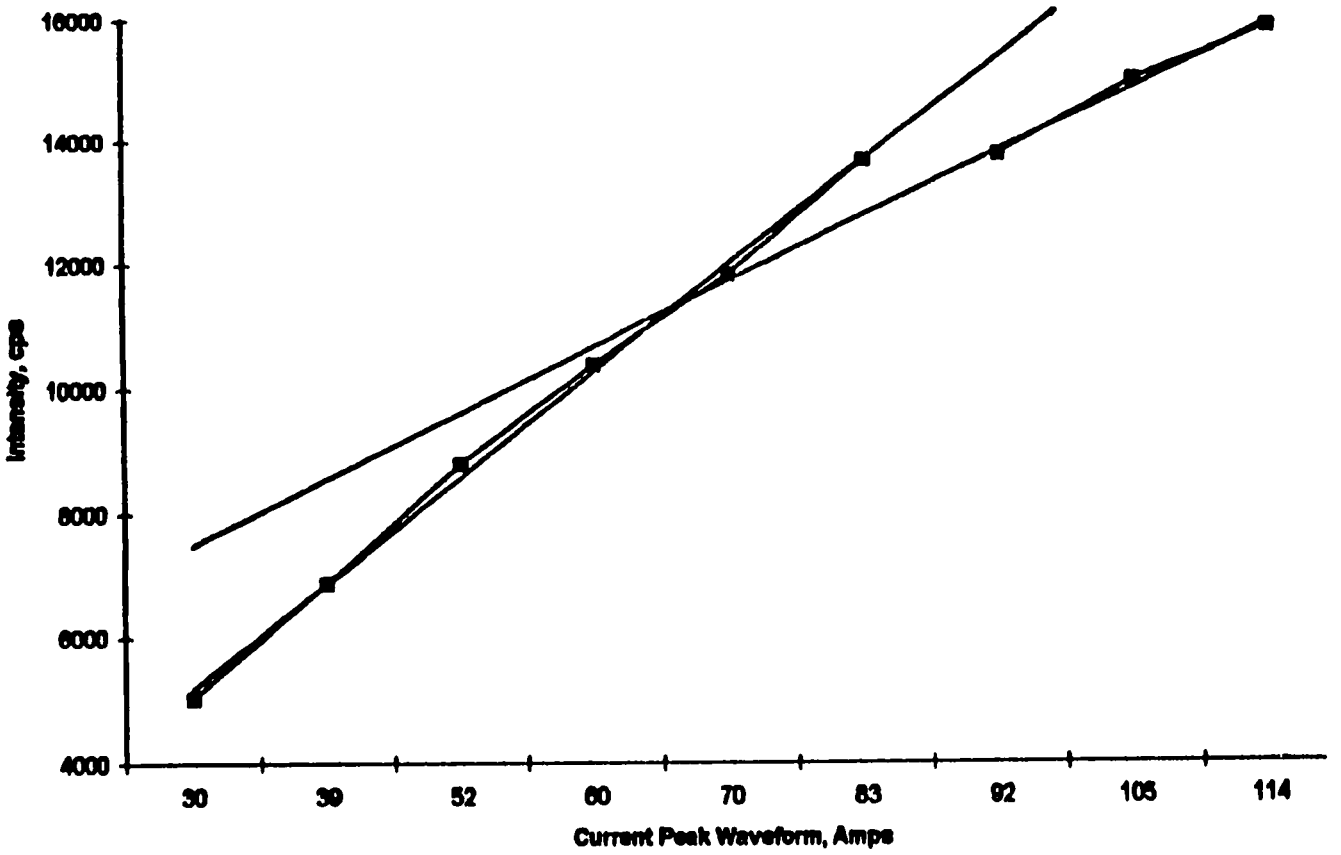

Figure 44. Current peak waveform of the spark source *vs.* signal intensity for Zn 206.200.

Aziz *et al.*[48] also show that increasing the repetition rate of a medium voltage spark source increases the amount of material removed from the sample. Therefore, when plotting repetition rate of the spark source *vs.* signal, the intensity should be linear. **Figure 45** shows that linearity is not achieved. A linear response is seen up to a repetition rate of approximately 900 Hz; then the signal intensity tends to level off. The data points represent an average of three analyses, each analysis is a different burn at a different location on the sample electrode. The error bars represent the standard deviations of the three analyses. One possibility of not achieving linearity could be that at higher repetition rates larger particles are ablated which settle in the spray chamber. We have no data to support such a conclusion, however.

A preliminary experiment was carried out to determine whether larger particles are ablated when using higher repetition rates. For this experiment, an on-line collection of ablated particles was obtained with an air sampling cassette to accumulate ablated particles for relative size determination. Smaller particles were presumed to be able to pass through a filter with a particle retention of 1 μm, which was placed in the air sampling cassette. Ideally, more particles should be collected at higher repetition rates if larger particles are generated.

An air sampling cassette (Gelman, Ann Arbor, MI) was placed between the "zero-bias" spark source and ICP-AES to collect the ablated particles. The cross section of the air sampling cassette is shown in **Figure 46**. The upper section was connected to the spark source with tygon tubing and the lower section was connected to the ICP with tygon tubing. A glass microfiber filter (Gelman, Ann Arbor, MI) with a particle retention of 1 μm was placed in the center section of the cassette allowing particles smaller than 1 μm to pass through the filter to the plasma. If larger particles were ablated at higher repetition rates, they should remain in the air sampling cassette not being able to pass through the filter to the ICP. Therefore, the signal intensity of ablated particles passing through the filter should decrease with increasing repetition rates. **Figure 47** shows a

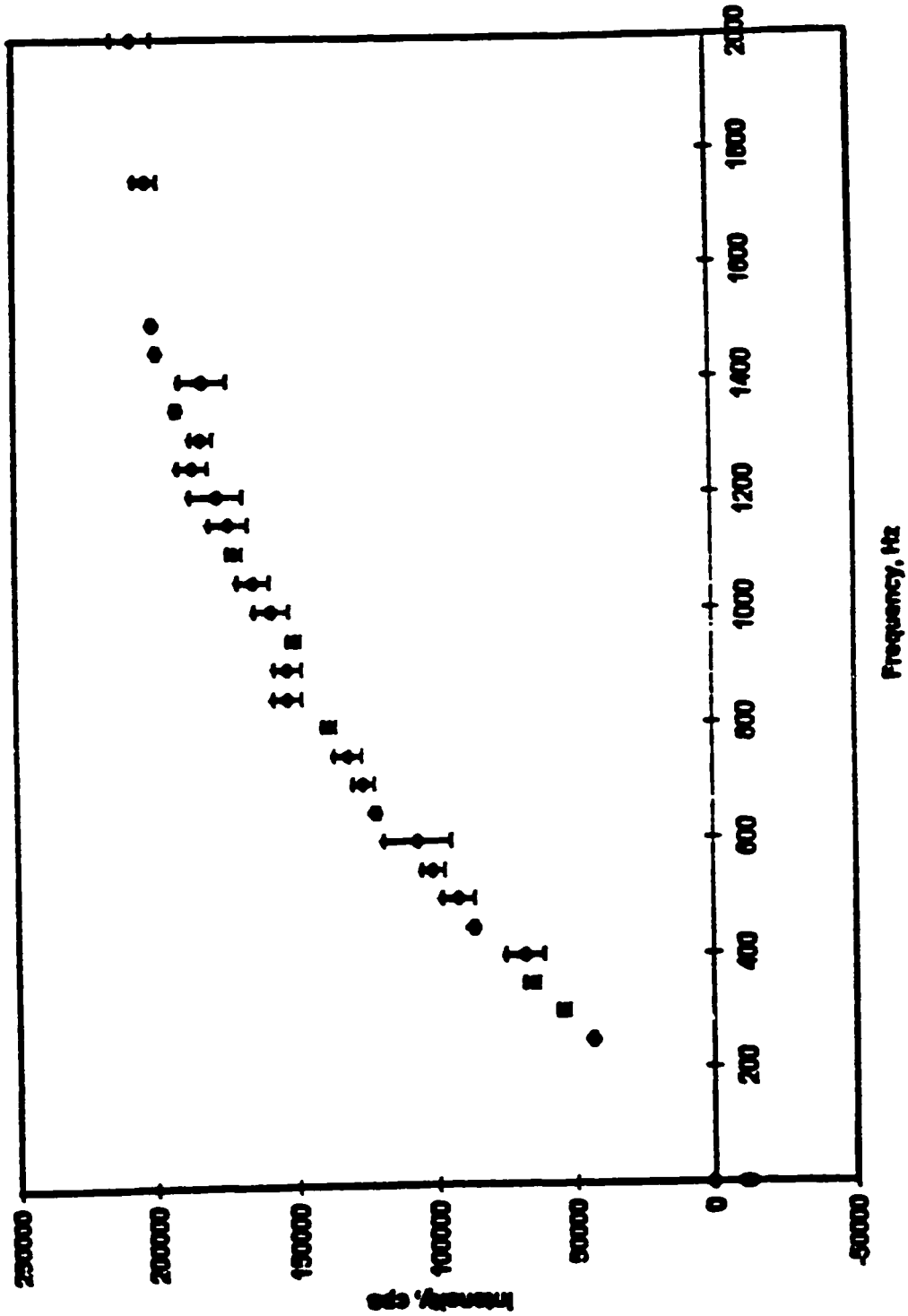

Figure 45. Frequency of the spark source *vs.* signal intensity for NIST SRM 1106, Cu 213.598.

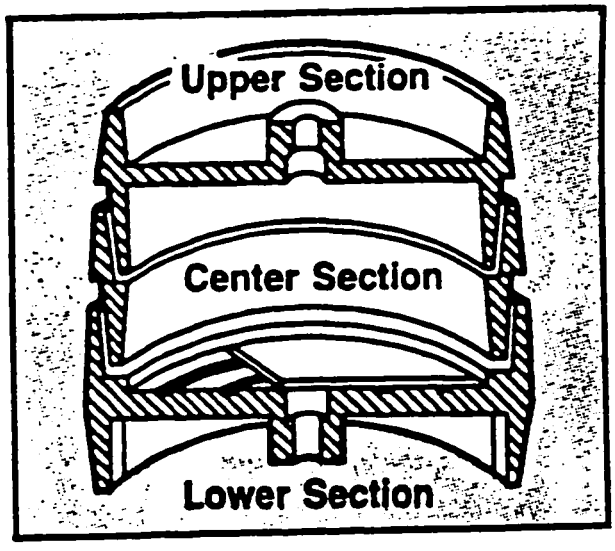

Figure 46. Diagram of an air sampling cassette.

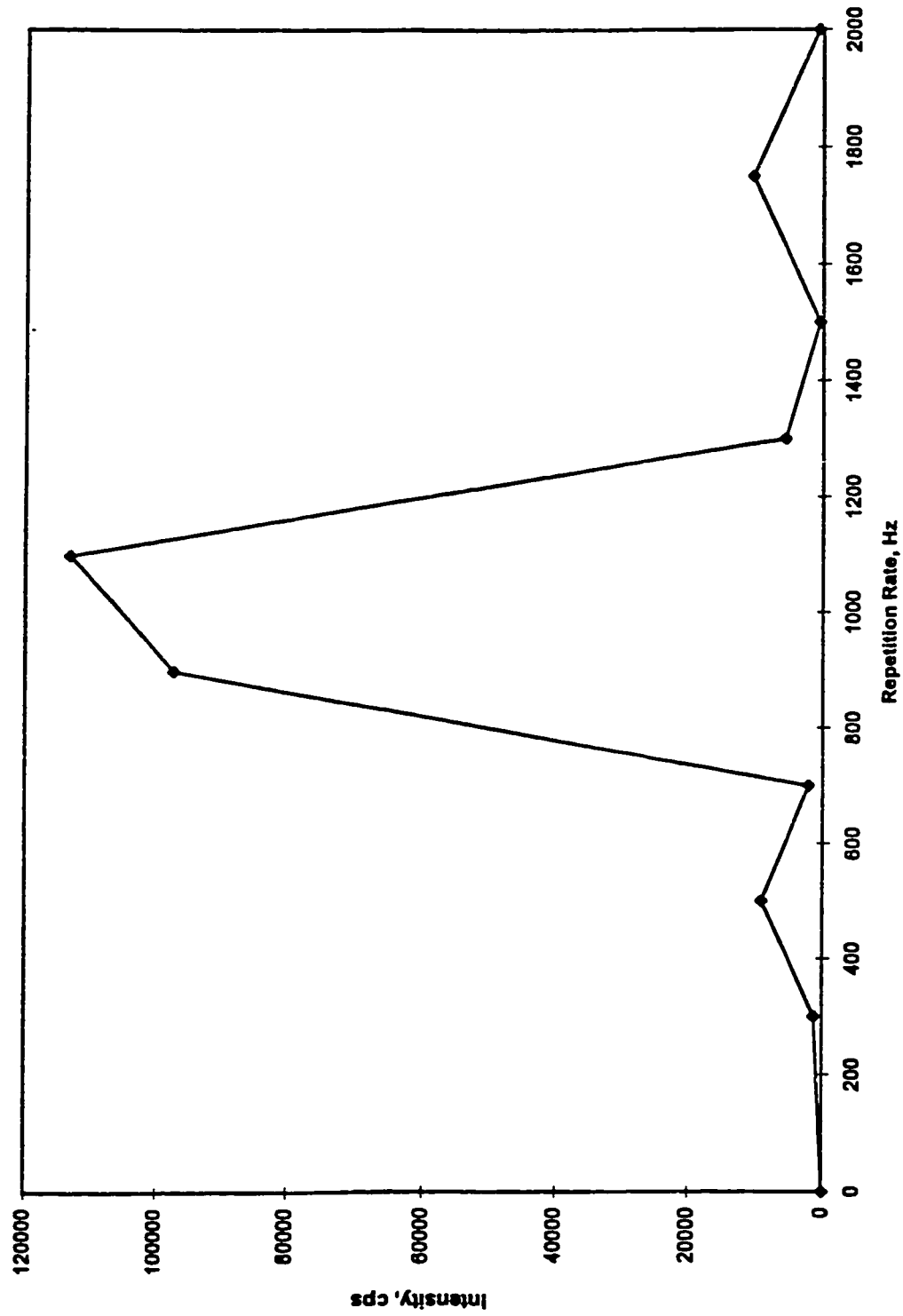

Figure 47. Ablated particles of NIST SRM 1106 passing through an air sampling cassette, for Cu 213.598.

plot of the repetition rate *vs.* signal intensity of ablated particles passing through the filter. The spark source was on for exactly one minute and the analysis was carried out on the ICP-AES after 30 seconds. The data represent raw intensity; no internal standardization was carried out. As **Figure 47** shows, there appears to be some clogging. It is possible, perhaps likely, that particles are condensing and clogging the filter so that particles cannot pass through to the ICP. **Figure 48** shows that the intensity of ablated particles passing through a filter does increase as the repetition rate of the spark source increases and then levels off beyond a certain frequency. It is also apparent that some clogging occurs. It is assumed that, at higher repetition rates, more material is ablated and the ablated particles condense to form larger particles which settle in the spray chamber, thereby failing to reach the plasma. It would be very beneficial to study the size and distribution of the ablated particles by means of scanning electron microscopy in the future.

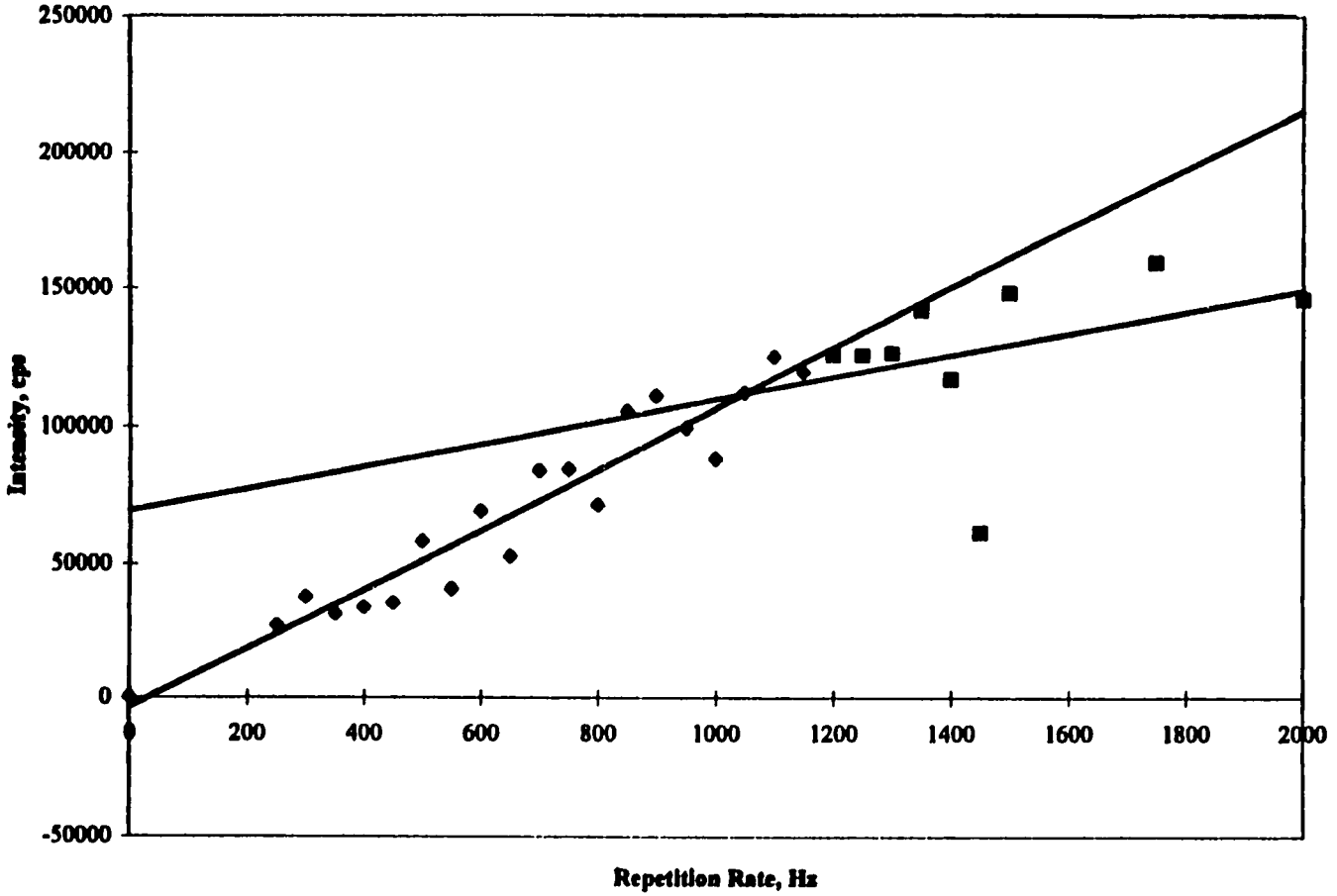

Figure 48. Ablated particles of NIST SRM 1106 passing through an air sampling cassette *vs.* repetition rate of the "zero-bias" spark source, for Cu 213.598.

Chapter 6

The Analysis of Aluminum Alloy Standards

Introduction

The auto industry has been encouraged to improve the environmental performance of the vehicles they produce. They have put much effort into the increased usage of lightweight materials for automotive parts to improve performance and fuel efficiency. Aluminum is an attractive candidate for structure, body, and engine applications due to its light weight and other performance attributes. An automobile today contains over 250 pounds of aluminum. Eighty five to ninety percent of aluminum in the automobiles can be reclaimed and recycled. Aluminum alloys of similar composition are recycled together. Other alloys are kept separate to preserve their value and characteristics in the recycling stream.[63] Aluminum products encompass three broad classes which are ingot, wrought products, and castings. Ingot is cast from aluminum furnaces and is later used in the production of wrought materials and castings. Wrought products are plate, sheet, foil, extrusions, tube, rod, bar, wire, and forging. Cast aluminum products are made by means of sand, permanent mold, and die-casting processes. Principal alloying elements for wrought alloys include Cu, Mn, Mg, and Zn, plus Si for cast alloys. When aluminum is recycled wrought alloys are worth considerably more as segregated scrap than mixed aluminum materials.[64]

A project in our laboratory[65] has been to identify wrought alloys from cast alloys by the "zero-bias" spark source coupled to the ICP-AES. The signal intensity of selected elements are then used to differentiate the different aluminum alloys.

Results and Discussion

Optimization of spark conditions for aluminum samples was performed in a slightly different fashion from the steel and brass standards. **Figure 49** shows the analytical characteristics for the peak current waveform of the spark source and argon flow rate for Mg 285.213. Mg has a percent composition of 0.65. The percent RSD was

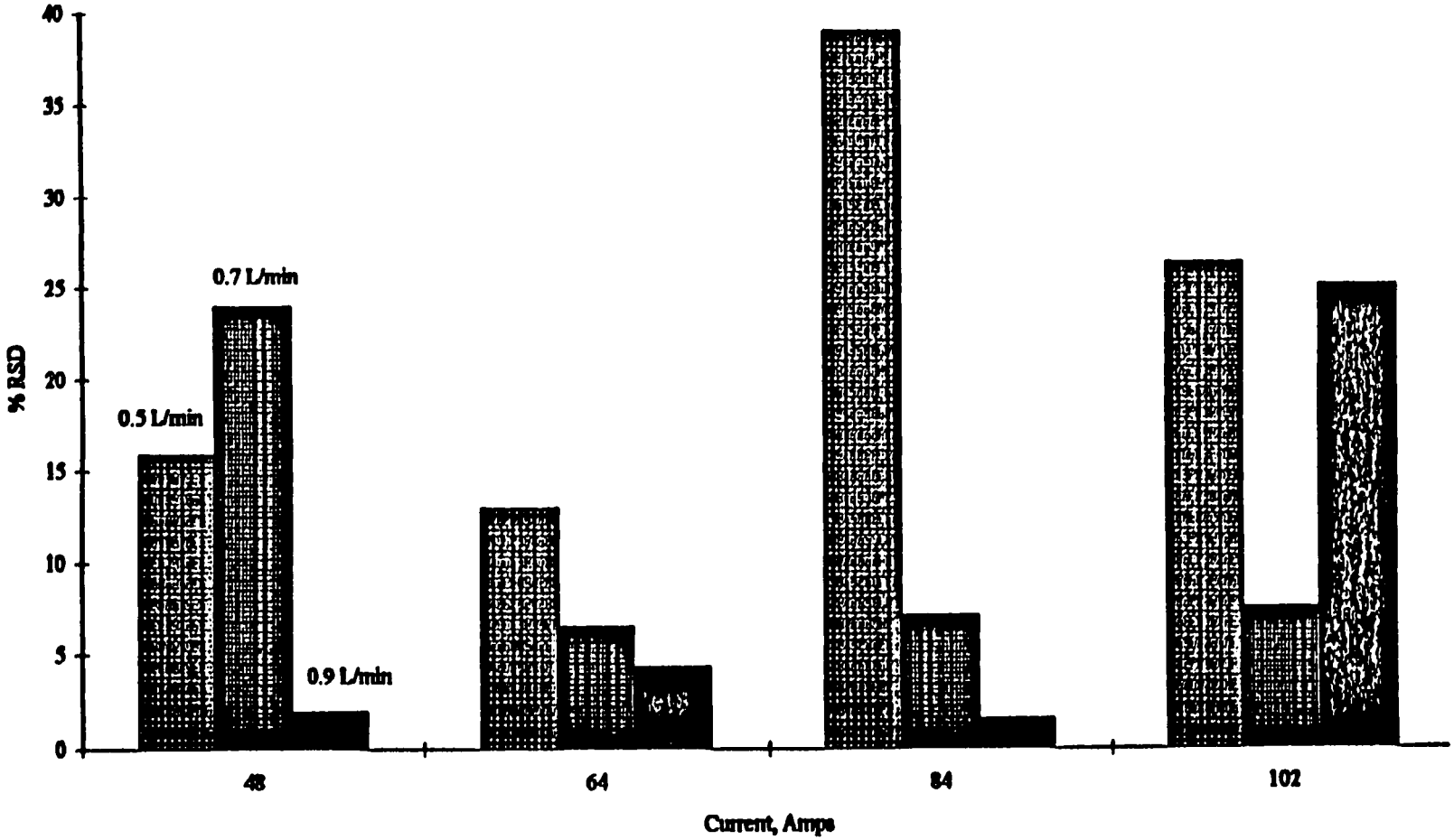

Figure 49. Analytical characteristics for the peak current waveform and argon flow rate for Mg for Alcoa Aluminum Alloys.

calculated from ten replicates to see which flow rate would provide the most stable spark discharge over time. From **Figure 49** it appears that 0.9 L/min provides the optimal spark discharge at the lower peak current waveforms. **Figure 50** shows the analytical characteristics for the current peak waveform of the spark source and RF power of the ICP-AES for Mg 285.213. An RF power of 1100 Watts shows the best stability at lower peak current waveforms. For this reason 1100 Watts was chosen to be optimal. The Analytical characteristics of the peak current waveform and the repetition rate of the spark source are shown in **Figure 51**. A repetition rate of 500 Hz shows the best stability. From **Figures 49, 50,** and **51** it is seen that higher peak current settings result in lower precision. There also appears to be no trend on the analytical characteristics for the parameters of the spark source or ICP-AES. **Table 18** shows the optimal conditions

Table 18. Optimal Conditions of the ICP-AES and "Zero-Bias" Spark Source for Aluminum Samples.

ICP-AES	
RF Power	**1100 Watts**
Argon Flow	
Nebulizer Flow	
Auxiliary Flow	**1.0 L/min**
Plasma Flow	**15 L/min**
Viewing Height	**15 mm**
Manual Integration Time	
Sampling Time	**500-10,000 ms**
Integration Time	**50-2000 ms**
Auto Background Correction	
Spark Source	
Repetition Rate	**500 Hz**
Peak Current	**60 Amps**
Spark Duration	**5 ms**
Pseudo-Triangular Waveform	
Spark Bias Current	**≈ 0 Amps**
Argon Flow	**0.9 L/min**
Preburn	**30 Seconds**
Spark Electrode Gap	**2.00 mm**

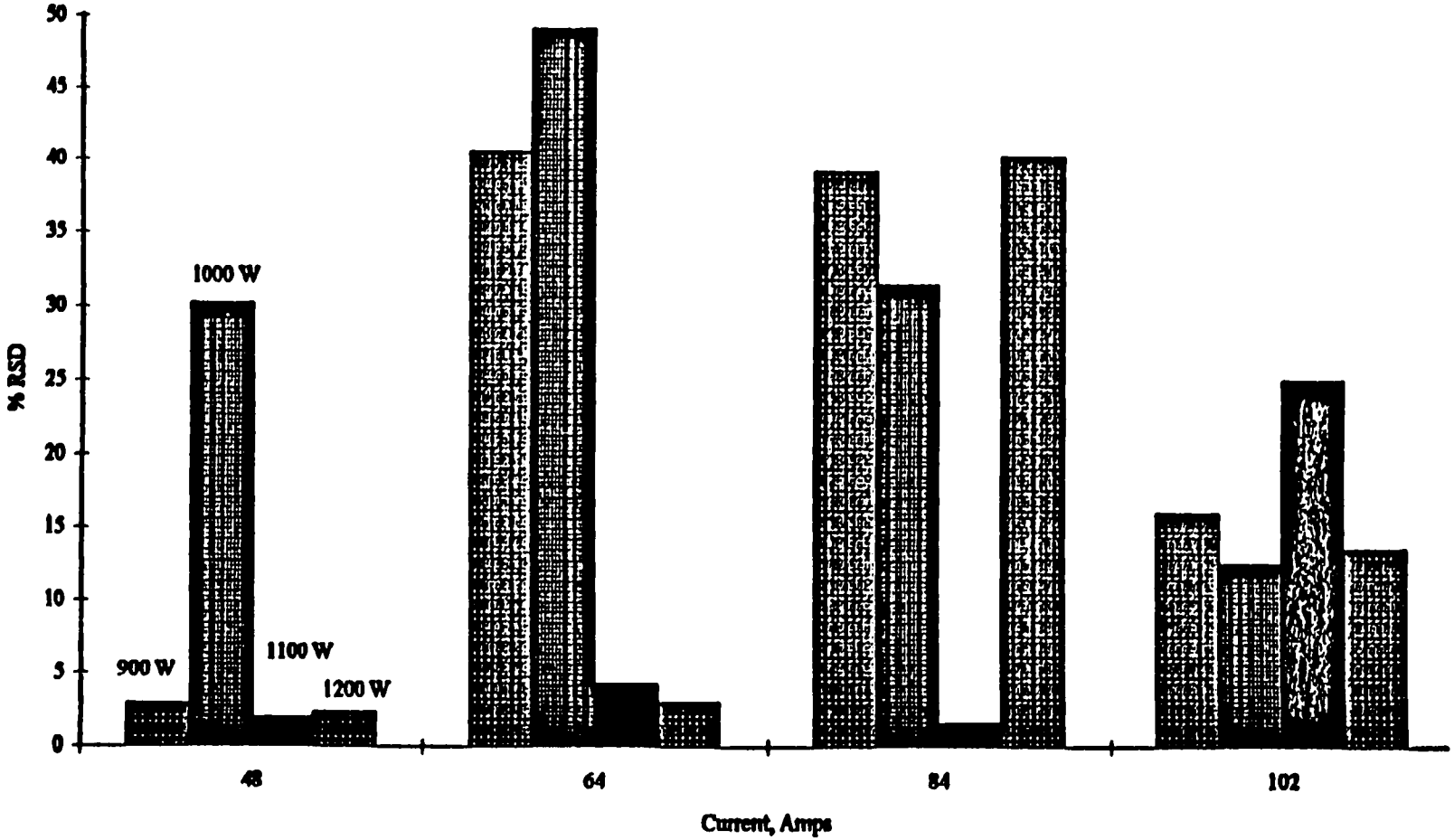

Figure 50. Analytical characteristics for the current peak waveform and RF power for Mg for Alcoa Aluminum Alloys.

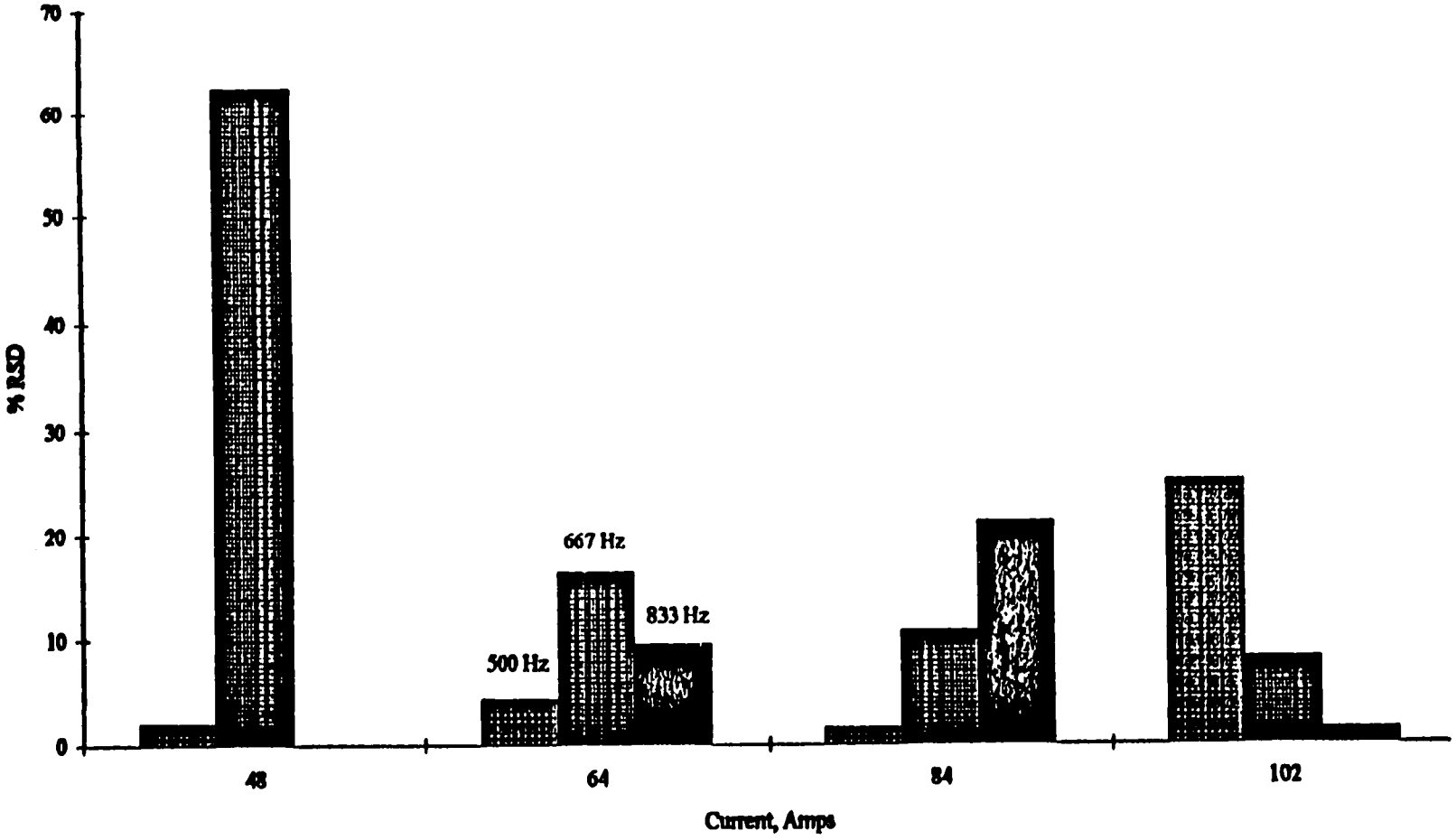

Figure 51. Analytical characteristics for the current peak waveform and repetition rate for Mg for Alcoa Aluminum Alloys.

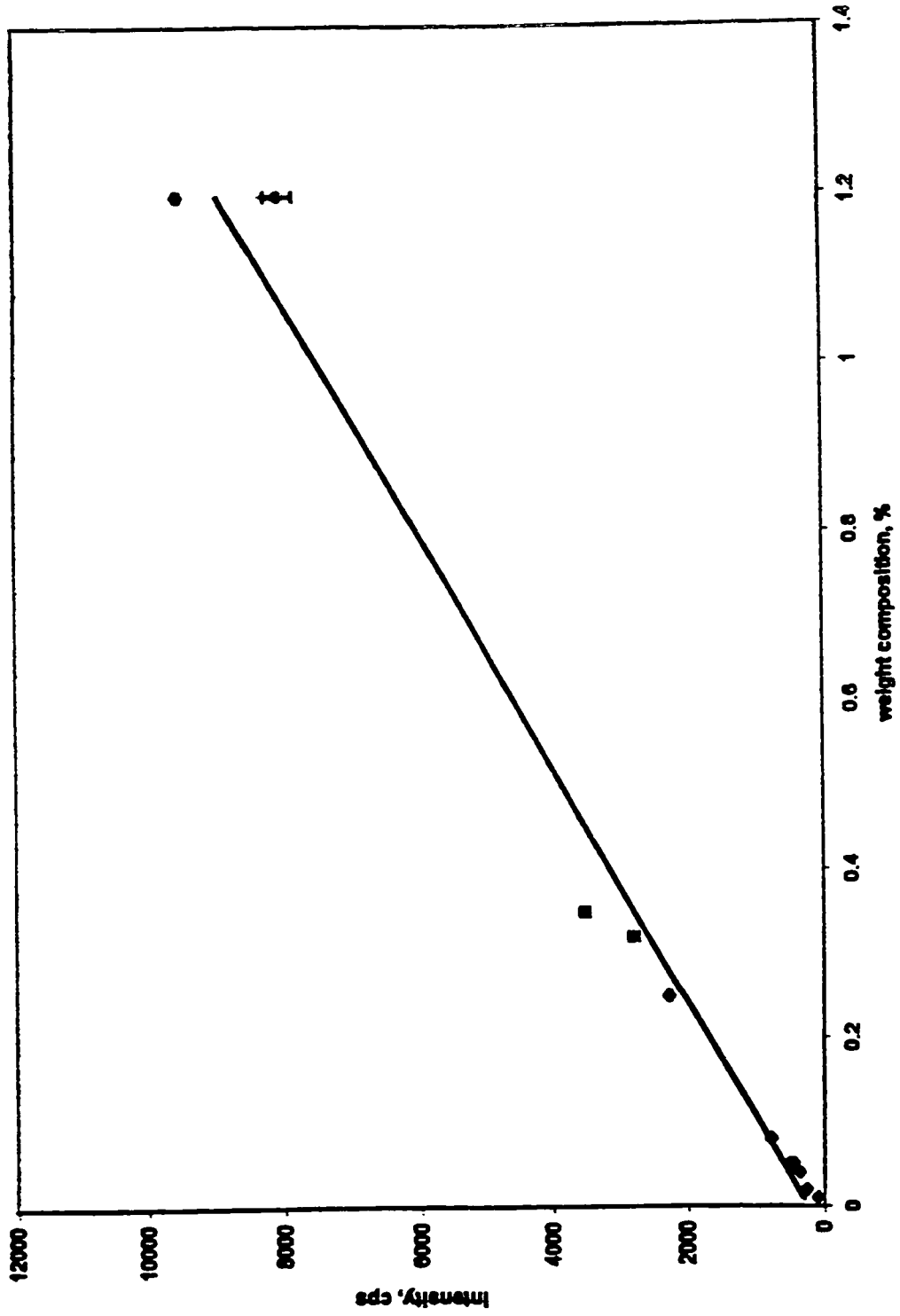

Figure 52. Calibration curve for Alcoa Aluminum Alloys of Mn.

chosen for the aluminum samples.

The linearity in spectral line intensity achieved with the "zero-bias" spark source as a solid sampling device for ICP-AES has been shown previously. **Figure 52** shows a calibration curve for Alcoa Aluminum Wrought Alloys of Mn at a wavelength of 257.610. The correlation coefficient is 0.983. The plot shows that linearity is achieved over three orders of magnitude. **Tables 11** and **12** also show excellent correlation coefficients for other elements over a range of three orders of magnitude. It is believed that the new spark source does not limit the fundamental capabilities of the ICP-AES and, therefore, linearity over an even greater range is possible. This could not be demonstrated since standards are not available.

Figure 53 shows a time profile, which was explained in detail previously, for Alcoa Aluminum Alloy 7075. The percent composition for Mg, Ti, and Fe is 2.60, 0.04, and 0.25, respectively. An integration time of 0.1 s was used. The intensities for Ti and Fe are not as stable as Al and Mg. A longer integration time would result in more stability for the minor constituents. The ICP-AES is reading replicates every six seconds continuously for approximately 12 minutes. During this time the spark source is turned on and left on for roughly five minutes. A pseudo-steady state intensity is reached within 20 seconds after the spark source is turned on. The spark source is then turned off; minor constituents such as Ti and Fe return to their baseline value within 20 seconds. It takes up to 70 seconds for the major constituents Al and Mg to reach their baseline values. This carryover could result from ablated particles deposited on the tygon tubing. When the spark source is then turned on again, it takes approximately 20 seconds to re-establish a pseudo-steady state intensity. The intensity also shows more stability the second time the spark source has been turned on.

Ablated particles are deposited on the chamber walls of the sample holder, transport tubing, and the spray chamber causing sample carry over to be of potential concern. Oudsema[66] observed similar results with a high-voltage spark source coupled to

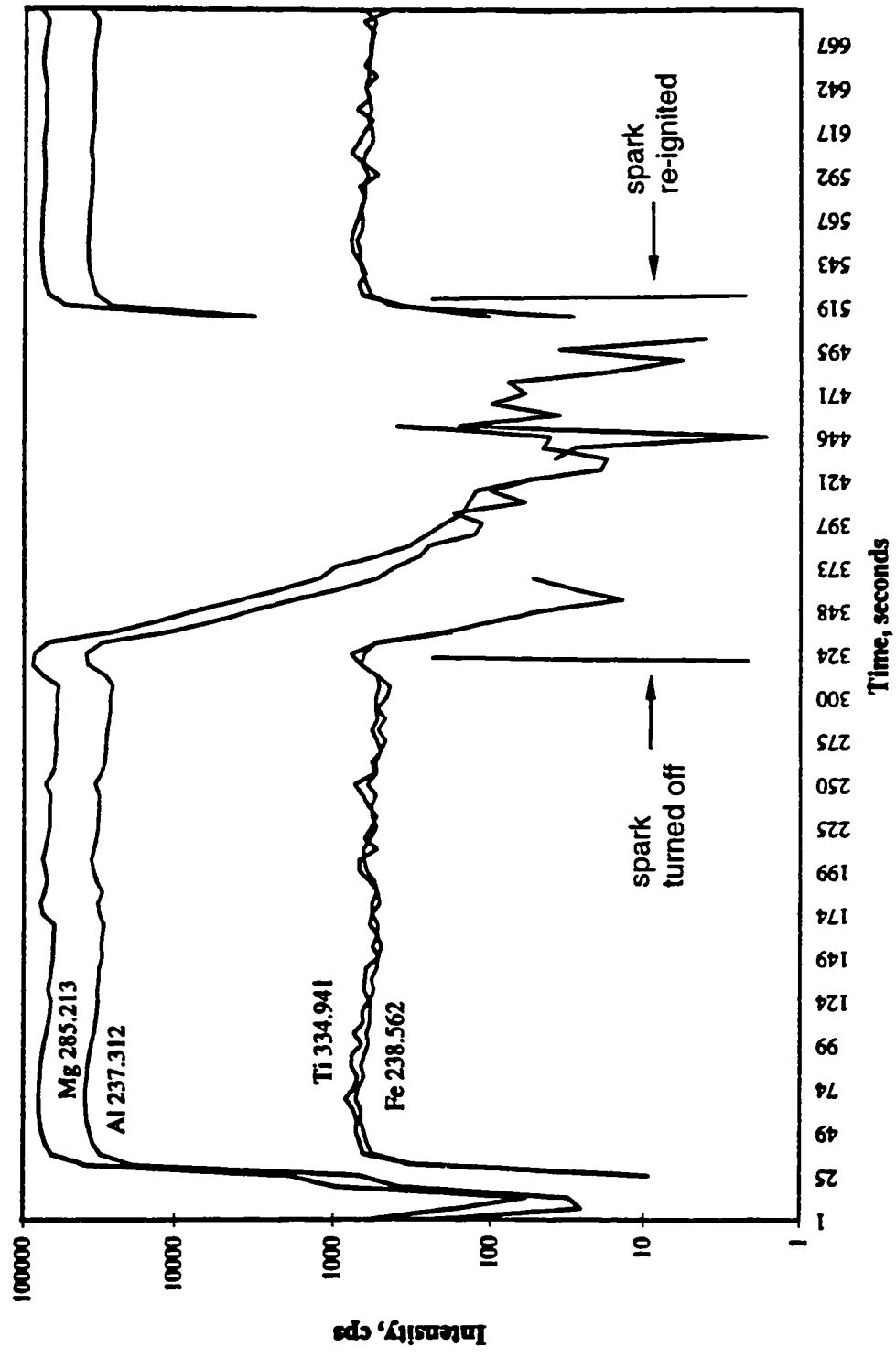

Figure 53. Time profile for Alcoa Aluminum Alloy SS-7075.

an ICP-MS. Once a significant amount of ablated material was deposited, it was necessary to disassemble and clean the sample holder and tygon tubing. By rinsing with alcohol and drying, a procedure requiring approximately 10 minutes.

Table 19 shows a comparison of signal intensity for Alcoa Aluminum Alloy 1100 for samples run on two different days. The first column of intensities is the mean of five analyses where each analysis represents a different burn at a different position on the alloy. The second column is the mean of ten analyses. Internal standardization was carried out each day using a less intense wavelength of Al as an internal standard. RSD values within a few percent are achieved for each element except for Zn. The intensity for Zn is low and it is likely that an insufficient integration time was used. As stated above, an on-going project in this laboratory is examining the intensity of selected elements in order to differentiate between the different alloys. **Table 20** shows a comparison of Cr intensities at a wavelength of 357.869 for the wrought alloys. Each alloy was analyzed on two separate days, five analyses of the sample were carried out one day and ten analyses on the next day. Each value represents a different burn at a different location on the alloy. The mean of the samples for each day is used to compare the signal intensity. The lowest % RSD value should be obtained when comparing each alloy to itself; these values are underlined. There are some discrepancies when the weight

Table 19. Comparison of Signal Intensity for Alcoa Aluminum Alloy 1100 Between Two Days.

Element	Wavelength	elemental composition (wt. %)	Intensity day 1	Intensity day 2	% RSD
Si	288.158	0.18	113.78	112.64	0.71
Fe	238.204	0.50	270.88	276.05	1.34
Cu	324.754	0.15	4735.18	4708.01	0.41
Mn	260.569	0.04	235.76	234.92	0.25
Mg	279.079	0.03	2463.06	2413.87	1.43
Zn	202.548	0.08	16.02	13.73	10.88
Ti	334.941	0.02	745.74	747.18	0.14

Table 20. Comparison of % RSD Values of Signal Intensity for Cr at a Wavelength of 357.869 Between Two Days for Alcoa Aluminum Wrought Alloys.

	1100	2024	2036	3003	3004	5052	5182	5252	6010	6061	6063	7021	7075
1100	11.56	106.5	126.4	7.63	31.80	137.8	116.6	29.10	124.7	137.3	104.1	114.8	137.9
2024	114.4	9.30	53.16	107.3	120.9	114.3	17.54	120.2	45.89	111.1	14.71	11.99	115.4
2036	130.5	70.08	11.60	127.2	133.2	80.31	47.93	132.8	19.78	74.22	74.11	52.83	82.49
3003	15.60	104.7	125.6	3.56	35.64	137.6	115.3	32.98	123.8	137.1	102.2	113.3	137.7
3004	23.39	119.1	132.1	41.57	2.85	139.2	125.8	5.67	131.0	138.9	117.5	124.6	139.3
5052	138.3	117.4	87.89	137.4	139.1	0.12	107.6	139.0	92.80	8.80	119.0	109.9	3.13
5182	125.6	47.80	15.40	121.1	129.5	96.68	22.62	129.0	7.16	91.86	52.56	28.05	98.39
5252	36.37	122.8	133.7	53.61	16.37	139.6	128.4	19.15	132.8	139.3	121.0	127.4	139.7
6010	126.2	50.26	12.63	121.8	129.9	95.17	25.34	129.5	4.37	90.22	54.95	30.73	96.92
6061	138.6	119.2	91.43	137.7	139.3	6.04	110.0	139.2	96.08	14.68	120.7	112.2	2.79
6063	122.5	35.17	28.88	117.1	127.0	103.6	8.97	126.5	20.85	99.35	40.23	14.55	105.0
7021	122.8	36.62	27.40	117.5	127.3	102.8	10.51	126.8	19.33	98.47	41.64	16.07	104.3
7075	138.8	121.1	95.43	138.0	139.5	13.10	112.7	139.4	99.77	21.66	122.6	114.7	9.87

Table 21. Percent Composition of Cr in Aluminum Wrought Alloys.

Wrought Alloys	weight percent
SS-1100	NQ
SS-2024	0.06
SS-2036	0.05
SS-3003	NQ
SS-3004	NQ
SS-5052	0.25
SS-5182	0.03
SS-5252	NQ
SS-6010	0.04
SS-6061	0.23
SS-6063	0.02
SS-7021	0.03
SS-7075	0.22

compositions of Cr are within 0.05% for different alloys. **Table 21** shows the weight percent of Cr in the aluminum wrought alloys. Due to the observed discrepancies, multiple elements must be used to differentiate between alloys.

The Aluminum Alloys were provided by the Alcoa Corporation. They are "in-house" secondary standards which were produced and analyzed by Alcoa. They are not characterized to the degree expected of NIST standards. An article has been published on the great care taken in the preparation and analysis of standard samples supplied by NIST.[67] Nonetheless, results of the aluminum alloys from the "zero-bias" spark source indicate that accuracy and precision are within a few percent.

Chapter 7

The Analysis of Gold Standards

Introduction

The determination of constituents in precious metals is usually carried out by fire assay. Minor and trace elements are then determined through spectrometric methods. A new method is needed that can quickly determine constituents in gold samples with minimal sample preparation. The Royal Canadian Mint has lent fine gold reference materials which have certified concentrations of its constituents. These elements are present as impurities in fine gold; hence it is important to accurately determine the composition of these elements in assessing the fineness of the precious metal product.

Results and Discussion

Table 22 shows the concentration of trace elements present in the Fine Gold Reference Materials. As shown the elements are present in trace amounts. For this reason, optimizing of the parameters was carried out in a different fashion than previously described. When studying other sample matrices, emission intensity increases as a result of increasing the RF power. For this reason, an RF power of 1200 Watts was used. An argon flow rate of 0.5 L/min was used for optimal residence time. Various repetition rates, currents, and integration times were investigated to determine conditions that gave optimal detection limits and stability. **Figures 54** and **55** show spectra for Mg at a wavelength of 279.079. The spectra in **Figure 54** were obtained at a repetition rate of 500 Hz and those in **Figure 55** at a repetition rate of 1000 Hz. The peak is more "defined" at a repetition rate of 1000 Hz. An integration time of 1.0 s and a sampling time of 10.0 s were chosen to allow enough time for adequate detector performance. Previously it was noted that at higher repetition rates the spark discharge is unstable and precision is poorer. Precision is also poorer at higher currents. **Table 23** shows the operating conditions used for the gold standards.

Table 6 shows the relative intensities obtained during spark ablation of FAU 8

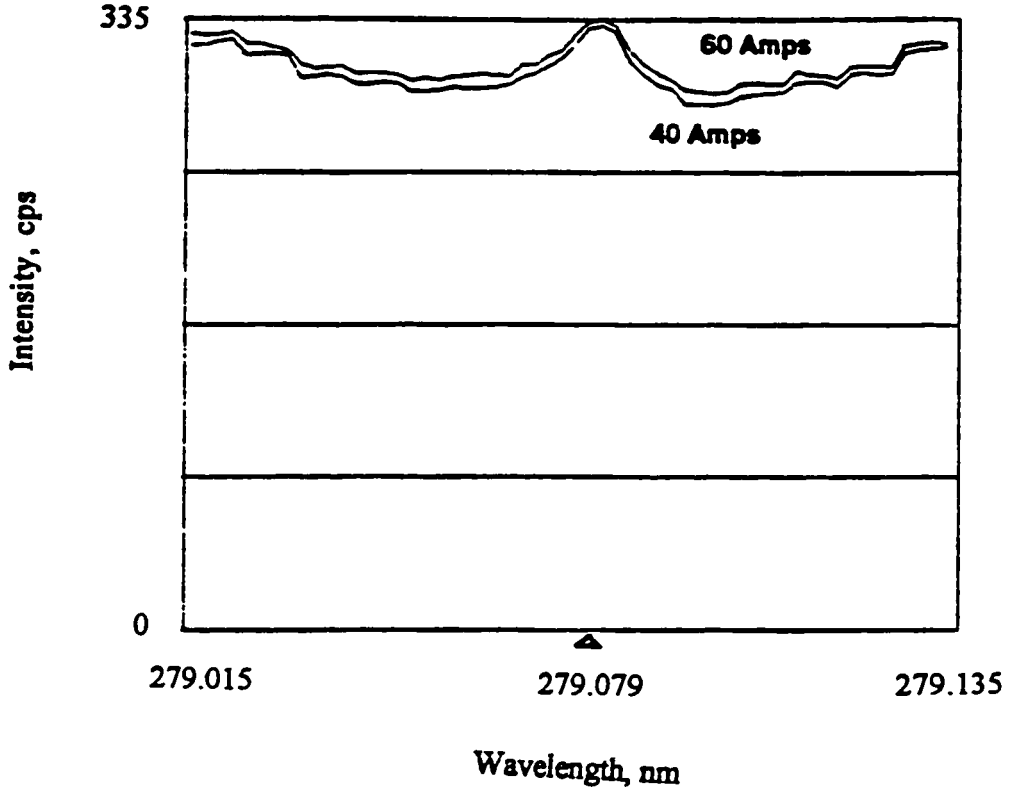

Figure 54. Spectra of Mg 279.079 at a repetition rate of 500 Hz.

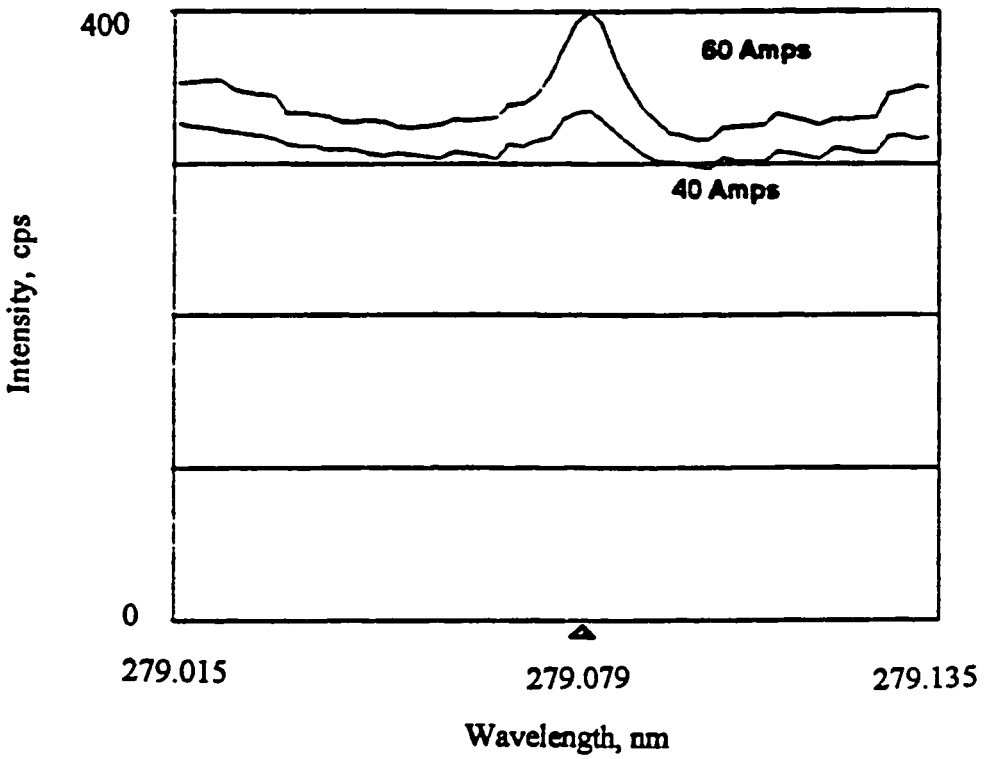

Figure 55. Spectra of Mg 279.079 at a repetition rate of 1000 Hz.

Table 22. Concentrations (μg/g) of Trace Elements in Fine Gold Reference Materials.

Element	FAU 6	FAU 7	FAU 8	FAU 9	FAU 10	FAU 11
Ag	9.5	20.3	81.7	7.1	49.7	15.1
As	2.4	10.0	18.0	6.7	29.4	14.3
Bi	3.4	24.0	34.0	6.8	53.9	11.0
Cr	1.7	32.6	13.3	8.1	4.9	16.7
Cu	1.6	98.1	46.9	5.7	9.8	13.8
Fe	6.2	11.6	33.8	7.5	90.4	15.4
Mg	1.1	34.0	11.8	6.0	3.2	15.6
Mn	1.1	58.9	22.5	10.8	64.3	20.5
Ni	2.7	32.5	50.5	5.7	14.6	13.5
Pb	1.9	21.9	30.5	6.4	49.7	11.5
Pd	1.3	43.1	19.8	5.0	119.0	13.1
Pt	NQ	87.1	40.8	6.1	5.1	12.5
Si	NQ	2.7	27.8	6.3	9.0	19.1
Sn	2.8	33.8	27.2	6.4	49.7	17.8
Ti	0.7	12.7	25.3	5.9	2.6	16.5
Zn	2.6	54.6	6.6	7.5	20.9	12.5

Fine Gold Reference Material where the ICP-AES is operated in the peak area mode. When analyzing trace constituents, it is better to use the peak height mode. The detector integrates the area of the peak when operating in the peak area mode and takes the intensity of the highest point of the peak when operating in the peak height mode. In peak area mode, it was found that the detector was integrating the area of the entire window instead of just the peak; as seen in **Figure 56**, this can make a profound difference. **Table 24** contains data recalculated from **Table 6** using the peak height mode. The data represent raw counts where no internal standardization was carried out for this experiment. A few of the elements have very poor precision. Under the current operating conditions, detection limits for these elements were too low for the ICP-AES to detect reliably. If a higher repetition rate and current were used, detection limits would likely be improved. Repetition rates of 1500 Hz and 2000 Hz each with a current of 100 amps were used to see if detection limits would improve. **Figures 57** and **58** show

Table 23. Operating Conditions of the ICP-AES and "Zero-Bias" Spark Source for Gold Samples.

ICP-AES	
RF Power	**1200 Watts**
Argon Flow	
Nebulizer Flow	
Auxiliary Flow	**1.0 L/min**
Plasma Flow	**15 L/min**
Viewing Height	**15 mm**
Manual Integration Time	
Sampling Time	**10,000-60,000 ms**
Integration Time	**1000-6000 ms**
Auto Background Correction	
Spark Source	
Repetition Rate	**1000 Hz**
Peak Current	**100 Amps**
Spark Duration	**5 ms**
Pseudo-Triangular Waveform	
Spark Bias Current	**≈ 0 Amps**
Argon Flow	**0.5 L/min**
Preburn	**30 Seconds**
Spark Electrode Gap	**2.00 mm**

spectra of Pb and Bi at these conditions and also the previous conditions used in **Tables 6, 10**, and **24**, 1000 Hz and 60 amps. A repetition rate of 1500 Hz and current of 100 amps did not improve the detection limits; it often just shifted the baseline. On the other hand, a repetition rate of 2000 Hz and 100 amps did improve the detection limits for both elements. Unfortunately, experiments at these latter conditions could not be carried out due to potential damage to the high voltage diodes currently in use. The poor % RSD values in **Table 10** can be explained in the same manner.

As stated previously, longer integration times typically resulted in better detection limits and improved analyte precision. Therefore, the integration time for the elements As, Bi, Mg, Pb, Pt, and Sn was increased from 1.5 to 6.0 s to see if the detection limits would improve. **Table 25** shows percent RSD values for five analyses of FAU 11.

Table 24. "Readback" of FAU 10, Fine Gold Reference Material Operating in the Peak Height Mode.

Element	Wavelength	Intensity (cps)	elemental composition (ppm)	mean (ppm)	% RSD
Ag	328.068	10215.1	49.7	50.6	1.27
As	228.812	9.1	29.4	27.8	3.95
Bi	223.061	77.3	53.9	56.6	3.45
Cr	205.552	32.3	4.9	4.7	2.95
Cu	324.754	1939.8	9.8	14.9	29.20
Fe	238.204	573.8	90.4	93.9	2.69
Mg	279.079	15.7	3.2	3.1	2.24
Mn	257.610	4595.2	64.3	63.8	0.55
Ni	231.604	94.25	14.6	14.6	0
Pb	220.353	68.9	49.7	49.6	0.14
Pd	340.458	1640.2	119.0	121.8	1.64
Si	251.611	156.2	9.0	9.2	1.55
Sn	235.484	31.9	49.7	53.5	5.21
Ti	334.941	312.0	2.6	2.6	0
Zn	334.502	316.9	20.9	21.6	2.33

The five analyses were obtained at five different locations on the sample electrode and the ICP-AES is operating in the peak height mode. As, Bi, and Pb still have poor precision, but the other three elements were within an acceptable range (a few percent).

A calibration curve was created for the elements using standard reference materials FAU 6, FAU 8, FAU 9, FAU 10, and FAU 11. FAU 7 was analyzed as a sample. The results are shown in **Table 26**. The elements with a low or high recovery are the elements for which the ICP-AES could not reach the detection limits with the conditions used for this experiment.

An instrument calibration curve was generated based on the ablation of FAU 7. FAU 8 was run as an unknown. Results of these determinations are given in **Table 27** along with certified values. As can be seen such preliminary results are very encouraging. Most elements are in good agreement with the certified values.

Integration time and reading time were 1 and 10 s, respectively, in experiments

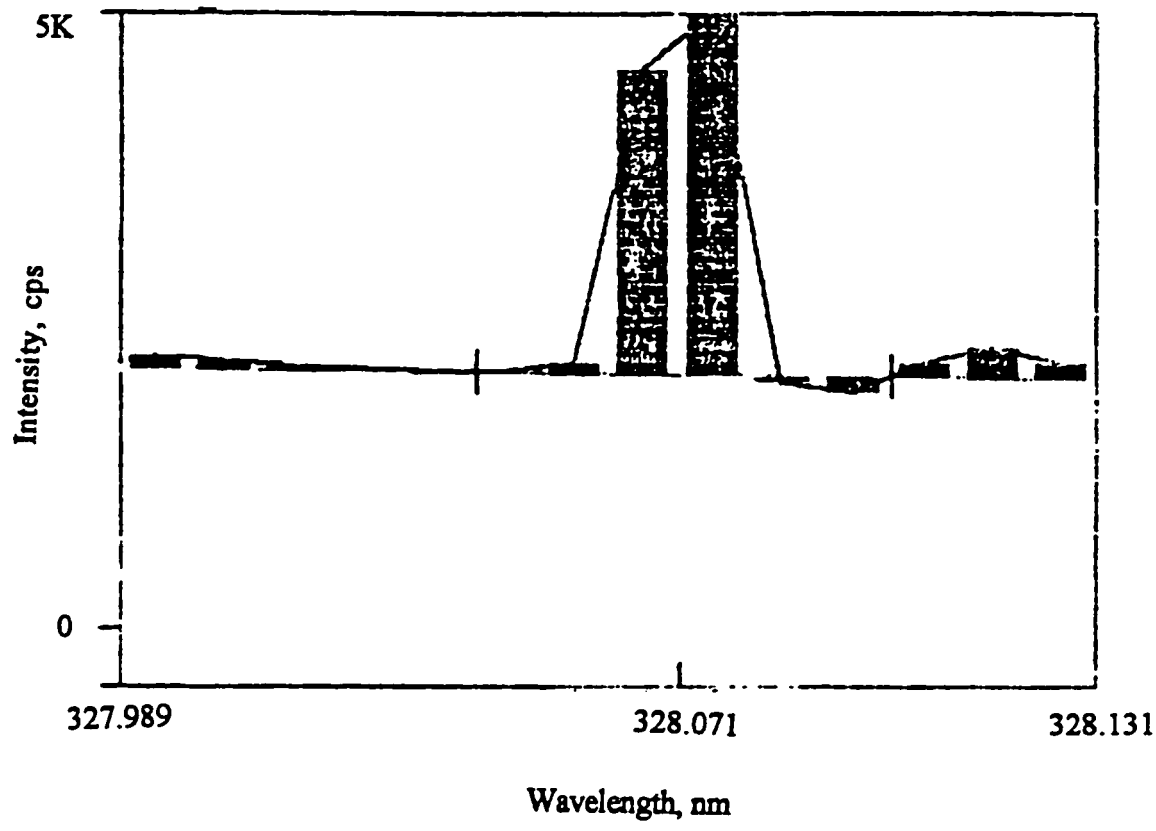

Figure 56. Area integrated for FAU 8 for the element Ag at a wavelength of 328.068.

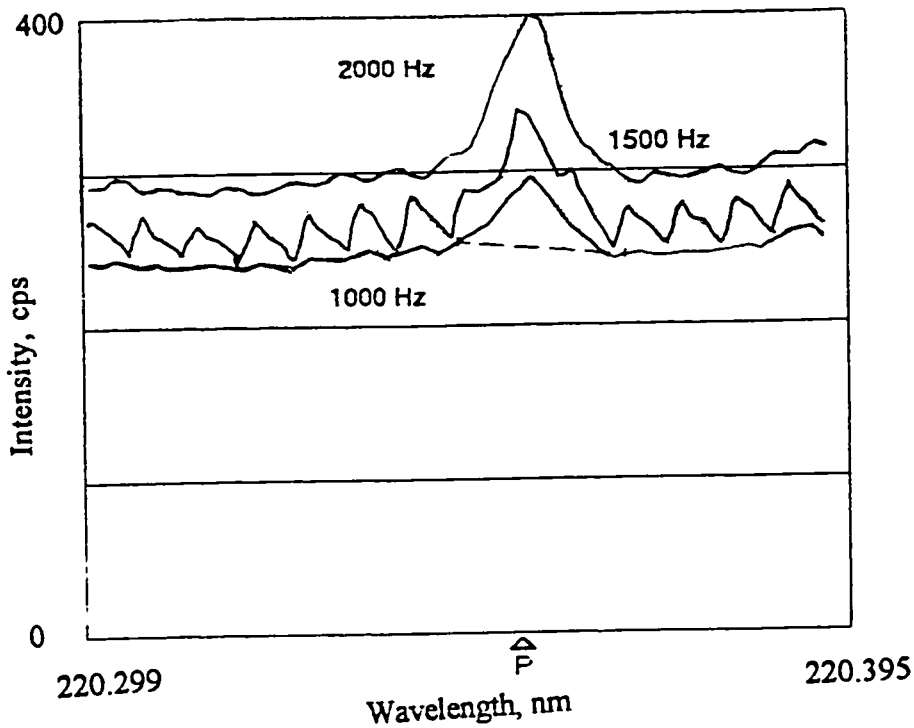

Figure 57. Spectra of Pb at a wavelength of 220.353 at repetition rates of 2000, 1500, and 1000 Hz.

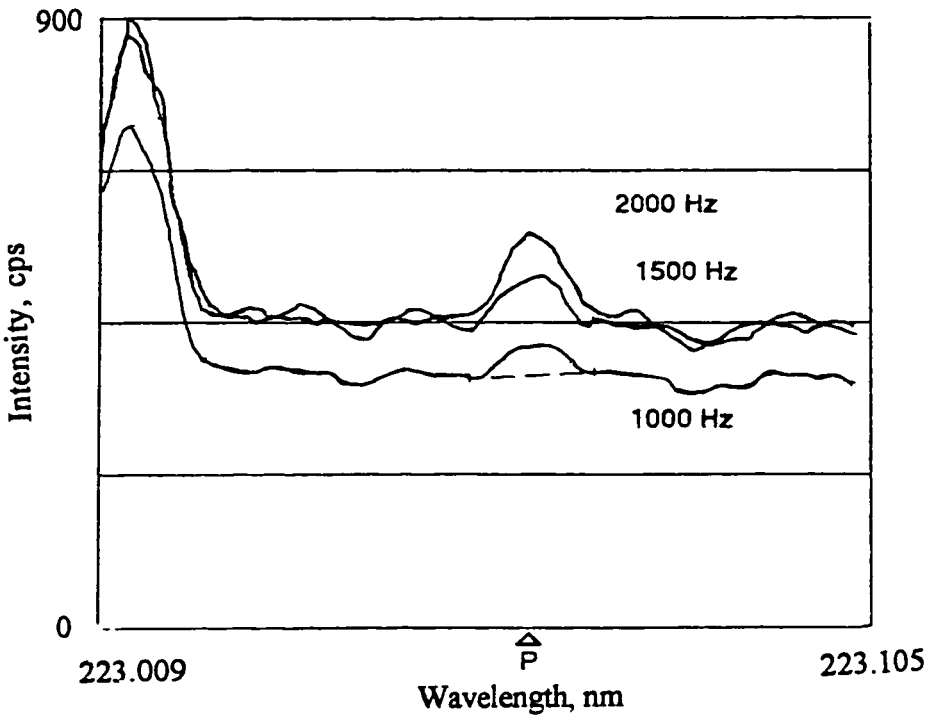

Figure 58. Spectra of Bi at a wavelength of 223.061 at repetition rates of 2000, 1500, and 1000 Hz.

Table 25. Relative Intensities Obtained During Spark Ablation of FAU 11.

Element	Wavelength	elemental composition (μg/g)	mean (cps)	% RSD
Ag	328.068	15.1	3038.47	1.51
As	228.812	14.3	6.76	8.29
Bi	223.061	11.0	19.26	15.91
Cr	205.552	16.7	161.06	1.67
Cu	324.754	13.8	4328.60	37.80
Fe	238.204	15.4	219.84	33.69
Mg	279.079	15.6	78.32	4.16
Mn	257.610	20.5	1158.16	2.51
Ni	231.604	13.5	132.52	1.93
Pb	220.353	11.5	20.82	5.99
Pd	340.458	13.1	196.40	0.91
Pt	214.423	12.5	35.77	2.67
Si	251.611	19.1	92.44	6.27
Sn	235.484	17.8	13.15	4.02
Ti	334.941	16.5	2068.71	1.23
Zn	334.502	12.5	264.97	4.42

discussed thus far. When they were increased to 3 and 60 s, respectively, the precision for Cu and Fe improved. Four analyses were carried out on FAU 9 each being a different burn at a different location on the sample. **Table 28** shows the % RSD values obtained. It is believed at the lower integration time and reading time that the ICP-AES was not reaching the detection limits. Allowing the detector to collect additional readout on the elements enabled the ICP-AES to reach the detection limits of Cu and Fe.

A commercially available CETAC Spark Source was used to analyze the Fine Gold Reference Material.[68] The CETAC unit is a medium voltage spark source. **Figure 59** shows a comparison of burn patterns on gold reference material FAU 6 for the (a) "zero-bias" spark source and the (b) CETAC unit. These are typical burns and measure approximately 1.8 and 4.2 mm in diameter for the "zero-bias" spark source and CETAC unit, respectively. The effects of the bias current can be clearly seen in **Figure 59(b)**. It appears that the sample is oxidized around the burn, but actually the secondary

Table 26. Recovery of FAU 7.

Element	Wavelength	Measured Value (μg/g)	Certified Value (μg/g)	% Recovery
Ag	328.068	19.3	20.3	95.1
Bi	223.061	40.1	24.0	167.1
Cr	205.552	29.9	32.6	91.7
Cu	324.754	64.0	98.1	65.2
Fe	238.204	4.2	11.6	36.2
Mg	279.079	39.8	34.0	117.0
Mn	260.569	55.0	58.9	93.4
Ni	231.604	31.6	32.5	97.2
Pb	220.353	22.7	21.9	103.7
Pd	340.458	42.8	43.1	99.3
Pt	213.423	59.2	87.1	68.0
Si	288.158	3.8	2.7	114.8
Sn	189.933	31.8	33.8	94.1
Ti	334.941	11.6	12.7	91.4
Zn	213.856	47.7	54.6	87.4

Table 27. Data Generated for FAU 8 From Response Curve of FAU 7.

Element	Wavelength	Measured Value (μg/g)	Certified Value (μg/g)	% Recovery
Ag	328.068	85.6	81.7	104.8
As	228.812	13.3	18.0	73.9
Bi	223.061	40.1	34.0	117.9
Cr	205.552	13.0	13.3	94.9
Cu	327.396	54.4	46.9	116.0
Fe	238.204	33.6	33.8	99.4
Mg	279.079	11.4	11.8	96.6
Mn	257.610	23.3	22.5	103.6
Ni	231.604	52.7	50.5	104.4
Pb	220.353	32.7	30.5	107.2
Pd	340.458	19.7	19.8	99.5
Pt	214.423	42.5	40.8	104.2
Si	288.158	10.2	27.8	36.7
Sn	189.933	29.7	27.2	109.2
Ti	334.941	28.6	25.3	113.0
Zn	213.856	16.3	6.6	247.0

discharge is wandering as discussed previously. This wandering increases the sampling area to 11.7 mm in diameter.

The scientists using the CETAC unit were able to achieve detection limits of 10 ppm.[68] They coupled their spark source to an axial view ICP-AES. With the axial view ICP, the photons from the plasma are collected along the axis. This improves the detection limits five- to ten-fold.[69] The ICP-AES used with the "zero-bias" spark source was a radial view ICP. Photons are collected at a 90 degree angle to the plasma with the radial view ICP. **Figure 60** shows the difference between axial and radial view ICP-AES. With the parameters used in our experiments, typical detection limits of 5-20 ppm were achieved. These are comparable, and likely even better than, the detection limits with the CETAC unit.

Table 28. Relative intensities for Cu and Fe obtained during spark ablation of FAU 9.

Element	Wavelength	elemental composition (μg/g)	mean (cps)	% RSD
Cu	324.754	5.7	1136.9	4.38
Fe	238.204	7.5	51.7	5.16

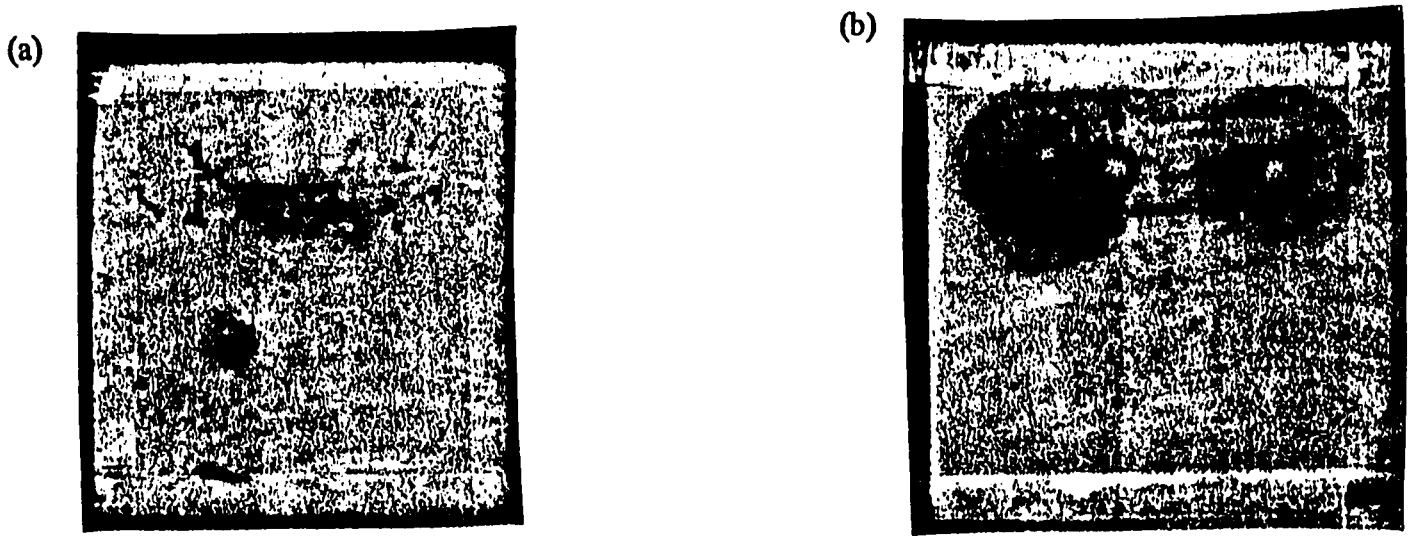

Figure 59. Comparison of burn patterns for the (a) "zero-bias" spark source and the (b) CETAC unit.

(a)

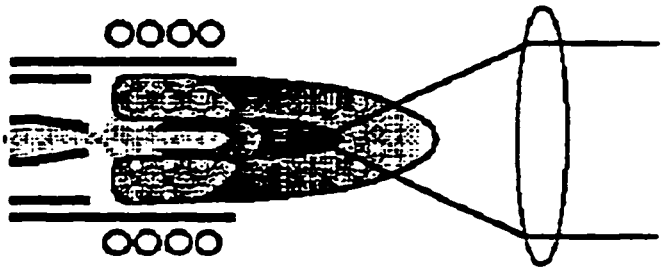

(b)

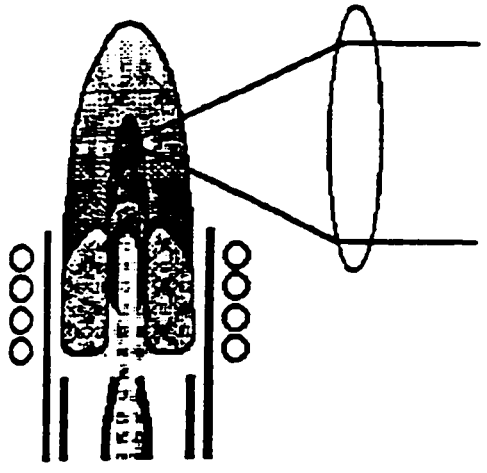

Figure 60. (a) Axial view ICP and (b) radial view ICP.

Chapter 8

Conclusions and Future Work

Conclusions

Initial work was carried out to investigate the "zero-bias" spark source as a solid sampling device for ICP-AES. The low voltage "zero-bias" spark source was developed by Coleman in collaboration with the Perkin-Elmer Corporation. The concept of this spark source is to separate the initial gap ionization and current injection circuits. This concept accurately stores the potential needed, or the amount of power desired to be dissipated, in the current waveform storage and "shaping" network circuit and separately ionizes the breakdown of the gap in the gap ionization section. This can eliminate bias current and, as a result, a positionally stable discharge can be achieved. The high voltage which is customarily present in the spark discharge and post-discharge periods of time for conventional spark sources is only present for a few ns in order to create seed electrons in the electrode gap. The small continuous bias current is characteristic of conventional spark sources and gives rise to positional instability and "secondary" sampling resulting in undesirable and poor test results.

For a solid sampling device to be useful it must be able to analyze different types of samples. The "zero-bias" spark source was successfully applied to a wide variety of sample matrices. These matrices included steels, brasses, aluminum, and gold standards. The experiments carried out show the versatility of the "zero-bias" spark source as a solid sampling device for ICP spectrometry.

The analysis of solid samples using a spark ablation device eliminates the time consuming sample preparation, poor recovery of analytes, and spectral interferences caused from the acidic medium resulting from the dissolution of a sample. Coupling a spark source to an ICP-AES separates the sampling and detection processes allowing each to be optimized independently. Initial work using a "zero-bias" spark source indicates the capability of the approach for direct solid analysis of conductive samples. Solid

sampling differs from liquid nebulization wherein spark ablation transient introduction of ablated materials derives from spark conditions. Therefore, investigation of the spark parameters were carried out. It is apparent that spark stability and sampling efficiency are dependent on operating conditions. Especially important are the peak current, repetition rate, spark electrode gap, and integration time. An increase in repetition rate increases the amount of sample being ablated. A simultaneous proportional increase in ICP-AES signal intensity does not occur. Signal intensity initially increases linearly with frequency, but at some point the intensity tends to level off with increasing repetition rate. This may be characteristic of changes in the plasma efficiency resulting from different amounts of sample ablation although particle size and distribution can not be neglected. Melting also becomes an important factor at this point. [23] Increasing the spark peak current also increases the amount of sample being ablated. As seen with increasing repetition rate, increasing the peak current does not cause a linear ICP-AES response. This can be attributed to the same reasons discussed above relative to the repetition rate.

Another spark parameter studied was the interelectrode gap. The spark stability and the ICP-AES signal intensity were found to be dependent on the gap size. Better precision and higher signal intensity were obtained for a larger gap. The smallest gap studied (0.75 mm) resulted in instability of the spark discharge and signal intensity of the ICP-AES.

The integration time of the ICP-AES played an important role in optimizing the signal intensity. It was evident that minor constituents needed a longer integration time and major constituents a shorter integration time. If an integration time was too long for a major constituent, saturation of the signal occurred. A short integration time for minor constituents resulted in "noisy" spectra.

Other parameters studied were the argon flow rate and RF power of the ICP-AES. An increase in signal intensity was obtained when increasing the RF power. An RF

power of 1200 to 1300 Watts was generally used for safety reasons. The argon flow rate played an important role in the resonance time of the ICP or the amount of time the sample spends in the plasma.

Once the parameters were optimized, the stability of the ablation process was determined through time profiles. A direct relationship between concentration and signal intensity was achieved for three orders of magnitude, suggesting that quantitation using this method should be straightforward and easy. Linearity at higher orders of magnitude is believed to be possible but could not be carried out because standards were not available. A critical point in solid sampling is to ensure "representative sampling." It is important that the ablated material be representative of the bulk material. This has been achieved as is evident in the accuracy and precision shown. A typical detection limit of approximately 10 ppm was achieved. Higher repetition rates may increase the detection limits but it was seen that higher repetition rates result in unstable discharges and signal intensities.

Operating conditions are dependent on the sample matrix. The efficiency of the spark sampling depends on the matrix chemical and physical properties, such as thermal conductivity, melting points, boiling points, and coating characteristics. It is therefore imperative to have a sampling device capable of sampling a variety of matrices. The "zero-bias" spark source is versatile as seen with results from steels, brasses, aluminum, and gold standards.

Experiments with fine gold standards showed that the "zero-bias" spark source coupled to an ICP, can detect trace amounts of constituents. Detection limits of 10-40 ppm were attained. It was also seen that higher repetition rates would lower the detection limits. The precision and accuracy are rather high for elements where the detection limits were not reached by the ICP-AES. It is likely detection limits would improve at a higher repetition rate and therefore, improve precision and accuracy. Unfortunately, this was not carried out due to instrumental limitations.

Involvement in the application of the "zero-bias" spark source coupled to an ICP-MS has also taken place and is discussed thoroughly in reference 59. These studies consisted of sampling non-conductive materials, studying the ablation rate and nature of the erosion crater on different sample matrice.

The first phase of the investigation of the "zero-bias" spark source as a solid sampling device for ICP-AES has been completed. The spark source can now undergo further engineering refinement and introduction as a commercially available instrument.

Future Work

The preliminary results obtained in this work for the "zero-bias" spark source as a solid sampling device for ICP look very promising for the analyses of a variety of sample matrices. However it is a first generation research-grade system and further development and understanding of the actual spark-solid interactions will undoubtedly lead to better performance. The present spark source has inherent instability within the timing circuit and a second generation spark source will concentrate on improving this. Efforts will also be made to improve the high voltage and high current diodes and switching devices so that they will be able to handle higher repetition rates and currents without overheating.

The sample holder needs further development. With the present sample holder, the sample electrode needs to be approximately one inch in diameter and no larger than five inches to create a seal. A sample holder that is adaptable to a variety of sample types and sizes would be more desirable. Also a sample holder which would permit more precise control over the positioning of the sample electrode would be beneficial.

Surprisingly, little is known about the process which occurs during the spark ablation event. In order to understand the sampling event, it would be necessary to study the effects of the initial spark on the electrode surface and succeeding spark events. Also, analysis of the nature of the particulates produced under different operating parameters and time should give further insight into the processes occurring. In the current work, initial efforts were made to study the effects of various repetition rates with an on-line

collection of ablated particles. Particle size and distribution may vary with operating conditions and sample matrix. Dissolution and analyses of the particles collected would be beneficial. Scanning electron micrograph data would also be advantageous.

A future application of the spark source ICP is the study of surface layers such as thin layer films. Quantitative analysis of surface layers may be possible. Maximum signal intensity values achieved during spark ablation integrated over a period of time could be estimated and used for this purpose.

Solid matrix matching standards are often difficult to find or are very expensive. It would be worthwhile to investigate the use of liquid standards for the analysis of solid samples by spark source ICP. With the current interface of the "zero-bias" spark source and ICP-AES, the nebulizer argon flow is connected to the spark source and ablated particles are transported through tygon tubing to the spray chamber. Adjustments must be made when analyzing solids in contrast to liquids.

REFERENCES

1. G.I. Babat, *J. Inst. Elec. Eng.*, 1947, **94**, 27.
2. S. Greenfield, I.L. Jones, and C.T. Berry, *Analyst*, 1964, **89**, 713.
3. R.H. Wendt and V.A. Fassel, *Anal. Chem.*, 1965, **37**, 920.
4. T.B. Reed, *J. Appl. Phys.*, 1961, **32**, 821.
5. M.R. Baker and B.L. Vallee, *J. Opt. Soc. Amer.*, 1955, **45**, 773.
6. H.F. Priest and A.V. Grosse, *J. Ind. Eng. Chem.*, 1947, **39**, 431.
7. I. Langmuir, *Science*, 1925, **62**, 463.
8. B. Karlovitz, *International Science and Technology*, 1962, **36**.
9. H.H. Willard, L.L. Merrit, Jr., J.A. Dean, and F.A. Settle, Jr., Instrumental Methods of Analysis, Seventh Edition; Wadsworth Publishing Company: Belmont, California, 1988.
10. M. Thompson and J.N.Walsh, Handbook of ICP Spectrometry, Second Edition; Blackie and Son Ltd.: Glasgow, 1989.
11. T.W. Barnard, M.I. Crockett, J.C. Ivaldi, and P.L. Lundberg, *Anal. Chem.*, 1993, **65**, 1225.
12. T.W. Barnard, M.I. Crockett, J.C. Ivaldi, P.L. Lundberg, D.A. Yates, P.A. Levine, and D.J. Sauer, *Anal. Chem.*, 1993, **65**, 1231.
13. J.P. Walters, *Appl. Spectrosc.*, 1969, **23**, 317.
14. A. Scheeline, *Prog. Anal. Atom. Spectrosc.*, 1984, **7**, 21.
15. A. Scheeline, *Mikrochim. Acta (Wien)*, 1990, **I**, 247.
16. E.E. Kunhardt and L.H. Luessen, eds. Electrical Breakdown and Discarges in Gases; Plenum Press: New York, 1983.
17. J.M. Meek and J.D. Craggs, eds. Electrical Brakdown of Gases; John Wiley and Sons: New York, 1978.
18. D.P.C. Thackeray, *J. Sci. Instr.*, 1958, **35**, 206.
19. S.W. Brewer, Jr. and J.P. Walters, *Anal. Chem.*, 1969, **41**, 1980.
20. A. Scheeline, J.A. Norris, J.C. Travis, J.R. DeVoe, and J.P. Walters, *Spectrochim. Acta, Part B*, 1981, **36**, 373.
21. L.J. Prell and S.R. Koirtyohann, *Appl. Spectrosc.*, 1988, **42**, 1221.

22. B. Raeymaekers, P. Van Espen, F. Adams, and J.A.C. Broekaert, *Appl. Spectrosc.*, 1988, **42**, 142.

23. R.L. Watters, Jr., J.R. Devoe, F.H. Shen, J.A. Small, and R.B. Marinenko, *Anal. Chem.*, 1989, **61**, 1826.

24. C.M. Cundall and J.D. Craggs, *Spectrochim. Acta, Part B*, 1954, **7**, 149.

25. D.M. Coleman presented at the Federation of Analytical Chemistry and Spectroscopy Societies, Chicago (1994).

26. J.A.C. Broekaert, *Spectrochim. Acta, Part B*, 1988, **43**, 119.

27. V. Karanassios, P. Drouin, and G.G. Reynolds, *Spectrochim. Acta, Part B*, 1995, **50**, 415.

28. R. Rattray and E.D. Salin, *J. Anal. At. Spectrom.*, 1995, **10**, 1053.

29. L. Moens, P. Verrept, S. Boonen, F. Vankaeck, and R. Dams, *Spectrochim. Acta, Part B*, 1995, **50**, 463.

30. A. Golloch, M. Haveresch-Kock, and F. Plantikow-VossGatter, *Spectrochim. Acta, Part B*, 1995, **50**, 501.

31. S. Q. Tao and T. Kumamaru, *Appl. Spectrosc.*, 1996, **50**, 785.

32. Y. Nakamura, K. Takahashi, O. Kujirai, and H. Okochi, *J. Anal. At. Spectrom.*, 1997, **12**, 349.

33. P.B. Farnsworth, and G.M. Hieftje, *Anal. Chem.*, 1983, **55**, 1414.

34. M. Thompson, J.E. Goulter, and F. Sieper, *Analysis*, 1981, **106**, 32.

35. J. Nolte, *Fresnius J. Anal. Chem.*, 1994, **349**, 131.

36. J.W. Carr, *Spectrochim. Acta, Part B*, 1982, **37**, 1.

37. D. Baldwin, *Anal. Chem.*, 1994, **66**, 1911.

38. X.R. Liu, *Spectrochim. Acta, Part B*, 1994, **50**, 537.

39. V. Kanicky and J.M. Mermet, *Appl. Spectrosc.*, 1997, **51**, 332.

40. X.L. Mao and R.E. Russo, *J. Anal. At. Spectrom.*, 1997, **12**, 177.

41. K.K.K. Lam and W.T. Chan, *J. Anal. At. Spectrom.*, 1997, **12**, 7.

42. P. Goodall and S.G. Johnson, *J. Anal. At. Spectrom.*, 1996, **11**, 469.

43. A. Scheeline and D.M. Coleman, *Anal. Chem.*, 1987, **59**, 1185A.

44. D.M. Coleman, M.A. Sainz, and H.T. Butler, *Anal. Chem.*, 1980, **52**, 746.

45. M.A. Sainz, and D.M. Coleman, *Appl. Spectrosc.*, 1989, **43**, 553.

46. H.G.C. Human, R.H. Scott, A.R. Oakes, and C.D. West, *Analyst*, 1976, **101**, 265.

47. J.Y. Marks, D.E Fornwalt, and R.E. Yungh, *Spectrochim. Acta, Part B*, 1983, **38**, 107.

48. A. Aziz, J.A.C. Broekaert, K. Laqua, and F. Leis, *Spectrochim. Acta, Part B*, 1984, **39**, 1091.

49. L.J. Prell, and S.R. Koirthyohann, *Appl. Spectrosc.*, 1988, **42**, 1221.

50. P.M. Beckwith, R.L. Mullins, and D.M. Coleman, *Anal. Chem.*, 1987, **59**, 22.

51. C. Webb, C.B. Cooper III, A.T. Zander, J.T. Arnold, E.S. Lile, and S.E. Anderson, *J. Anal. At. Spectrom.*, 1994, **9**, 263.

52. I. Steffan and G. Vujicic, *Spectrochim. Acta, Part B*, 1992, **47**, 61.

53. A. Ono, M. Saeki, and K. Chiba, *Appl. Spectrosc.*, 1987, **41**, 970.

54. M. Gagean and J.M. Mermet, *J. Anal. At. Spectrom.*, 1997, **12**, 189.

55. K.A. Ivanovic, D.M. Coleman, F.W. Kunz, and D. Schuetzle, *Appl. Spectrosc.*, 1992, **46**, 894.

56. A.G. Coedo, M.T. Dorado, and B. Fernandez, *J. Anal. At. Spectrom.*, 1995, **10**, 859.

57. O.V. Borisov, D.M. Coleman, and R.O. Carter III, *J. Anal. At. Spectrom.*, 1997, **12**, 231.

58. N. Jakubowski, I. Feldmann, and D. Stuewer, *Spectrochim. Acta, Part B*, 1995, **50**, 639.

59. O.V. Borisov, Ph.D. Dissertation, Wayne State University, 1997.

60. Perkin-Elmer Optima 3000 Hardware Guide, 1993.

61. J.S. Beaty and R.J. Belmore, *J. Test. Eval.*, 1984, **12**, 212.

62. David Ekimoff and John P. Walters, *Anal. Chem.*, 1981, **53**, 1644.

63. Automotive Aluminum Recycling; The Aluminum Association: Washington, D.C., 1997.

64. Automotive Aluminum Recycling Design Guidelines; The Aluminum Association, Washington, D.C., 1997.

65. A. Robinson, B. Shepherd, D.M. Coleman presented at the Federation of Analytical Chemistry and Spectroscopy Societies, Providence, (1997).

66. K.I. Oudsema, Ph.D. Dissertation, Wayne State University, 1993.

67. B.F. Scribner and C.H. Corliss, *Anal. Chem.*, 1951, **23**, 1548.

68. Application Bulletin "Determination of Gold Fineness using Spark Ablation and ICP-AES"; CETAC Technologies Inc., Omaha, 1997.

69. C.B. Boss and K.J. Fredeen, Concepts, Instrumentation, and Techniques in Inductively Coupled Plasma Optical Emission Spectrometry, Second Edition; Perkin Elmer: Norwalk, 1997.

ABSTRACT

A "ZERO-BIAS" SPARK SOURCE FOR DIRECT SOLID SAMPLE INTRODUCTION FOR INDUCTIVELY COUPLED PLASMA ATOMIC EMISSION SPECTROSCOPY

by

BILLIE A. SHEPHERD

May 1998

Advisor: Dr. David M. Coleman

Major: Chemistry (Analytical)

Degree: Doctor of Philosophy

A new "zero-bias" spark source was used as an ablation device for the analysis of solids with ICP-AES. Direct solid analysis has an inherent advantage for ICP applications as it allows a dry plasma to be maintained. This helps minimize the background species present as many arise from the water and acids present in solution. The use of a spark source as a sample introduction method for ICP employs separate sampling and excitation processes. In separating these two events, both may be optimized individually to give enhanced performance. Dependence of spark parameters such as peak current and repetition rate on analytical characteristics of the ablation process was found on the spark stability and performance of ICP-AES. Lower currents and repetition rates are generally optimal.

Analytical performance was evaluated by time profiles, a plot of emission intensity *vs.* time. Spark sampling and concurrent spectral emission are stable over time. Elements also tend to track each other was seen when ratioing minor elements signal intensity to the major constituent signal intensity of the sample. Linear correlations between measured signal intensities and concentrations of major and minor constituents in the samples were achieved. No internal standardization was required due to the similarity of the sample matrices for each series of samples. Experiments to measure spark reproducibility were performed. Acceptable accuracy and precision were achieved.

AUTOBIOGRAPHICAL STATEMENT

The author was born on May 18th 1971 in New Philadelphia, Ohio. After graduating with honors from Heidelberg College in 1993, she began graduate studies in Analytical Chemistry at Wayne State University under the direction of Dr. David M. Coleman. During undergraduate and graduate years she was involved in different projects in the field of inorganic, physical, and analytical chemistry. Her research at Wayne State University involved fundamental and applied studies in the field of spark based solid sampling with subsequent detection by ICP-AES. Most of this research involved collaboration with the Perkin-Elmer Corporation.

During her graduate career she was an author of three oral and two poster presentations.